Utah State University

DigitalCommons@USU

2014

Modeling the Defect Density of States of Disordered SiO2 Through Cathodoluminescence

Amberly Evans Jensen
Utah State University

Follow this and additional works at: https://digitalcommons.usu.edu/mp_etd

Part of the Condensed Matter Physics Commons

Recommended Citation

Utah State University
MERRILL-CAZIER LIBRARY

MODELING THE DEFECT DENSITY OF STATES OF DISORDERED SiO$_2$

THROUGH CATHODOLUMINESCENCE

by

Amberly Evans Jensen

A thesis submitted in partial fulfillment
of the requirements for the degree

of

MASTER OF SCIENCE

in

Physics

Approved:

_____   _____
Dr. JR Dennison   Dr. D. Mark Riffe
Major Professor   Committee Member

_____   _____
Dr. Eric Held   Dr. James S. Dyer
Committee Member   Committee Member

_____
Dr. Mark R. McLellan
Vice President for Research and
Dean of the School of Graduate Studies

UTAH STATE UNIVERSITY
Logan, Utah

2014

ABSTRACT

Modeling the Defect Density of States of Disordered SiO$_2$ Through Cathodoluminescence

by

Amberly Evans Jensen, Master of Science

Utah State University, 2014

Major Professor: Dr. JR Dennison
Department: Physics

This study measures the electron-induced luminescence (cathodoluminescence) for various samples of fused silica. With a band gap of ~8.9 eV, visible and near-IR (NIR) luminescence occurs only if there are states (localized defect or trap states) within the forbidden band gap for electrons to occupy. A model is presented based on the electronic band structure and defect density of states—used to explain electron transport in highly disordered insulating materials—which has been extended to describe the relative cathodoluminescent intensity and spectral bands as a function of incident beam energy and current density, sample temperatures, and emitted photon wavelength.

Tests were conducted on two types of disordered SiO$_2$ samples, the first type containing two variations: (i) thin (~60 nm) coatings on reflective metal substrates, and (ii) ~80 μm thick bulk samples. Luminescence was measured using a visible range SLR CCD still camera, a VIS/NIR image-intensified video camera, a NIR video camera, and a UV/VIS spectrometer. Sample temperature was varied from ~295 K to 40 K. The results of these tests were fit with the proposed model using saturation dose rate and mean shallow trap energy as fitting parameters and are summarized below.

First, each incident energy has a corresponding penetration depth, or range, which determines the fraction of energy absorbed in the material. In the thinner samples, the range exceeds the thickness of the sample; therefore, the intensity decreases with increasing energy. However, for the thicker samples, the range is less than the sample thickness and the intensity increases linearly with incident energy.

Next, at low current densities, luminescent intensity is linearly proportional to incident current density through the dose rate. At very high current densities, saturation is observed.

Finally, the overall luminescent intensity increased exponentially as T decreased, until reaching an optimum temperature, where it falls off to zero (as the model predicts). The spectra show four distinct bands of emitted photon wavelengths, corresponding to four distinct energy distributions of defect states within the band gap, each behaving differently with temperature. The response of each band to temperature is indicative of the extent to which it is filled.

(109 pages)

PUBLIC ABSTRACT

Modeling the Defect Density of States of Disordered SiO_2 Through Cathodoluminescence

Amberly Evans Jensen, Master of Science

Utah State University, 2014

Spacecraft charging is the accumulation of an electrical charge on orbiting spacecraft induced by the space plasma environment and has harmful effects on the electrical functionality of a spacecraft. This is studied extensively, particularly in the Materials Physics Group (MPG) at Utah State University (USU). During charging studies performed by the MPG, another potentially problematic effect of the space plasma environment on spacecraft was observed: light emanating from the sample undergoing electron beam bombardment. Space-based observatories are one type of spacecraft on which this luminescence may occur. If the luminescence from the material caused by the space plasma is within the field of view of the collection optics on the observatory or emanating from the collection optics themselves, the observatory images will be tainted by this light contamination. This problem provides the main motivation behind these experiments. It can also have applications in microelectronics, geological dating, and other fields.

The process of electron-induced luminescence, or cathodoluminescence, provides information on and insight into the electronic band structure of the material undergoing radiation. The energetic incident electrons excite electrons within the material from low-energy states to high-energy states. From there, electrons can undergo light emitting relaxation into trapped states residing in the material's band gap. Trapped states exist in the band gap because there are defect sites (doping sites or other sites, which deviate from the crystalline structure) within the structure of the material. The cathodoluminescence intensity and wavelength range behaviors in disordered SiO_2 are the focus of this thesis. The intensity has been shown to change as incident electron current density and energy change and as temperature varies. Further, wavelength spectral data show there are multiple defect bands available for relaxation.

The Utah State Materials Physics Group, with the funding of the NASA James Webb Space Telescope project and a NASA Space Technology Research Fellowship, is currently studying this phenomenon for disordered SiO_2 (as is presented here) and is extending their work to other materials.

ACKNOWLEDGMENTS

First, I would like to acknowledge and thank JR Dennison who has been an amazing mentor for my entire stay at Utah State. Thanks for taking a risk and giving me a chance as a freshman. Thanks for keeping me on and offering to allow me to get my master's degree with you. You have shown great patience with me throughout these years and I am truly grateful for that. Thanks for taking the time to help me grasp an understanding of our work over and over again.

Thank you to my committee members for being willing to be on my committee, for reading my thesis and offering great suggestions, and all the time you have put in to help me complete this thesis.

Thank you, Karalee and Sharon, for all the hours you put in on my behalf. Thanks for putting up with my procrastination regarding paperwork and for helping me get things in on time. You two are truly the best.

Thanks to all the USU Materials Physics Group members, past and present, who have put up with my singing and other weird behaviors while I've been a part of this group. You are each amazing people and physicists (or engineers). Specifically, I owe a big thank you to Greg Wilson and Justin Dekany. Without your help, I would not be completing my degree.

I would also like to acknowledge the NASA Space Technology Research Fellowship, which I received. This fellowship has not only funded my research, but has also provided me the opportunity to travel and work in national laboratories. Without this fellowship, these opportunities would not have been available to me. I am truly grateful for being chosen as a recipient.

I would like to thank my mom and dad for all their encouragement. You have always been supportive and behind me in my decisions with my education. You have encouraged me to try for things I didn't have the courage to do on my own. I would not be where I am without you. Thank you for being the best! I would also like to thank Joe, Liz, Amielyn, Justin, and Ashlynn who are the absolute best siblings anyone could ever ask for. You can always keep your nerd sister laughing and provide a fun diversion when I need one.

I appreciate my in-laws who have been encouraging and supportive of my decision to get this degree. My grandparents have also always encouraged excellence in my education and have been behind me all the way.

Finally, I would like to thank my husband, Matt. You are absolutely the best husband I could ever have asked for. Thank you for your support as I have worked to achieve this goal. Thank you for listening when I come home and start talking about how my tests are going and have to tell you. Thanks for your patience when I come home and vent all my frustrations to you. I love you and look forward to our many adventures together.

Amberly E. Jensen

CONTENTS

LIST OF TABLES

LIST OF FIGURES

LIST OF SYMBOLS

A_{fcs} = area of the Faraday cup as if it were at the sample position

A_{Sample} = area of the sample

$\dot{D}$ = dose rate

$\dot{D}_{sat}$ = saturation dose rate

E_b = incident beam energy

E_c = energy of the conduction band

E_{gap} = energy of the band gap

E_v = energy of the valence band

I_{fc} = total current in Faraday cup when positioned at peak position

I_{sample} = total current hitting the sample area when beam is centered on sample

I_γ = cathodoluminescence intensity

J_0 = Gaussian peak amplitude

J_b = incident beam current density

J_{fc} = mean Faraday cup beam current density at peak position

J_G = 2D Gaussian beam profile

J_{sample} = mean sample beam current density at peak position

k_B = Boltzmann's constant

L = material thickness

L_1 = distance for electron gun to faraday cup

L_2 = distance for electron gun to sample

q_e = electron charge

$R(E_b)$ = energy-dependent range

r_{fcs} = radius of the faraday cup as if it were at the sample position

r_m = Gaussian peak position

$\mathbb{R}_m(\lambda)$ = wavelength-dependent reflectivity of metallic layer

r_s = radius of the sample

T	= temperature
ε_{DT}	= energy depth of the deep traps below the conduction band
ε_{ST}	= energy depth of the shallow traps below the conduction band
$\eta(E_b)$	= energy-dependent backscattered electron yield
λ	= wavelength
ρ_m	= material mass density
σ	= Gaussian peak width
$A_f(\lambda)$	= wavelength-dependent optical absorption of the coating materials

LIST OF ABBREVIATIONS

CB	Conduction Band
CCD	Charge-Coupled Device
CF	Correction Factor (Faraday Cup to Sample)
CL	Cathodoluminescence
CSDA	Continuous Slow Down Approximation
DOS	Density of States
DT	Deep Trap
FC	Faraday Cup
HDIM	Highly Disordered Insulating Materials
MPG	Materials Physics Group
NBOHC	Nonbridging Oxygen Hole Center
NIST	National Institute of Standards and Technology
ODC	Oxygen Deficiency Center
RIC	Radiation Induced Conductivity
SLR	Single-Lens Reflex
ST	Shallow Trap
UHV	Ultrahigh Vacuum
USU	Utah State University
UV	Ultraviolet
VB	Valance Band
VIS	Visible

CHAPTER 1

INTRODUCTION

This thesis presents a study on the electron-induced luminescence, or cathodoluminescence (CL), of thin film fused silica (disordered SiO_2). The original motivation for this field of study was serendipitous. In studies conducted in the Materials Physics Group (MPG) at Utah State University (USU), originally focused on the charging properties of the many materials used in the construction of spacecraft, CL was observed when one person decided to simply peek inside the test chamber. Since that accidental discovery, CL has become another area of study for the MPG in conjunction with that of spacecraft charging. The specific study of highly disordered silicon dioxide (SiO_2) was originally motivated by its abundant use as an optical coating on mirrors located on space-based observatories. Should this coating produce light within the wavelength range of the optical detectors and be within the field of view of the detectors, the observatory itself would pollute its own images. After looking at the preliminary data, it was quickly realized much could be learned about the electronic band structure of fused silica by studying the behavior of its CL. This is the purpose and objective of this particular thesis study.

The study of the CL of disordered SiO_2, and other materials important in today's technologically advanced world, is not new or unique to the work done by USU's MPG. In recent decades, there have been multiple studies regarding this phenomenon. For example, Fitting has studied CL in fused silica and similar materials, the origin of the peaks in these spectra produced (Fitting *et al.*, 2000) and, to some extent, the temperature dependent behavior of the CL (Fitting *et al.*, 2001).   In addition to these studies, Fitting has also developed an understanding and technique for making silicon dioxide luminesce through ion implantation (Fitting, 2009). CL was used by Salh to determine the stoichiometry of different fused silica samples. As the ratio of oxygen to silicon varied, so did the presence of certain peaks in the CL spectra and intensities of those peaks (Salh *et al.*, 2006). Trukhin looked at the difference between thin film silica CL and bulk silica CL. In this study, they distinguished between self-trapped exciton and defect luminescence (Trukhin *et al.*, 1998). These and other works will be discussed in further detail later in this thesis and compared with our results.

The present studies were done using a low-flux, intermediate-energy electron beam to determine the total CL intensity dependence on incident electron beam current density and energy and material temperature. The presence of distinct wavelength bands within the total luminescence was also studied. The work presented here compliments previous work by continuing to study the electronic bands responsible for CL and extending the study of the CL intensity dependence on temperature. Also presented in this work is a study on total CL intensity dependence on current density and energy. The total CL intensity has been described by a single mathematical model, which includes these three parameters (material temperature, incident electron current density, and incident electron energy), as well as a fourth parameter (photon wavelength absorption and reflection), not studied here, but included for completeness. This has not been done in previous studies. The effect of incident beam current density and energy has been mentioned briefly in past studies (usually only as a side note or afterthought), but they have never considered the overall intensity; rather, they only looked at individual bands. Though the temperature dependence has been a major focus of previous work, it was, again, considered only for individual bands. It was also only done for two temperature extremes, room and liquid nitrogen temperatures, whereas in the present studies, measurements were taken continually as temperature changed from room temperature to 55 K. Though not studied presently, other factors that can have an effect on CL include surface potential, irradiation time, and sample history.

As was discussed above, CL can have detrimental affects when it occurs on space-based observatories. CL in space is caused by the space plasma environment, creating a harsh setting in which spacecraft reside. Fused silica is commonly used as the top coating on mirrors, making it possible for the telescope mirrors themselves to luminesce, optically contaminating the images collected by the observatory. On the other hand, the presence of CL in fused silica has proven useful in other applications. These include optical sensors for vacuum applications such as electron spectroscopy and microscopy or luminescence spectroscopy. It can also be used in the characterization of the SiO_2/Si/metal interfaces found in today's microelectronics. Geologists have also implemented a related phenomenon in the Optically Stimulated Luminescence Dating method. Though slightly different from CL, the fundamental physics involved in this technique is the same.

The body of this text is organized into four main sections. Chapter 2 will address the theory of the band model of fused silica. It begins with a review of the simple band theory of ordered materials to set the basis. Then the details of the fused silica material are presented. From this point, a band model of highly disordered insulating materials (HDIM) is given. This begins with a single, or mean, band model of CL intensity. This includes a mathematical model, which describes the overall CL intensity of fused silica. This model predicts dependence of the CL intensity on the incident beam current density and energy, as well as the material temperature and the photon absorptivity of the material and reflectivity of the substrate. It then moves on to a two-band model of the electronic structure of defects in fused silica. This is then extended to the more complicated four-band model, which is more representative of the bands that are actually present in fused silica. This qualitative schematic representation of the bands is developed using the temperature-dependent spectra obtained during experimentation. Finally, the chapter concludes by addressing the shape of the bands and the defects associated with the CL phenomenon.

Chapter 3 describes the instrumentation used and experimental methods implemented. Tests were conducted in the MPG Electron Emission Test chamber, at pressures on the order of 10^{-8} Torr. The temperature of the sample was adjusted using either a liquid nitrogen reservoir or a closed-cycle helium cryostat. Incident radiation was provided using one of two available electron guns attached to the chamber. Finally, CL was observed and recorded using an SLR CCD still camera, a CCD video camera and a UV/Vis spectrometer. The test matrix included measurements that would explore the temperature, incident electron energy, and flux dependence of the intensity of CL. Temperature dependence was tested by holding the incident beam flux and energy constant while lowering the sample temperature. Next, while holding the temperature and incident energy constant, incident electron flux was adjusted to show the flux dependence. By following this procedure at multiple energies, the energy dependence of CL intensity was also measured.

The results of the experiments are presented in Chapter 4. These are divided into two subsections: results within in the model and additional results for further consideration. The first section addresses the dependence of the model on incident beam current density, incident beam energy and material temperature. It also looks at the spectral bands and their individual behavior as a function of temperature. Here, the

experimental data are fit using the model from Chapter 2. A comparison of these results with the work found in the literature is provided for each parameter. The next section focuses on results that do not apply to the model, but are significant and therefore worth mentioning. The first is time dependence. Though not explicitly studied in this work, the time-dependent behavior observed in these tests are compared with time-dependent behavior described in the literature. The last is a certain edge effect the CL exhibited on one occasion, which could merit further study.

Finally, Chapter 5 contains the conclusions of this study. There is a summary of the theory and results, as well as the literature comparison. It describes, once more, the CL intensity model presented here and how the data are fit by this model. Following the summary is a discussion of the applications of disordered silicon dioxide CL, which were mentioned only briefly in this chapter. Finally, a framework for future studies on the CL of fused silica and other materials to be made by the USU MPG is presented.

CHAPTER 2

THEORY

This chapter discusses the development of the models and theory used to explain the experimental results, which will be presented later in this text.

2.1. Electron Band Model of Ordered Materials

The theory used to describe the luminescence phenomenon observed here is founded in the band theory of HDIM. This is reached, however, by beginning with the electron band model of ordered materials. In the development of the band theory of ordered periodic crystalline materials, the energy levels of individual atoms coalesce forming a continuum of energy levels as the atoms are brought closer together to create an ordered solid structure. The number of levels created in a given band is equal to the number of energy levels originally available, typically one per valence electron in the solid. Thus, as the number of atoms increases, so do the number of new energy levels, eventually creating a continuum with closely spaced energy levels (see FIG. 2.1). In FIG. 2.1(a), two atoms of the same energy are brought closer together until they form a bond and the two energy levels of the individual atoms separate, but still average the same energy level as the individual atoms. When five atoms [FIG. 2.1(b)] are brought together, the same separation occurs, but the separation distance between each level is much less than in the two atom model. Finally, in the many atom case [FIG. 2.1(c)], a continuous band is created where all energy levels within that band are available for occupation. These extended energy levels span the full spatial extent of the crystal. These energy bands are filled starting at the band of lowest energy up to the Fermi
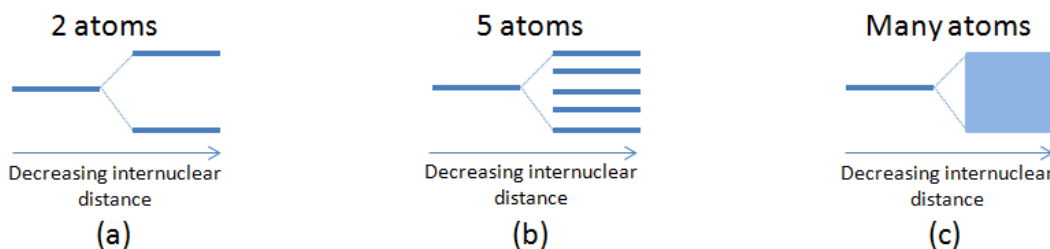
FIG. 2.1. Schematic of energy bands. Representation of the creation of the continua of energy levels, or energy bands, as the energy levels of individual atoms coalesce for (a) two atoms, (b) five atoms, and (c) many atoms.

energy (at low temperature).

The extent to which these energy bands are filled is the means of classifying solids as conductors, semiconductors, and insulators (FIG. 2.2). Conductors have a partially filled highest energy band, the conduction band (CB). Electrons that occupy this band have high mobility, allowing electrons to move freely in the extended states, leading to high electrical conductivity. By contrast, insulators have a fully filled valence band and a large band gap between the valance band (VB) and the empty CB. Even for large thermal energies, VB electrons have an extremely low probability of being thermally excited into the CB. Thus, electrons in insulators have very little mobility, making these materials electrically insulating. Semiconductors are insulators with a small band gap so, with sufficient thermal energy, electrons in the valence band have a small, but significant, probability of excitation into the higher bands, therefore leading to moderate conductivity.

The Fermi energy of a material is the energy of the highest filled state at absolute zero; the Fermi level, ε_F, is the (weakly) temperature-dependent chemical potential defined as the energy with 50% probability of filling a state. For intrinsic insulators and semiconductors with no defect states, the Fermi energy is at the middle of the band gap (FIG. 2.2). If, as in our experiments, electrons are added to a disordered material by electron bombardment, these new electrons will start to fill energy levels above the
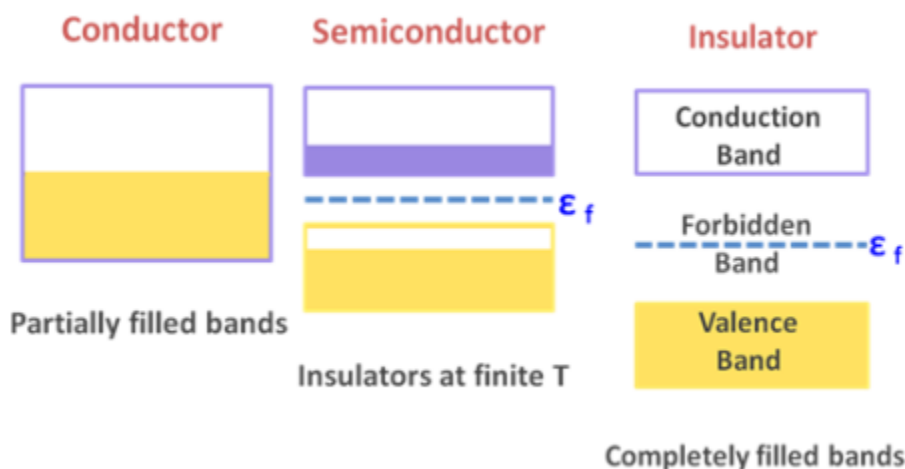
FIG. 2.2. Classification of conductors, semiconductors, and insulators. In a periodic solid, the classification of solids as conductors, insulators and semiconductors is determined by the extent of the filling of bands. Note the position of the Fermi level, ε_F.

Fermi energy, thus creating what is termed an effective Fermi level, ε_F^{eff}; this can be thought of as a charge-(and temperature-) dependent chemical potential.

2.2. Fused Silica

Fused silica (SiO_2) is an amorphous or noncrystalline form of silica, in contrast to the crystalline form of SiO_2, quartz (FIG. 2.3). It has a density of 2.2 g/cm^3. It is an insulating material that has a band gap of about 8.9 eV. Hence, thermal excitation from the VB to CB is highly improbable; the only likely source of such excitation is through collisions of incident high-energy electrons with valence electrons, through a process referred to as electron-hole creation. Since visible light is in the 1.65 to 3.1 eV range, even if electrons in the VB of SiO_2 were electronically excited to the CB, no visible light, only high-energy UV radiation with > 8.9 eV, could be emitted upon relaxation or recom bination of the excited electron with an empty state in the VB (termed a hole). Thus, because visible light is emitted, there must be other states within the band gap where the electrons can reside; there must be localized defects or trap states (FIG. 2.4).

FIG. 2.4 shows the transition from ordered to disordered materials. In FIG. 2.4(a), the band gap is empty; there are no localized states in an ordered material between the VB edge (E_V) and the CB edge (E_C) in which electrons can reside. As disorder is introduced, trap states begin to occupy the band gap [FIG. 2.4(b)]. The trap states of fused silica consist of shallow trap (ST) and deep trap (DT) states. The ST states are located within k_bT of E_C and are now separated from the CB by what is termed the mobility edge.
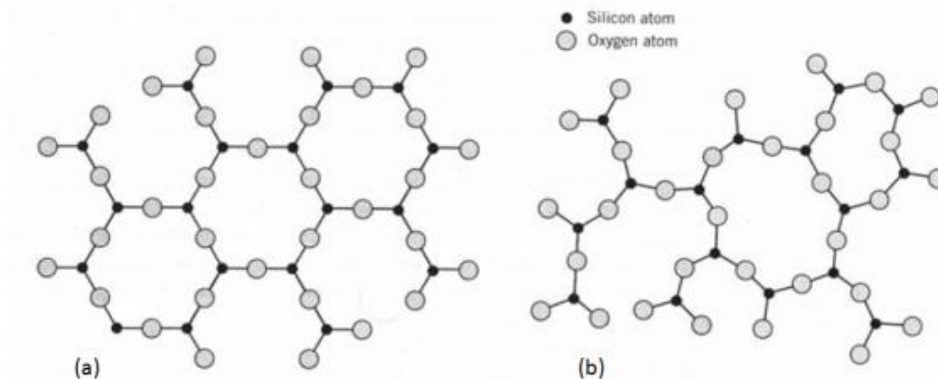
FIG. 2.3. Quartz and fused SiO_2 structures. (a) Crystalline SiO_2 structure. (b) Noncrystalline or fused SiO_2 structure. Note the change in the uniformity of the structure.
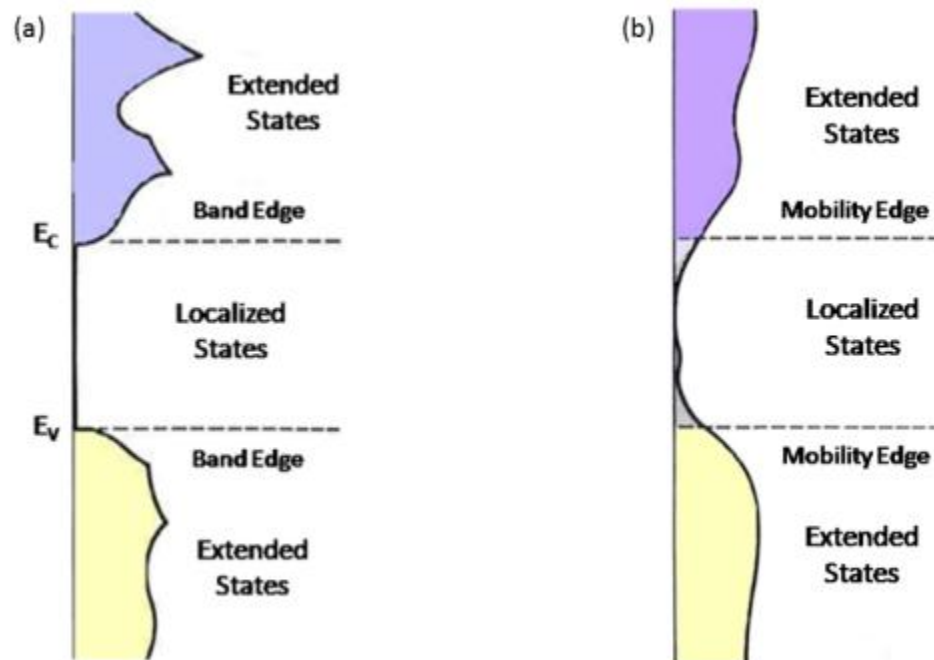
FIG. 2.4. Crystalline to disordered band structure. (a) In ordered solids, extended states in the VB and CB are separated by a band gap. (b) In disordered solids, variations in the periodic order cause extended states to become localized in space. These occur in the forbidden band gap, forming localized trapped states, separated from extended states by a mobility edge (Sim and Dennison, 2010b).

These states are created by minor, low-energy defects within the crystalline structure of SiO_2. These defects could be the small deviations within the crystalline structure as seen in FIG. 2.3(b). The DT states are located $>k_bT$ of E_C and are created by more drastic, high-energy defects with the crystalline SiO_2 structure. Defects of higher energy, for example, those shown in Section 2.3.4, are those where atoms are missing completely from the structure.

2.3. Band Model of Highly Disordered Insulating Materials

A model with multiple DT bands is necessary to qualitatively explain the observed CL emission spectra of disordered SiO_2. CL occurs when there are localized DT states with long lifetimes available for electron relaxation. The localized states within a material are due to defects in the crystalline structure or chemical defects from possible substitutional dopants. These defects within the material can behave as chromophores, the sites in a molecular structure from which luminescence originates. These chromophores

can be inherently present within the structure, can appear when there are structural defects in the molecular structure, or can be induced by electron beam bombardment.

The structural defects add localized energy states within the forbidden band (FIG. 2.4). The observed luminescence occurs when an incident high-energy, charged particle undergoes a series of inelastic collisions exciting valence band electrons into the conduction band. The excited electron rapidly decays to localized ST states, with a mean binding energy ε_{ST} below the mobility edge. A final electron transition, from the short-lived ST states to longer-lived DT states is the origin of the emitted photon if that process is a radiative process (Sim and Dennison, 2010a). Therefore, if these radiative processes are in the appropriate energy range, visible or IR photons will be emitted. The presence of four identifiable UV/VIS peaks in the observed spectra of disordered SiO_2 (see Chapter 4) suggests there are at least four bands of optically active localized defect DT bands well within the band gap. These DT bands are located at energies of $\gtrsim hc/\lambda$ below the mobility edge, where λ is the wavelength of the emitted CL photons. The temperature-dependent peak intensities are determined by the extent and occupancy of these DT bands, which will be proportional to the number of available, optically active DT states, the number of electrons that can transition into DT states (which is typically the number of electrons in ST states), and a transition probability. The occupancy of a given state is determined to first order by the ε_F^{eff} for a given density of trapped charge states. A more detailed model will take into account the transition probabilities from one DT state to another and nonradiative recombination of electrons with largely immobile VB holes or disordered acceptor states above the VB.

2.3.1.   Single (Mean) Band Model of Cathodoluminescent Intensity

The model for the observed CL phenomenon is based on band theory of HDIM as discussed above. We begin with a model for a single or mean band available for relaxation, which predicts the overall CL intensity behavior.

The luminescent intensity, I_γ, is proportional to the number of available states and the transition rates of each phase depicted in the modified Joblonski diagram (Joblonski, 1935; Lakowicz, 1983) of FIG. 2.5. This diagram illustrates the different paths an excited electron can take after being excited from the
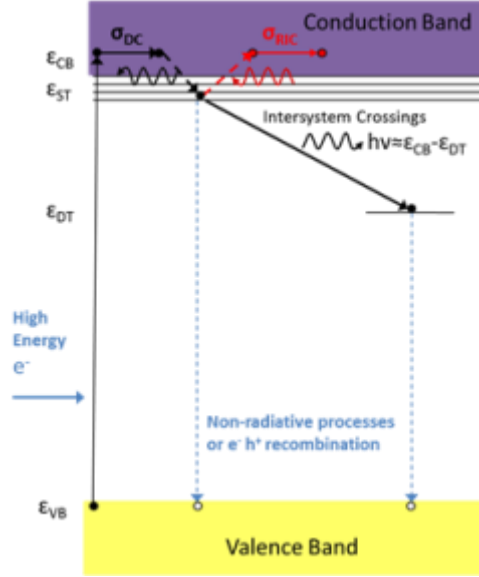
FIG. 2.5. Modified Joblonski diagram for CL. Shown are transitions between the extended state VB and CB bands, ST states at ε_{ST} within $\sim k_B T$ below the CB edge, and DT distributions centered at ε_{DT}. Energy depths are exaggerated for clarity.

VB to CB by the high-energy electron flux (dose). After relaxing quickly from the CB into a ST state, the electron can take one of three paths. One, it can undergo a nonradiative relaxation back to the VB, by way of the Auger effect, for example. It could also be reexcited into the CB, undergoing radiation induced conductivity (RIC). Finally, as discussed above and the interest of this thesis, the excited electron can undergo radiative relaxation to a DT state well below the CB. In this process, a photon is emitted equal in energy to the energy difference between the ST and DT states.

Here we propose a single band or mean DOS model for the overall intensity of the radiative process, which predicts the luminescence intensity, I_γ, scales with incident current density, J_b, incident beam energy, E_b, temperature, T, and photon wavelength, λ, as

$$I_\gamma(J_b, E_b, T, \lambda) \propto \frac{\dot{D}(J_b,E_b)}{\dot{D}(J_b,E_b)+\dot{D}_{sat}}\left\{\left[1 - e^{-(\varepsilon_{ST}/k_B T)}\right]\right\}\left\{\left[1 - \mathbb{A}_f(\lambda)\right]\left[1 + \mathbb{R}_m(\lambda)\right]\right\} \quad (2.1)$$

$\dot{D}$ is the dose rate, or absorbed power per unit mass. The intensity, or emitted power should be proportional to the deposited high-energy electron radiation power. The dose rate is the deposited power per unit mass.

The deposited power density is simply the incident power density, E_bJ_b, corrected for the efficiency with which power is absorbed (the bracket term in Eq 2.2). The dose rate is given by

$$\dot{D}(J_b, E_b) = \frac{E_b\, J_b[1-\eta(E_b)]}{q_e \rho_m} \times \begin{cases} [1/L] & ; \ R(E_b) < L \\ [1/R(E_b)] & ; \ R(E_b) > L \end{cases} \quad . \tag{2.2}$$

q_e is the electron charge, ρ_m is the mass density of the material, and L is the sample thickness. At high dose rates, saturation is observed, characterized by a material and sample-dependent saturation dose rate, $\dot{D}_{sat}$. The meaning of sample dependence is that the defect density of states can vary from one sample to another, even in samples of the same material. This causes variations in the saturation dose rate value between samples.

R(E_b) is the energy-dependent penetration depth or range, which is a material-dependent property. FIG. 2.6 (a) shows the range of SiO_2 as a function of incident electron energy calculated in the continuous slow down approximation (Wilson and Dennison, 2012), and the associated dose rate for 10 nA-cm^{-2} incident current density. The dose rate depicted in this figure assumes R(E_b) > L for penetrating radiation throughout the entire energy spectrum, which is the reason for the specific behavior seen here. FIG. 2.6 (b) shows the behavior of the dose rate for a 60 nm fused silica material with a 10 nA-cm^{-2} incident current. This shows the linear behavior of the dose rate when the range is less than the sample thickness; in other words, the beam is nonpenetrating and all the incident power is absorbed in the material. Following the linear portion, it shows the dose rate falls off when penetrating radiation occurs. This occurs when the range is greater than the sample thickness and the absorbed power is reduced by a factor of $[L/R(E_b)]$ (Dennison *et al.*, 2012).

The dependence of the CL intensity on the dose rate is twofold. The first arises in the incident beam current density. According to Eqs 2.1 and 2.2, if the dose rate is sufficiently smaller than the saturation dose rate of a given material, then as the current density increases, the CL intensity will increase linearly. However, as the dose rate approaches the saturation dose rate, the behavior of the intensity begins to bend over and approaches a saturation or maximum intensity level (see FIG. 2.7). This effect can be attributed to the filling of ST states to the point that even by exciting more VB electrons to the CB by
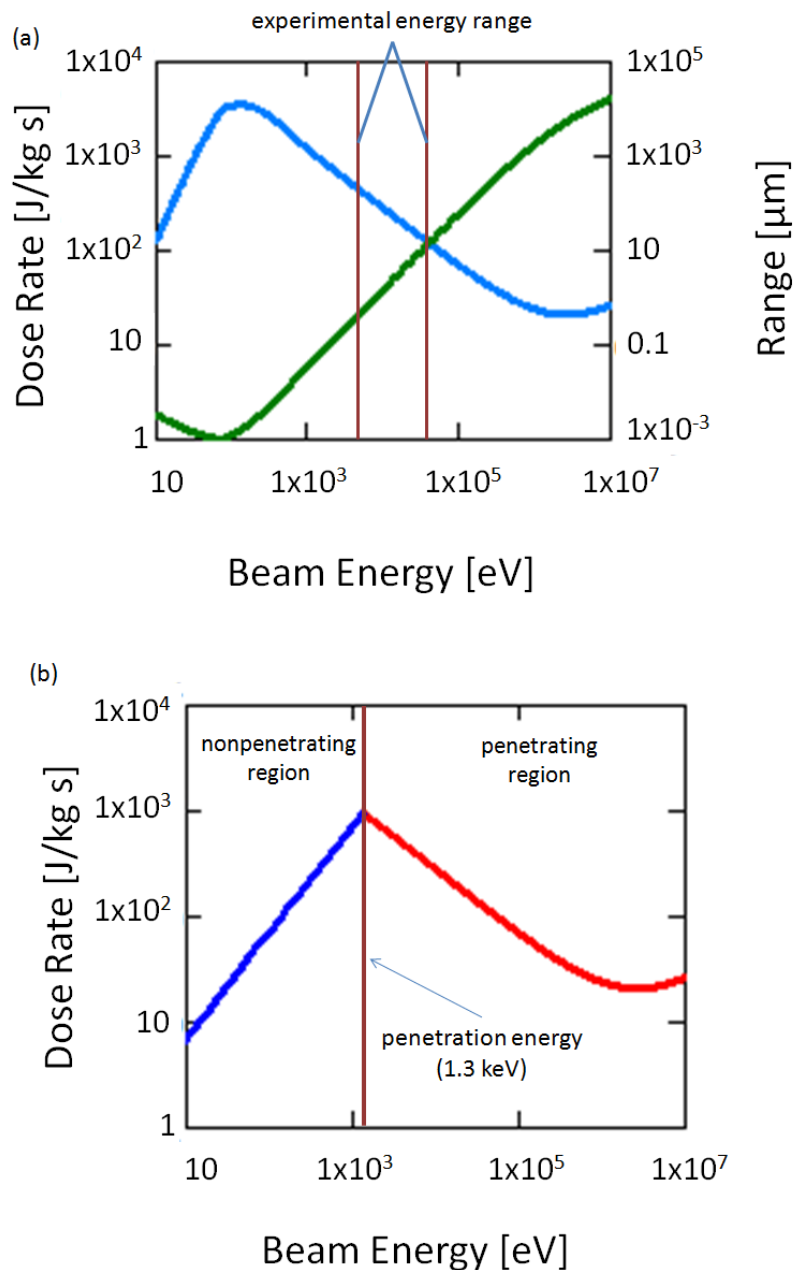
FIG. 2.6. Range and dose rate plotted against electron beam energy. (a) Range (green) and dose rate (blue) of disordered SiO_2 as a function of incident energy using the continuous slow-down approximation, based on calculations from (Wilson and Dennison, 2012). (b) The dose rate as a function of energy. The blue, increasing portion is the nonpenetrating beam, when the dose rate is range independent. The red, decreasing portion is when the beam is penetrating and the dose rate becomes range dependent. For the ~60 nm thick sample shown here, the crossover occurs at the penetration energy of ~1.3 keV.
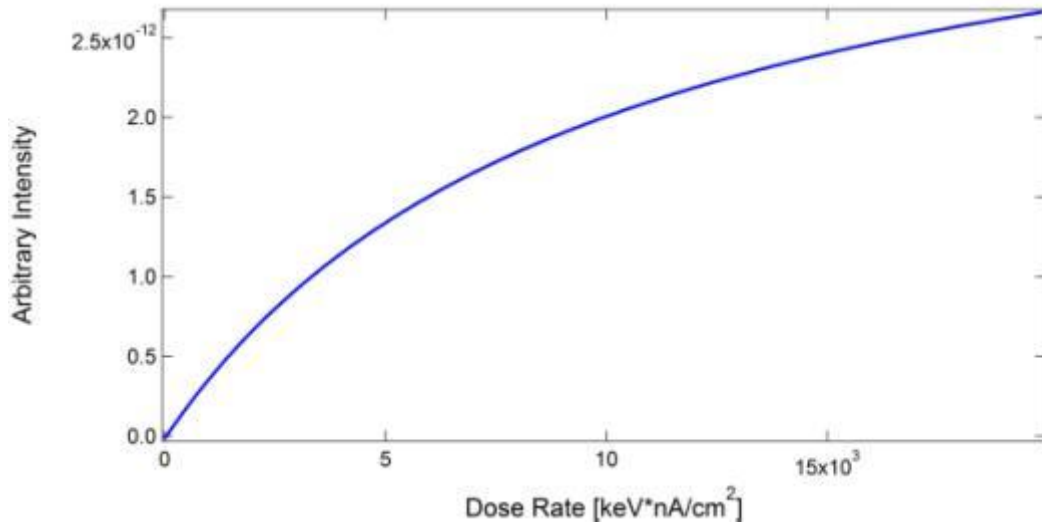
FIG. 2.7. CL intensity saturation effect. As the dose rate increases, the intensity of the CL deviates from the linear increase and approaches a horizontal asymptote.

increasing the incident beam current, there are no longer states available for all the excited electrons to relax into and then contribute to CL.

Alternately, the saturation behavior can be attributed, through the dose rate, to an increase in the sample surface potential as excess space charge increases as trap states are filled. Higher-energy incident electrons can excite a proportionally higher number of valence electrons into the CB; as more electrons are trapped in the material and surface potential rises, the landing energy of incident electrons, $(E_b - q_e V_s)$, decreases, thereby reducing the number of valence electrons excited by the incident electrons. At saturation, an equilibrium is reached in both the dose rate and surface charge.

For biased samples, or when excess charge is stored in the trap states, a surface voltage, V_s, results and E_b is replaced everywhere in Eqs. (2.1) and (2.2) by the landing energy, $(E_b - q_e V_s)$. Thus, glow intensity may diminish appreciably for kV surface potentials often observed on GEO satellites in eclipse. In the calculations presented here, this affect was assumed to be negligible.

Another way in which the dose rate depends on energy is through the range of the beam within the material. When the incident beam is nonpenetrating, as described above, the CL intensity increases linearly as the beam energy increases. This occurs because all the power in the beam is deposited in the material. Thus, for nonpenetrating radiation, below saturation limits in the current density and the energy, increasing

the energy increases the number of VB electrons that are excited to the CB, which then contribute to CL. There is a penetration energy, though, at which the range exceeds the thickness of the material and the beam becomes a penetrating beam. At this point, some of the incident beam power is lost, or not deposited in the material. It is at this penetration energy the linear increase of the intensity stops and it begins to fall off with increasing energy.

Inclusion of a weakly energy-dependent backscatter coefficient, $\eta(E_b)$, in Eq. (2.2) corrects the dose rate for incident electrons that quasi-elastically backscatter without depositing appreciable energy in the material (Dennison *et al.*, 2012). For the most part, this correction is small and weakly dependent on energy. For SiO_2, η is ~0.2 over the energies used for this thesis.

The effects of these two experimental parameters, current density and energy, on CL intensity are not independent of each other. For example, the current density at which saturation occurs depends on the beam energy and whether or not that energy is penetrating or nonpenetrating.

The thermal dependence of luminescence is characterized by the energy depth of the shallow traps below the CB, ε_{ST}. This energy depth, ε_{ST}, is defined as the ST energy level at which there are appreciable trapped electrons, which can be excited into the CB. In equilibrium, I_γ is proportional to the fraction of electrons that are retained in the shallow traps and not thermally excited into the conduction band ($\propto \left[1 - e^{-(\varepsilon_{ST}/k_B T)}\right]$ (see FIG. 2.8). At higher temperatures where $k_B T \gg \varepsilon_{ST}$, the thermal energy exceeds ε_{ST}, and $I_\gamma \propto \left(\varepsilon_{ST_Q}/k_B T\right)$. This predicts there is a critical temperature where the maximum CL will occur and approaches an asymptotic limit as the temperature goes to zero. Above this critical temperature, the intensity decreases, falling off as $I_\gamma \propto \left\{\left[1 - e^{-(\varepsilon_{ST}/k_B T)}\right]\right\}$. This fall off occurs because electrons within the ST states receive more thermal energy as temperature increases, thus reexciting more electrons into the CB. This reduces the number of electrons available for radiative relaxation into the DT states; there are fewer electrons contributing to CL.

In other words, $I_\gamma \propto \left\{\left[1 - e^{-(\varepsilon_{ST}/k_B T)}\right]\right\}$ where the 1 accounts for the number of electrons excited to the CB, which relax into the ST states. The exponential form accounts for the number of electrons that
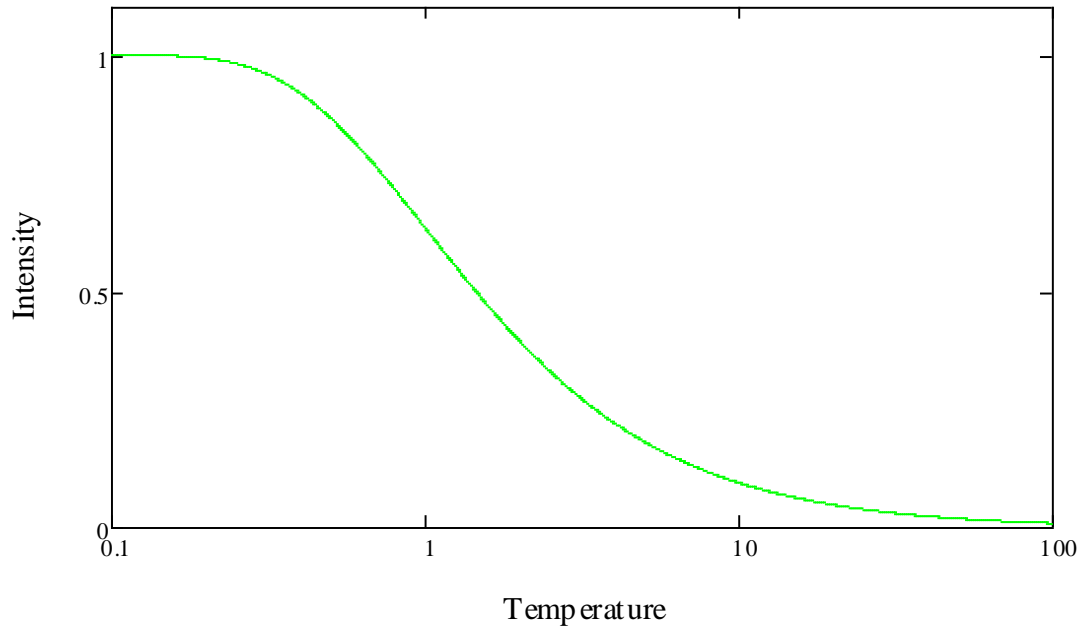
FIG. 2.8. Temperature-dependent behavior of CL. The plot shows the electrons in the ST states, not thermally excited to the CB, which therefore, can contribute to the overall CL intensity. Here, the x-axis is a relative temperature of the form $\frac{k_B T}{\varepsilon_{ST}}$.

are thermally excited form the ST states back to the CB and contribute to RIC (as described below) and not to CL. This assumes the number of electrons involved in nonradiative relaxation processes is negligible.

The temperature-dependent behavior of CL is complimentary of RIC, an electron mechanism mentioned above (FIG. 2.5). When RIC occurs, electrons in the ST states are excited into the CB where they contribute to the conductivity of the material. RIC has been found to increase with increasing temperature for fused silica, meaning as temperature increases, more ST electrons are thermally excited into the CB. Temperature-dependent RIC tests were done at USU in the temperature range of ~100 to ~280 K (Gillespie, 2013; Dennison *et al.*, 2014a; Gillespie *et al.*, 2014). This behavior is opposite that of CL intensity for this temperature range, as expected. As more electrons undergo the RIC phenomena at these higher temperatures, fewer are available to relax into DT states and contribute to the overall intensity of CL.

The final term in curly brackets in Eq. (2.1) accounts approximately for the wavelength, λ, of photons propagation through the coating. The optical absorption of the SiO_2 coating materials is $A_f(\lambda) \ll$

1 for propagation through the full film; thus it does not contribute significantly for these measurements. $\mathbb{R}_m(\lambda)$ accounts for the possibility of a reflective metallic layer underlying the dielectric coating. For highly reflective materials like Ag, $\mathbb{R}_m \approx 1$ at all λ considered. For materials like Au or Cu, the glow spectrum is enhanced at longer λ, due to greater absorptivity of Au at shorter λ. The effect of the reflectivity of the substrate for different samples has not been studied here but is included in Eq (2.1) for the sake of completeness.

2.3.2.   Two-Band Model of Cathodoluminescent Intensity

Next, we move on to a simple two-band model of the electronic band levels within the band gap of fused silica. Here, instead of focusing on the overall intensity, we look at how individual bands will behave, specifically the red (R) and ultraviolet (UV) bands. FIG. 2.9 illustrates this band model for DT distributions centered at ε_{red} and ε_{UV} below the CB edge. Radiation dose and dose rate control the number of electrons in the DT as measured by the ε_F^{eff}. Thermal energy controls the thermal excitation of the electrons and the relative filling of the DT bands. In this model used to illustrate the basic temperature behavior, an ε_F^{eff} is located between peaks at ~275 nm and ~645 nm, as shown in FIG. 2.9. The band
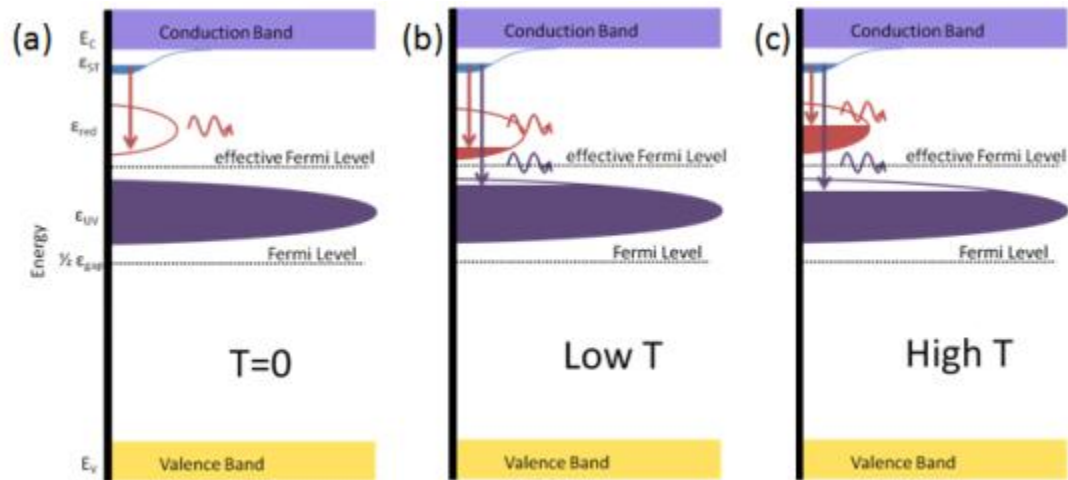
FIG. 2.9. Qualitative two-band model of occupied densities of state (DOS) as a function of temperature during CL. (a) At $T \approx 0$ K, the deeper band DOS is filled, so there is no UV photon emission if $\varepsilon_{UV} < \varepsilon_{eff}$. (b) At low T, electrons in UV DT are thermally excited to create a partially filled upper band (decreasing the available DOS for red photon emission) and a partially empty lower band (increasing the available DOS for UV photon emission). (c) At higher T, enhanced thermal excitations further decrease red photon emission and increase UV photon emission.

generating red photons has available, optically active states at an energy ε_{red}~1.93 eV below the CB edge. A similar band generating the ~275 nm photons is centered at ε_{uv} ~4.97 eV below the CB edge. At different temperatures, the varying amounts of thermal energy control the thermal excitation of the electrons and the relative filling of the bands. These thermal excitations will fill available energy levels in some energy bands, while vacating levels in the other, assuming the two bands are close enough together for the thermal excitation of an appreciable number of lower-energy band electrons into higher-energy bands. This is the origin of the different photons intensities being emitted at different temperatures.

At absolute zero [see FIG. 2.9 (a)], no electrons will occupy levels above the ε_F^{eff}. Thus, the UV band is full and the red band is empty. Therefore, excited electrons can only relax into states in the red band, emitting lower-energy red photons. At low temperatures with $0<k_BT<<(\varepsilon_{red}-\varepsilon_{uv})$ [see FIG. 2.9 (b)], a significant number of electrons in the UV band (represented in blue in FIG. 2.9) are thermally excited to the red band (either directly or through an intermediate excitation into the CB). This creates empty states in the UV band that can then accept electrons decaying from the ST states and generating higher-energy UV photons. Thus, significant numbers of electronically excited electrons can now relax from the ST states into either the red or UV bands. Since, to first order approximation, the number of electrons that can decay into either the red or UV bands from the ST states is the same; it does not affect the relative intensities. However, the relative intensities of the R and UV emission depend on the relative number of unoccupied states in the two bands and the transition probabilities into these two bands from the ST states. There is also a weaker dependence of the emission intensities on the transition from red band states directly into UV band states and for recombination of electrons in the R and UV band with largely immobile holes in the VB. At higher temperatures $0<<k_BT<(\varepsilon_{red}-\varepsilon_{uv})$ [see FIG. 2.9 (c)], even more electrons from the UV band are thermally excited into the red band. At high enough temperature, if the decay time of electrons from sites in the red band into the UV band is longer than the trapping of electrons excited into the CB by incident high-energy electrons, a population inversion can occur similar to that observed in a three-level laser system. To summarize the band temperature behavior, as temperature increases, the red band intensity decreases, but the UV band intensity increases.

2.3.3.   Four-Band Model of Cathodoluminescent Intensity

Using this two-band model is a good starting point, but it is obviously not the entire picture, considering the fact four bands appear, not only in some of the spectra collected during these experiments, but in experiments found in the literature, as well (McKnight and Palik, 1980; Fitting *et al.*, 2000, 2001). To fully understand the behavior, a model containing all four bands must be used.

In the model containing four DT bands, the behavior of the R and UV bands is the same as it was in the two-band model. The ε_F^{eff} is still located between these two bands and the mechanism for the production of CL is the same; that is, excitation from the VB to CB, subsequent relaxation into the ST states, followed by radiative relaxation into the DT states, producing CL.

The green (G) and blue (B) bands lie between the R and UV bands, just as the ε_F^{eff} does. This suggests the ε_F^{eff} is located within these two bands, which overlap in energy. The overlap in energy and the location of ε_F^{eff} within the bands proves to complicate the behavior of the intensity of these two bands, as will be seen in Chapter 4. Due to the complexity of the schematic, only the $T = 0$ K scenario is depicted in FIG. 2.10.

2.3.4.   Band Shape and Associated Defects

The lifetime of the extended states (CB) is typically very short while the ST states have intermediate lifetimes. The DT states, on the other hand, have typically very long lifetimes. It is these long lifetimes of the DT states that give the DT bands in the model, and their spectral band counterparts, as will be seen later, their Gaussian shape. Short lifetimes would, alternatively, produce Lorentzian-shaped bands. This shape is depicted in FIG. 2.11. While each peak will contain some component of a Lorentzian distribution, fitting the data with a Lorentzian or a Voight (convolution of a Gaussian and a Lorentzian) distribution would, many times, cause the fitting program to malfunction, as is discussed in Appendix A.

The amplitude and width of the peaks, not just the location, provide information on the DOS in the material and the occupancy of these states. The amplitude can indicate the number of available, unoccupied states there are for relaxation. The width indicates the distribution of the energy levels associated with a certain defect.
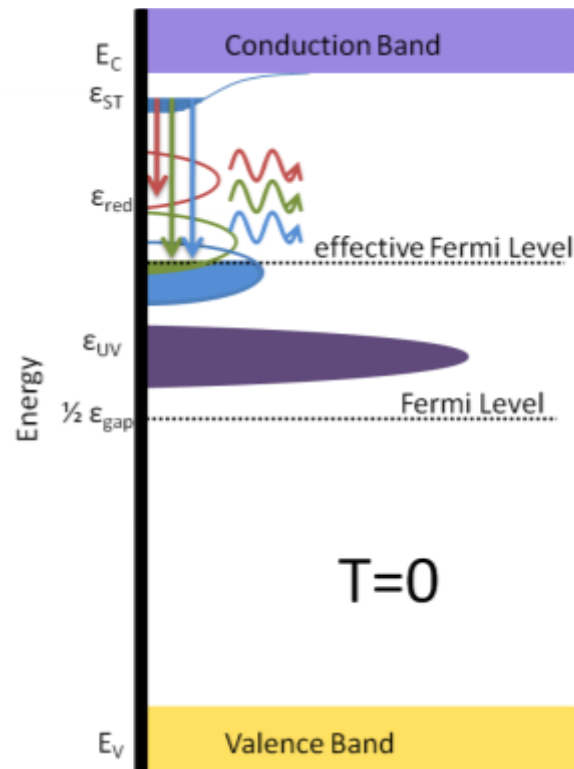
FIG. 2.10. Depiction of four-band model of CL intensity. At $T \approx 0$ K, the deeper band DOS are filled, so there is no UV photon emission if $\varepsilon_{UV} < E_F^{eff}$. There will be red, green, and blue photons emitted if E_F^{eff} is located such that it is within the blue and green bands and there are empty states in both for electrons to relax into.

Some of the DT states that exist in the electronic band structure of disordered SiO$_2$, which contribute to CL, have been identified and are also depicted in FIG. 2.11. The R band is attributed to a nonbridging oxygen hole center (NBOHC) (Goldberg *et al.*, 1997; Salh *et al.*, 2006). The B and UV bands are associated with an oxygen deficient center (ODC) or twofold coordinated silicon centers (McKnight and Palik, 1980; Goldberg *et al.*, 1997; Trukhin *et al.*, 1998). The UV band is attributed to a singlet-singlet (allowed) transition and the B band is attributed to a triplet-singlet (forbidden) transition (Goldberg *et al.*, 1997). Here, singlet and triplet refer to the value of the electronic spin quantum number, S. If S = 0, it is a singlet state, if S = 1, it is a triplet state. When $\Delta S = 0$, the transition is allowed.
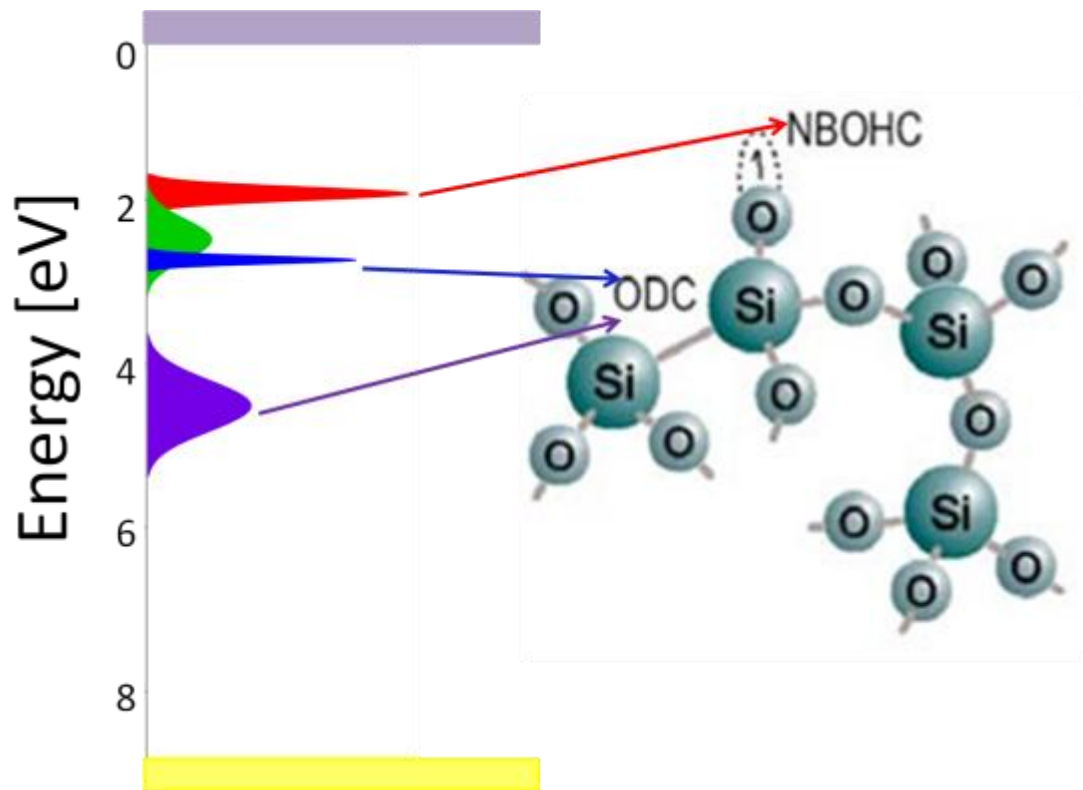
FIG. 2.11. DT states and associated defects. The existence of at least four peaks in the disordered SiO_2 luminescence spectra suggest at least four bands of localized defect or DT states. SiO_2 studies at room temperature have attributed a 645 nm peak to a nonbridging oxygen hole center (Salh *et al.*, 2006) and the 275 nm and 500 nm peaks to an oxygen deficient center (Trukhin *et al.*, 1998).

CHAPTER 3

INSTRUMENTATION AND EXPERIMENTATION

This chapter begins with a description of the various samples studied, their characteristics, and their preparation for testing. The tests performed on these samples are enumerated. The details of the instrumentation are presented, and the procedures for experimentation follow. The chapter ends with a description of the analysis procedures used.

3.1. Samples

3.1.1.   Sample Characterization

Three different samples were used in these tests (Table 3.1). One was a thin film fused silica coating on top of a Ag reflective surface [FIG. 3.1 (a)]. The layer structure of these mirrors is shown in FIG. 3.2. These mirrors are circular with a 25 mm diameter. As seen in FIG. 3.2, the thickness of the thin film coating is ~60 nm. Another was similar to the first, but on a Au reflective surface [FIG. 3.1 (b)]. These two samples were supplied under a NASA-funded project, and the fused silica layer was created using the sputter deposition process. The last sample was a bulk fused silica sample with no substrate permanently attached. This was a 25 mm square and ~80 nm thick fused silica Corning 7980 sample [FIG. 3.1 (c)], created using the hydrolysis process.

3.1.2.   Sample Preparation

The samples of optically smooth, thin film disordered SiO_2 (as described in 3.1.1) were optically cleaned and underwent a ~12 hr vacuum bakeout at ~390 K and <1•10-3 Pa to eliminate adsorbed water

Table 3.1. Material information. A layout of experiment label, sample name, sample thickness, sample substrate, electron source, sample holder and the data collected from that test.

Experiment	Sample Name	Thickness	Substrate
A	Pick Off Mirror	60 nm	Au
B	Primary Mirror	60 nm	Ag
C	Bulk Sample	80 μm	Cu
Experiment	Electron Source	Sample Holder	Luminescent Data
A	HEED	Carousel	J_b, E_b -dep.
B	STAIB	Carousel	T-dep
C	HEED	Sample Round	J_b, E_b, T -dep.
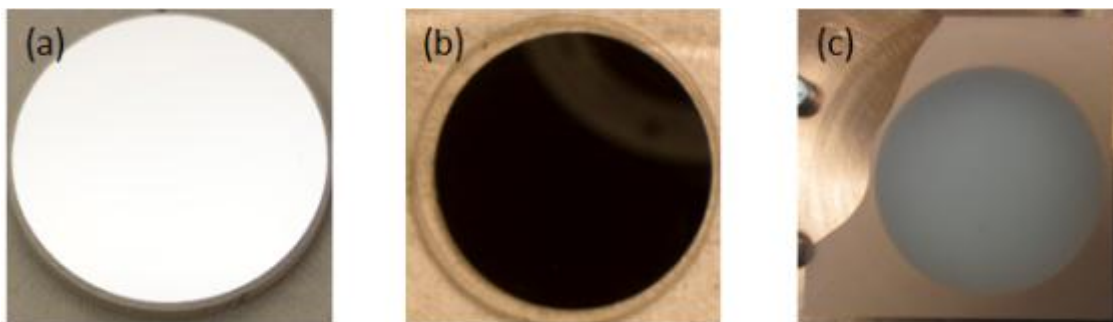
FIG. 3.1. Thin film SiO$_2$ samples. (a) Ag substrate with thin film disordered SiO$_2$ coating. **(b)** Au substrate with thin film disordered SiO$_2$ coating. (c) Bulk stand alone disordered SiO$_2$ sample.
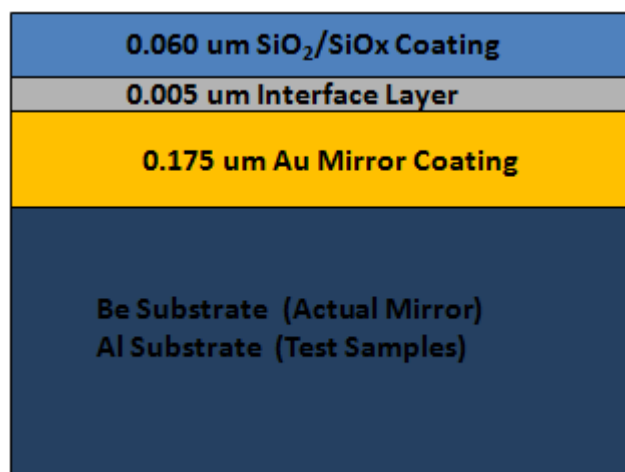
FIG. 3.2 Diagram of layered mirror samples.

and volatile contaminates. The samples were placed in the sample holder corresponding to the correct experiment and were placed in the ultrahigh vacuum chamber (see section 3.3.2) for > 24 hrs outgassing before measurements were made.

3.2. Measurements Made

Data presented in this thesis were acquired from different samples and under different experimental parameters. Table 3.1 shows which samples were used under what conditions and the data collected from those tests. Table 3.2 shows the different experiments presented in this paper. These tests add up to more than 100 test runs, more than 30 hours of testing and analysis, and more than 1 terabyte of data.

Table 3.2. List of all the tests that provide results in this text. The sample letter refers to the sample given in Table 3.1.

Sample	Beam Energy (keV)	Temperature (K)	Flux Density (nA/cm²)	Sample	Beam Energy (keV)	Temperature (K)	Flux Density (nA/cm²)
A	5	163	2	C	30	55	1
A	5	163	10	C	30	55	10
A	5	163	40	C	30	55	40
A	5	163	100	C	30	55	60
A	7.5	163	10	C	30	55	100
A	7.5	163	40	C	5	285	1
A	10	163	10	C	5	285	10
A	10	163	40	C	5	285	40
A	15	163	10	C	5	285	60
A	15	163	40	C	5	285	100
A	15	163	100	C	7.5	285	1
A	25	163	10	C	7.5	285	10
A	25	163	40	C	7.5	285	40
A	25	163	100	C	7.5	285	60
B	5	cooling	>200	C	7.5	285	100
C	5	55	1	C	10	285	1
C	5	55	10	C	10	285	10
C	5	55	40	C	10	285	40
C	5	55	60	C	10	285	60
C	5	55	100	C	10	285	100
C	7.5	55	1	C	15	285	1
C	7.5	55	10	C	15	285	10
C	7.5	55	40	C	15	285	40
C	7.5	55	60	C	15	285	60
C	7.5	55	100	C	15	285	100
C	10	55	1	C	20	285	1
C	10	55	10	C	20	285	10
C	10	55	40	C	20	285	40
C	10	55	60	C	20	285	60
C	10	55	100	C	20	285	100
C	15	55	1	C	25	285	1
C	15	55	10	C	25	285	10
C	15	55	40	C	25	285	40
C	15	55	60	C	25	285	60
C	15	55	100	C	25	285	100
C	20	55	1	C	30	285	1
C	20	55	10	C	30	285	10
C	20	55	40	C	30	285	40
C	20	55	60	C	30	285	60
C	20	55	100	C	30	285	100
C	25	55	1	C	25	cooling	>200
C	25	55	10	C	5	cooling	>200
C	25	55	40	C	5	cooling	>200
C	25	55	60				
C	25	55	100				

3.3. Instrumentation

3.3.1.   Overview

The system used for these studies is shown in FIG. 3.3. It allows for diverse space environments to be simulated and for precise measurements to be made in real time. Some of the system is automated by
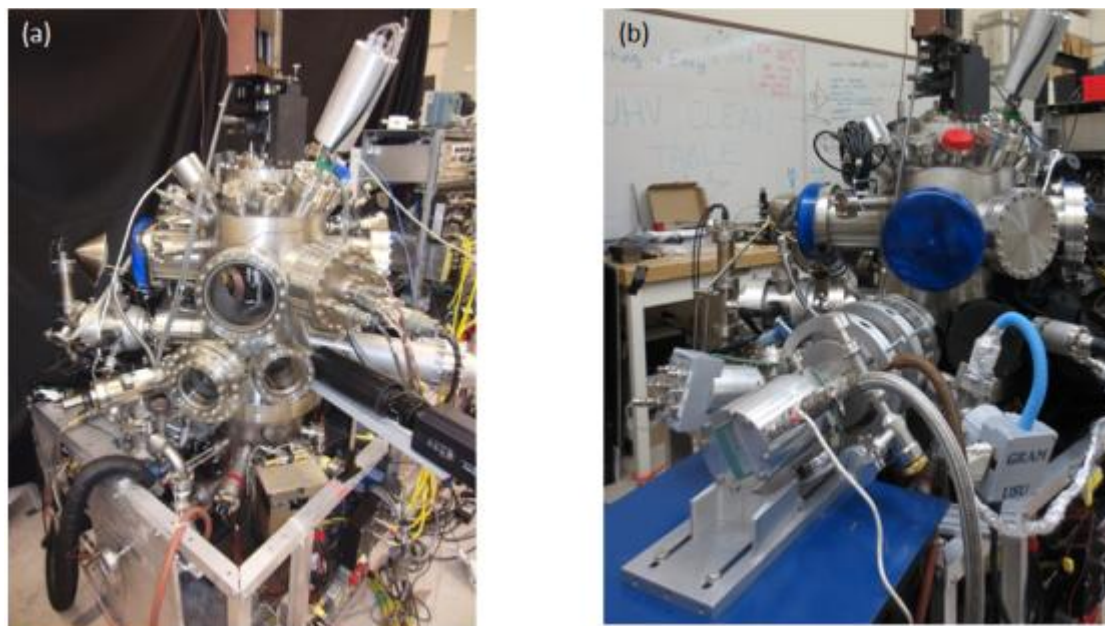
FIG. 3.3. Photograph of USU Materials Physics Group's electron emission test chamber. (a) Configured for Staib gun use. (b) Configured for HEED gun and cryostat use.

LABView^{TM} programs, which are interfaced with the various instruments. The many aspects to the instrumentation used to complete these experiments are shown in FIG. 3.4, providing a general schematic of the experimental system used. Each component is discussed below.

In order to do ground-based testing, several specific instruments are needed: an electron gun to simulate electron fluxes, an ultrahigh vacuum chamber to simulate the vacuum of space, an apparatus to control the sample temperature, temperature probes to measure the sample temperature, fast picoammeters to measure charge movement through the sample, as well as image charges in response to changing electric fields, and optical equipment to look at resulting arcs and other optical events.

3.3.2.   Vacuum Chamber and System

For the testing of spacecraft materials, two factors that need to be precisely controlled are the vacuum pressure and the temperature. The vacuum of space is typically $<10^{-7}$ Pa, but can be $>10^{-3}$ Pa in local space environments due to outgassing or mass ejection. Pressure variations have significant impact on contamination rates, susceptibility to arcing, and thermal transport. Temperature has far more drastic variations, which can range from 20 K to 350 K depending on which side of the spacecraft is being

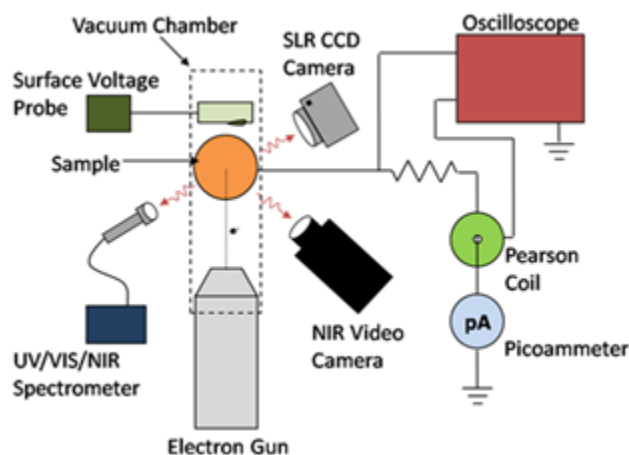FIG. 3.4. Block diagram of instrumentation for collecting the pulse charging surface voltage and electrode current data induced by electron beam bombardment. Instrumentation includes picoammeters, Pearson coils, a storage oscilloscope for electrode current measurements, UV/VIS and IR spectrometers, an SLR CCD still camera, and a NIR video camera for optical measurements.

illuminated by the sun and whether or not solar shielding is being used (Hastings and Garrett, 1996; Donegan *et al.*, 2010). It is, therefore, important to take these variables into consideration for the models, as well as the testing apparatus when conducting ground based simulations.

The USU materials physics group has designed and constructed several ultrahigh vacuum (UHV) (10^{-7} to 10^{-10} torr) systems in which spacecraft simulations can be conducted. Measurements include electrostatic breakdown, material conductivity and resistivity, electron-induced cathodoluminescence, radiation induced conductivity, and electron beam charging. Using these systems, we can effectively simulate numerous space-like scenarios and measure the needed quantities to validate proposed models, as well as determine sample characteristics (Chang *et al.*, 2000; Dekany *et al.*, 2014b; Dennison *et al.*, 2014b; Hodges *et al.*, 2014). The MPG electron emission test chamber has been modified for observations of low intensity UV/VIS/NIR glow over a broad range of sample temperatures (Wilson and Dennison, 2010; Dekany *et al.*, 2014b). This chamber uses standard mechanical and turbomolecular pumps for roughing and an ion pump for continuous maintenance-free operation (base pressure of $<10^{-7}$ Pa). Absolute pressure is monitored with Convectron TM and ion gauges. Partial pressure is measured with a residual gas analyzer.

For the present CL tests, it is important to keep ambient light from interfering with the signal from the CL. This is done by putting dark caps over unused port windows and placing black plastic or cloth around the instrumentation.

3.3.3. Sample Holders

One sample holder used, the carousel, is a right dodecagon with eleven sample blocks, which can be rotated in front of the various flux sources (FIG. 3.5). Typically, one sample block contains a photodiode, another contains a Faraday cup, and a third has a Au sample used as an electron emission standard. The carousel has been designed so it can be easily removed from the chamber. One module in the carousel is omitted to make way for a slot from the center to the edge that allows the sample carousel to be removed from the circular base on which it rests. The center region of the sample carousel is hollow to allow for the various wires from the back side of each module to be accumulated and passed through the top plate via a 25-pin, UHV-compatible, D-type subminiature connector (Insulator Seals Part # 0981901). The 25-pin connector allows for quick removal of the sample stage and clean, hassle free, wiring of all samples. A 25-lead Kapton^{TM} coated ribbon cable connects the internal D-pin connector to a UHV feedthrough (MDC Vacuum Part #D25-450-ISI 913208) (Hodges, 2012).

FIG. 3.5. Sample carousel used to house samples for tests A and B.

Samples are mounted on OFHC Cu stands, using a Cu tape with conductive UHV-compatible adhesive routinely used for scanning electron microscope studies (3M, Type 1182 tape). The top part of the Cu stands are a 25 mm diameter cylinder. The bottom is a 10 mm diameter cylinder. The Cu cylinders are mounted in sample blocks on the sample carousel, using ceramic pins to provide electrical isolation. FIG. 3.6 shows the stands and the blocks for mounting. Electrical connection to the sample is made via a spring-loaded pin from the rear, allowing the current to the sample to be monitored using custom electrometers (Thomson, 2001; Nickles, 2002).

The other sample holder, termed sample round, is very different from that described above, as can be seen in FIG. 3.7. The sample block (**B** in FIG.3.7) is electrically isolated with a Kapton^{TM} spacer and PEEK screws, but maintains good thermal contact with the sample stage. The sample round has a large wiring cavity to facilitate various low-noise electrical connections, in addition to allowing room for bulk and control heaters. A 10 mm Cu cylinder is mounted in a sample block using ceramic pins or 100 μm diameter sapphire spheres held in place with set screws to provide electrical isolation. Electrical connection to the sample is made via a spring-loaded pin from the rear, allowing the sample current to be monitored. The sample mount has four holes on the back, used for other experimental configurations. For this experiment, only one corner hole is used. The Cu cylinder in this sample hole has a hole in it where a spring and pin are placed to make electrical contact with the back of the sample (FIG. 3.8). On top of this is a conversion piece for square samples [**H** in Fig. 3.9(a)], then a Kapton^{TM} washer with one hole for contact [**I** in FIG. 3.9(a)] is placed for electrical isolation. A layer of copper foil [**J** in FIG. 3.9(a)] is placed
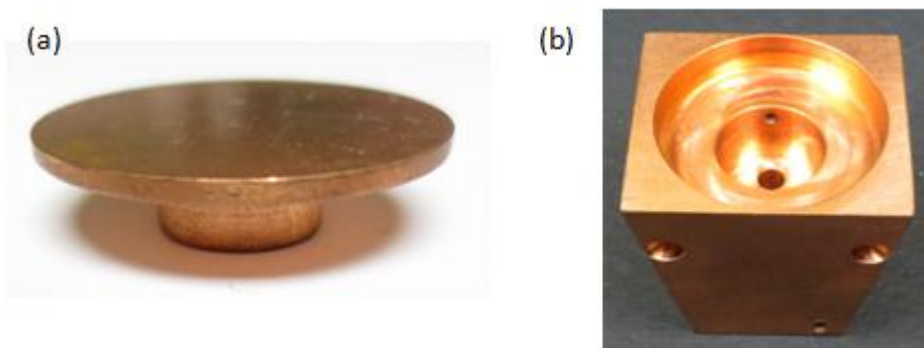
FIG. 3.6. Sample holders for tests A and B. (a) **T**he Cu pedestals used for mounting the samples when using the sample carousel. (b) The Cu wedges in which the Cu pedestals are held.
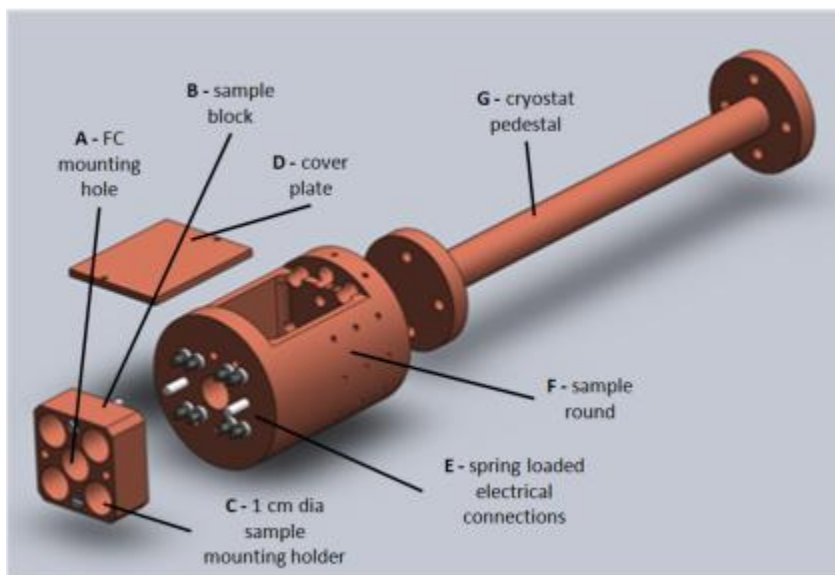
FIG. 3.7. Sample round used for test C. View of the cryostat's second stage sample pedestal and interchangeable sample holder, which attaches to the cryostat. Shown is a sample holder for four 1 cm diameter samples and a central Faraday cup. Different components are identified.

next for a conductive backplate to measure the current coming off the back of the sample. The fused silica sample lays on top of the copper backplate [**K** in FIG. 3.9(a)]. Another Kapton^{TM} washer with a 2 cm hole cut into the center lays on top of the sample [**L** in FIG. 3.9(a)]. It is slightly larger than the top plate hole so there is no Kapton^{TM} exposed to the electron beam. The top plate is then placed on top, with the center hole to expose the sample to the beam [**M** in FIG. 3.9(a)]. The front surface of the top plate

FIG. 3.8. Cu cylinder (top corner) that holds the spring-loaded pin, which makes electrical contact with the back of the sample. This is mounted in the sample round along with the FC (middle), and the other sample slots are left empty.

FIG. 3.9. Solid model of sample mounting and image of the Aquadag^{TM} surface. (a) The solid model shows each layer of the mounting assembly for Sample C as called out in the text. (b) The front surface of **L** was sprayed with a coating of Aquadag^{TM} to reduce reflections.

is coated with Aquadag[TM] to minimize both optical and electron beam reflections from the surface [FIG.3.9(b)].

3.3.4. Sample Cooling
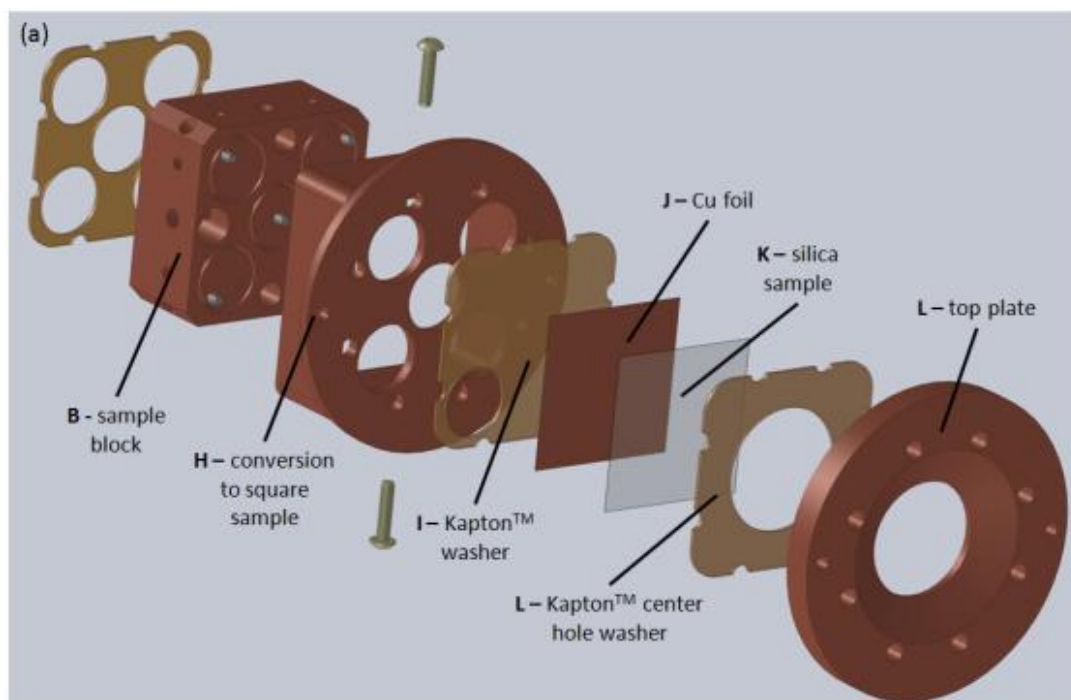
Two methods of cooling the sample were employed during these tests. The first was a liquid nitrogen cooling system; the second employed a closed-cycle helium cryostat. Both are addressed below.

The sample carousel described in section 3.3.3, was thermally anchored to (but electrically isolated from) a thermal reservoir (FIG. 3.10). The samples are cooled by running liquid nitrogen through the reservoir. In combination with resistive heaters and liquid N_2, the samples were maintained over a range of temperatures from ~150 K to ~300 K with a long-term stability of ± 3 K.

A closed-cycle helium cryostat (FIG. 3.11) has been added to the electron emission test chamber to extend the operational temperatures for sample testing from <40 K to >450 K (Dekany *et al.*, 2014b). Temperature is maintained to ± 0.5 K using a standard computer-controlled PID temperature controller (RMC Cryosystems CR31-21) under LABview[TM] command and platinum RTDs mounted on the sample holder, low temperature stage, and cryostat radiation shield. A large mass radiation shield was attached to the cryostat's first stage (thermal load capacity of ~10 W at ~80 K) and a sample mounting stage was attached to the cryostats second stage (thermal load capacity of ~1 W at ~20 K); these large thermal masses helped maintain a constant sample temperature. Due to radiative heat transfer from the chamber walls, the

FIG. 3.10. Liquid nitrogen cooling reservoir used for sample tests.

addition of a multilayer thermal insulation blanket wrapped around the first stage radiation shield was required. This blanket consists of five sheets of thin conducting material separated by a thin mesh of insulating material. With this addition to the apparatus, the sample holder, which is mounted to the cryostat's second stage sample pedestal, can reach 40 K, a temperature comparable to passively cooled spacecraft in standard orbit. Direct measurement of a sample confirmed a <2 K gradient between the samples and sample holder on which the temperature probe was mounted. Once the chamber was down to pressures of <5·10^{-3} Pa, the cryostat cooled the sample at a rate of ~ 1 K/min, reaching the lowest temperature of ~40 K in about 4 hr; this temperature can be sustained for weeks. Heating the sample is accomplished using a combination of control and bulk heaters attached to the radiation shroud and sample mount. Once activated, the temperature controller can heat the sample at a rate of ~ 1.5 K/min. FIG. 3.12 shows a typical cooling and heating profile.

3.3.5.   Electron Sources and Detection

3.3.5.1.   Source Descriptions

Two electron sources are available on this chamber. One is a low-energy electron gun (Staib, EK-5-51), which produces a beam that ranges in energy from 20 eV to 5 keV and flux of ~50pA/cm^2 to 1 μA/cm^2 [FIG. 3.13(a)]. This defocused electron beam produces a beam profile at the sample with about ±30% uniformity over an ~3 cm diameter beam spot. The W filament of the electron gun also produces visible light that travels down the bore of the electron gun and impinges on the sample; even at the low operating filament temperatures used for the low flux beam (~2500 K), the intensity of the filament spot on the sample was initially larger than the luminescent signals. To minimize this background filament light, a blocking aperture was developed, which allows an electron beam to be focused ~5° off axis and then electrostatically deflected back on to the sample while sending the filament light into an optical baffle. The baffle and the primarily specular nature of the reflected filament light that makes it past the blocking aperture reduces the stray light background seen by the optical cameras to acceptable levels. This baffling is discussed more in (Wilson, 2013).
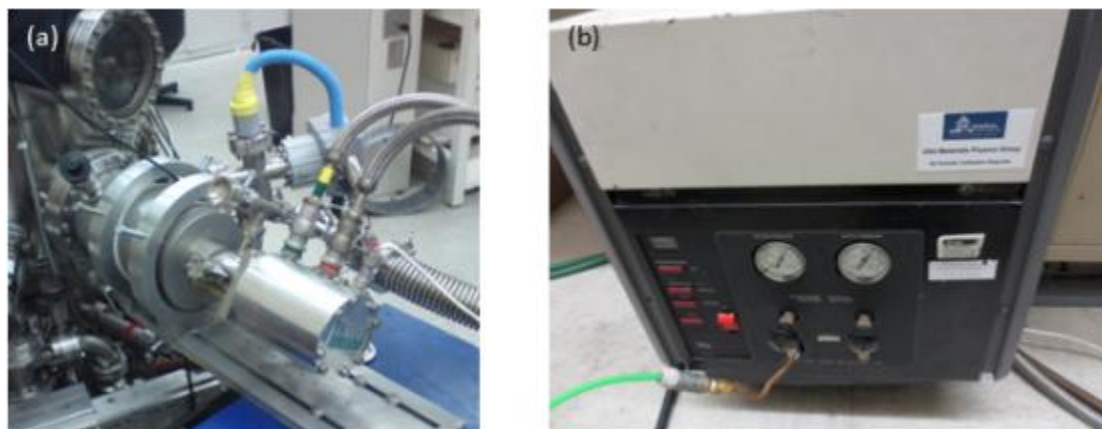
FIG. 3.11. Closed-cycle helium cryostat. (a) Extension view of cryostat mounted on electron emission test chamber. (b) Cryostat He compressor.
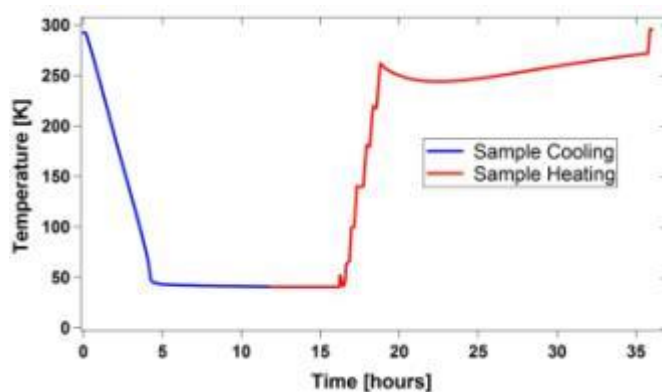
FIG. 3.12. Typical sample stage cooling and heating curves. Multiple sustained temperatures are shown during heating cycle.

The other electron source used is a high-energy gun (Kimball, Model EGPS-21B), which provides a monoenergetic beam with a flux of ~50pA/cm^2 to 1 μA/cm^2 over an energy range of 5.00 to 30.00$\pm$0.01 keV (FIG. 3.13(b)). This gun uses a LaB$_6$ filament, which also produces a light spot, but is not the problem the W filament is in the other gun.

3.3.5.2. Source Characterization

In order to accurately determine the amount of flux incident on the sample for each experiment, the electron beam is characterized. The characterization process differs for the different electron sources
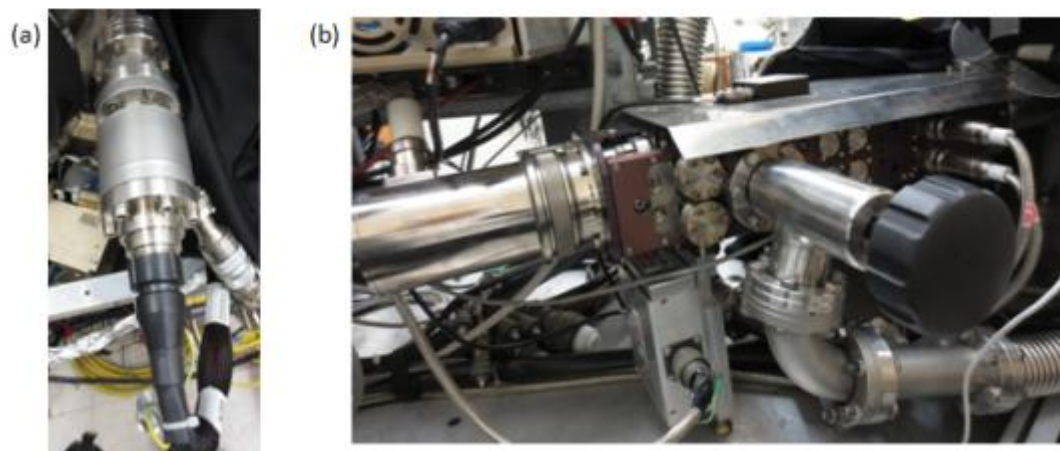
FIG. 3.13. Electron sources used during these tests. **(a)** Low energy electron gun (STAIB gun). **(b)** High energy electron gun (HEED gun).

used and the different locations of the sample. The details concerning the beam characterization of the STAIB gun is found in (Wilson, 2013). The HEED gun characterization is detailed below.

For each beam energy, electron gun settings (Table 3.3) need to be found to produce a spot to fill the entire exposed sample area with as much uniformity as possible. Since the electron gun was made for a small (~1 mm) collimated beam, settings from previous experiments could not be used (see Hoffmann, 2010). Using the video camera to watch the glow from the sample, the beam is adjusted to uniformly fill the entire sample area (FIG. 3.14). This is done for each beam energy. The defocused electron beam produces a beam profile at the sample with about ±30% uniformity over an ~3 cm diameter beam spot.

Once these settings are determined, beam profiles are taken for each energy to determine the

Table 3.3. Electron gun settings to fill the entire sample area with the beam.

Energy (keV)	Source (A); Knob	X Alignment	Y Alignment	X Deflection	Y Deflection	Lens
5	1.6; 9.075	-94	123	0.02	0	0.82
7.5	1.6; 9.075	-92	126	0.02	-0.01	1.07
10	1.6; 9.075	-90	128	0.03	-0.01	1.23
15	1.6; 9.075	-85	132	0.03	-0.02	1.49
20	1.6; 9.075	-80	143	0.04	-0.02	1.73
25	1.6; 9.075	-75	151	0.05	-0.02	1.81
30	1.6; 9.075	-70	161	0.05	-0.03	1.95

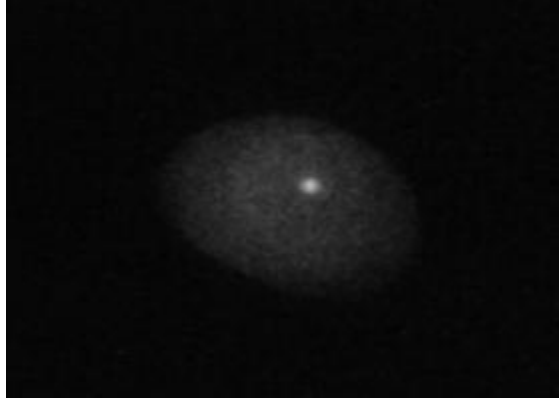FIG. 3.14. A single frame from the CCD video camera directed at the sample. The bright spot in the center area is the light from the LaB_6 filament. The other bright region is the CL emitted from the fused silica. This image verifies the beam is filling the entire sample, relatively uniformly.

correction factor (*CF*). The beam profile is measured using a FC residing in the analysis chamber and mounted on a computer-controlled translation stage (the carousel discussed in Section 3.3.3 for experiments A and B) with 0.7 μm resolution (Thomson, 2001; Nickles, 2002). Using translation and rotation, the beam is centered in the *FC* using as little beam deflection as possible to limit beam distortion. Once centered, the *FC* is moved in 0.19 mm steps with the current from the beam measured at every step. This is done using an automated LABView^{TM} routine using the same program as above: the FC is vertically translated across the beam as data is acquired using GPIB interfacing and a data acquisition (DAQ) card (National Instruments, Model BNC2110) under LABView^{TM} control (Wilson, 2013).

Each beam profile is fit with the Gaussian curve of Eq 3.1 [FIG. 3.15(a)].

$$J_G(r, J_0, r_m, \sigma) = J_0 \cdot \frac{1}{\sigma \cdot \sqrt{2 \cdot \pi}} \cdot e^{\frac{-(r - r_m)^2}{\sigma^2}} , \qquad (3.1)$$

where J_G is the current density at radius, r, J_o is the normalized total current centered at r_m, and σ is the standard deviation. The total current in the *FC*, I_{fc}, is determined by integrating Eq. 3.1 over the *FC* radius, r_{fcs}, and assuming cylindrical symmetry of a centered beam as

$$I_{fc} = \int_{0mm}^{r_{fcs}} J_G \left[r, J_0 \cdot \left(\frac{L_1}{L_2} \right)^2, 0mm, \sigma \cdot \left(\frac{L_2}{L_1} \right) \right] \cdot 2 \cdot \pi \cdot r dr . \qquad (3.2)$$
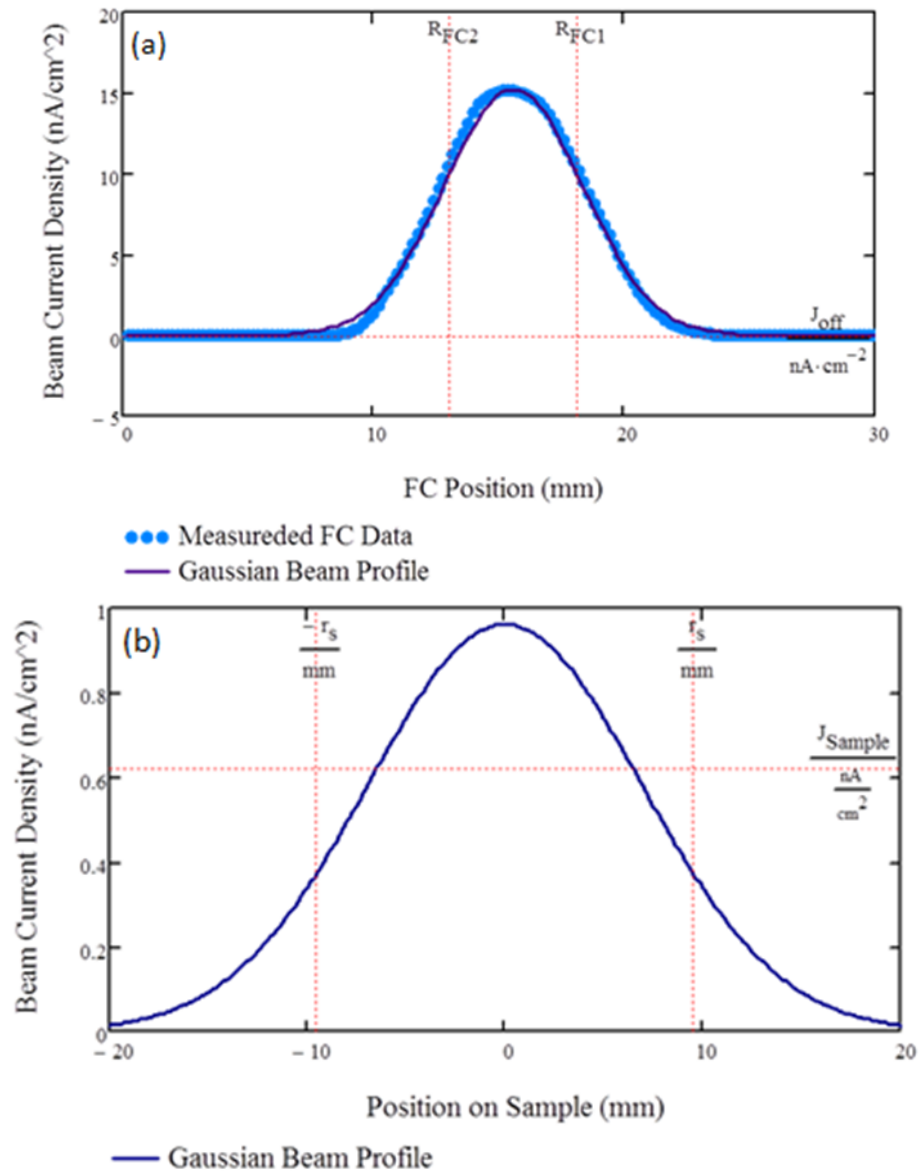
FIG. 3.15. Plots for beam characterization. (a) Beam profile at FC fit with a Gaussian function. (b) Projected beam profile at the sample.

The current incident on the sample, I_{sample}, is given by

$$I_{sample} = \int_{0mm}^{r_s} J_G \left[r, J_0 \cdot \left(\frac{L_1}{L_2}\right)^2, 0mm, \sigma \cdot \left(\frac{L_2}{L_1}\right) \right] \cdot 2 \cdot \pi \cdot r dr \ . \tag{3.3}$$

The *FC* and sample are at distances L_1 and L_2 from the electron gun filament, respectively. Then, the current densities at the *FC*, J_{fc}, and sample, J_{sample}, are determined to be

$$J_{fc} = \frac{I_{fc}}{A_{fcs}}$$

(3.4)

and

$$J_{sample} = \frac{I_{sample}}{A_{sample}} .$$

(3.5)

This is shown in FIG. 3.15(b). A_{fcs} is the area of the *FC* and A_{sample} is the area of the sample. The correction factor (*CF*) is then

$$CF = \frac{J_{fc}}{J_{sample}} .$$

(3.6)

The *CF* is used in the LABView^{TM} data collection program to take a measured current density at the *FC* and convert it to current density that the sample will see in real time without having to repeat a full beam profile measurement. A list of correction factors for each beam energy used is given in Table 3.4. Once the *CF*s are determined, measurements are again made with the *FC* to find the correct settings for the desired current densities at each energy for each measurement. This has to be done before testing starts

Table 3.4. List of correction factors for each beam energy used in these experiments.

Energy (keV)	Correction Factor
5 ± 0.01	1.26
7.5 ± 0.01	1.225
10 ± 0.01	1.236
15 ± 0.01	1.26
20 ± 0.01	1.248
25 ± 0.01	1.321
30 ± 0.01	1.321

because there is no *FC* at the sample position.

3.3.5.3.   Electron Detection

Electrode currents are measured during the entirety of the run from a copper electrode on the back of the sample to ground. Measurements are taken using fast sensitive picoammeters with <0.2 pA resolution (Thomson *et al.*, 2003) and recorded using GPIB interfacing and a DAQ card under LABView[TM] control similar to the beam profile measurement process using the LABView[TM] program "IESBD_DC Profiler v1.6." A screenshot of this program is shown in FIG. 3.16. While electrical measurements are not the focus of these experiments, they were recorded mainly for the purpose of the analysis program used. The text file that is output by the LABView[TM] program that runs the electrometer is ready to use in data analysis as is.

3.3.5.4.   Optical Detection

Light detection uses the two cameras shown in FIG. 3.17. The cameras are positioned with clear views of the sample through vacuum port windows, thus allowing collection of photon emission data resulting from CL and arcing (Evans *et al.*, 2012).

The Single Lens Reflex (SLR) CCD camera (Cannon, EOS Rebel XT DS126071; ~400 nm to 700 nm, 30 frames per s) takes visible light 10 Mpixel images at 30 s shutter speeds at full aperture with a 55 mm lens, giving it an average spectral response of $\sim 4 \cdot 10^9$ counts/(W/cm$^2 \cdot$sr$\cdot \mu$m). It is connected via USB to a computer with the EOS Utility and ZoomBrowser EX programs installed. The EOS Utility program controls the picture acquisition and ZoomBrowser EX displays a preview of the image after the picture is taken. The images are output as raw .CR2 files. FIG. 3.18 is a screen shot of the computer screen running the SLR still camera utilities.

The image-intensified CCD video camera (Xybion, ISG-780-U-3; ~400 nm to 900 nm) collects data at 30 frames per sec using a 55 mm lens and has a spectral response of $\sim 4 \cdot 10^{10}$ counts/(W/cm$^2 \cdot$sr$\cdot \mu$m). This camera outputs the digital video files through the ULEAD program. FIG. 3.19 is a screen shot of the program that runs the CCD video camera.
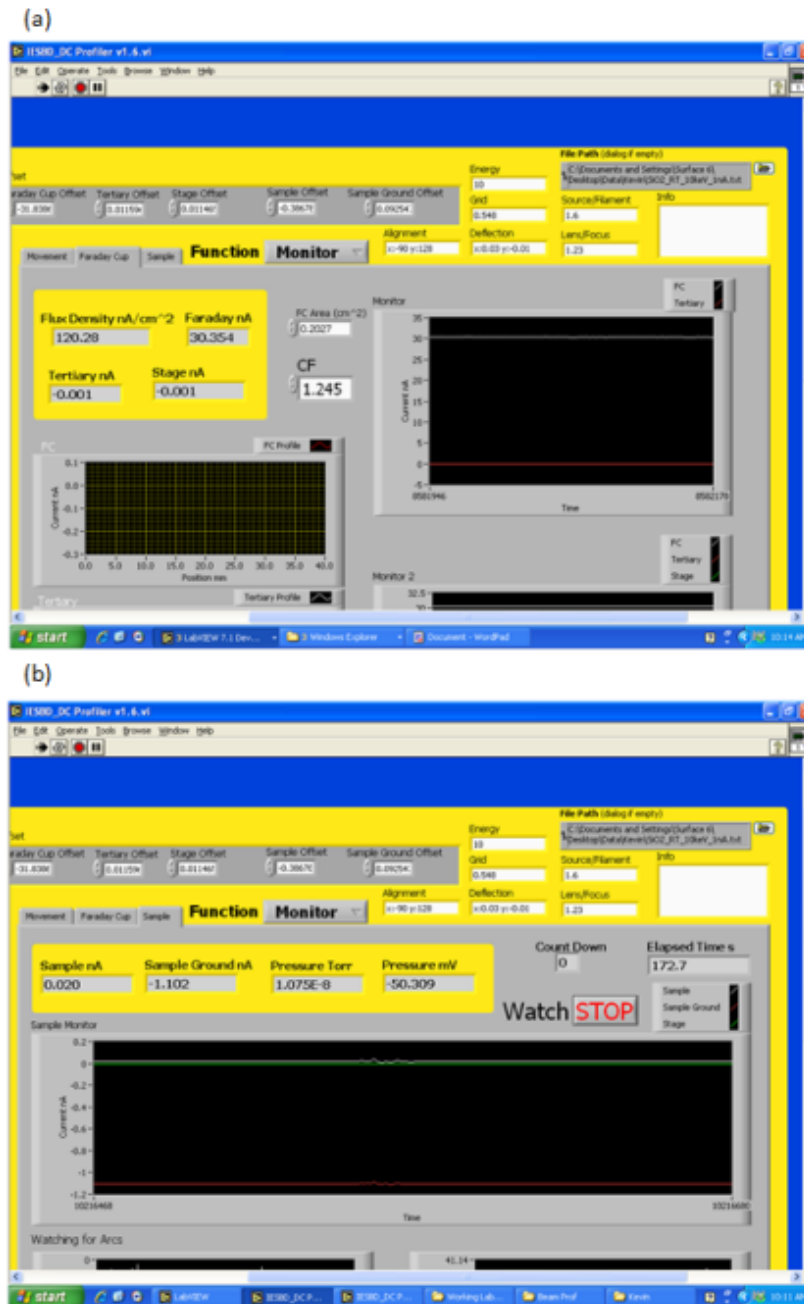
FIG. 3.16. Electrometer program screen shot. (a) Screen shot of program used for beam profiles. (b) Screen shot of program used for collecting sample electrometer data.

Visible range calibrations for the SLR CCD camera and CCD video camera were done using a 6 in diameter Spectralon™ integrating sphere (Labsphere, Model SC6000) with a NIST traceable calibration curve for absolute spectral radiance, using an integrated W-halogen lamp powered by a NIST traceable

CCD Video Camera   **SLR CCD Still Camera**

FIG. 3.17. Cameras used for optical detection. CCD video camera (left) and the SLR CCD still camera (right) as they are set up to look at the sample.

calibrated current source (Keithley, Model 6430). A smaller 1.5 in diameter Spectralon^{TM}-lined fiber optic integrating sphere (Ocean Optics, Model FOIS-1) connected to a calibrated W-halogen blackbody (2530 K) source (Ocean Optics, Model LS-1-CAL-INT) was used as an *in vacuo* secondary standard. This calibration allows for absolute spectral radiance values to be obtained (Dekany *et al.*, 2014b).

A UV/Vis fiber optics-based spectrometer (Stellarnet, 13LK-C-SR; ~200 nm to ~1080 nm) provides photon spectral measurements from ~200 nm to 1080 nm (FIG. 3.20) with a wavelength resolution of ~1 nm. Because the luminescence is so low, the spectrometer has to be set at its longest integration time, 65363 ms, to collect spectra. The spectrometer is connected to a computer via USB and is controlled through the Stellarnet program, SpectraWiz. The files output by the spectrometer are .SSM files, which can be read directly into IGOR, the analysis program. If this is the first time this computer has run the spectrometer, check that the calibration constants are correct. The procedures for installation and set up are located on the MPG BigBlue file server.

3.4.   Data Acquisition Procedures

Two types of tests were conducted for this thesis. The first are temperature-dependent cooling runs, where the sample temperature is varied as data are collected at a constant beam energy and flux. The second set is conducted at fixed temperature (~55K, cryogenic tests) and the beam energy and flux are changed for each test.

Set up for the cooling method is completed prior to beginning the run. When cooling via liquid nitrogen, hoses are connected and the fume hood is turned on to remove the excess nitrogen released into the lab. Also, confirm there is enough liquid nitrogen in the dewar to complete whatever tests are planned. When running the cryostat, it is charged to the correct pressure of high purity helium as needed. The cooling water for the cryostat is set to flow at a medium pace; without proper flow, the compressor will not function. The temperature controller box and cryostat compressor are then turned on to begin the cooling process.
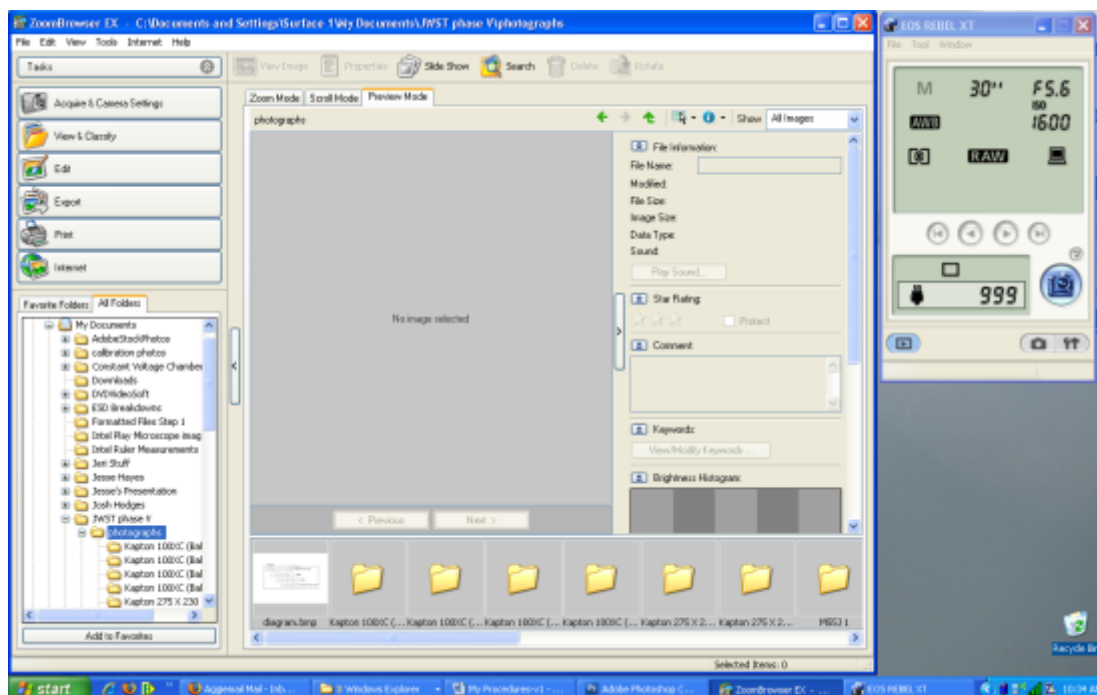

FIG. 3.18. SLR CCD camera program. Zoom Browser (left) and EOS Utility (right) programs opened side by side. As the camera takes pictures, the picture will open in the large gray box in Zoom Browser where it can be previewed.
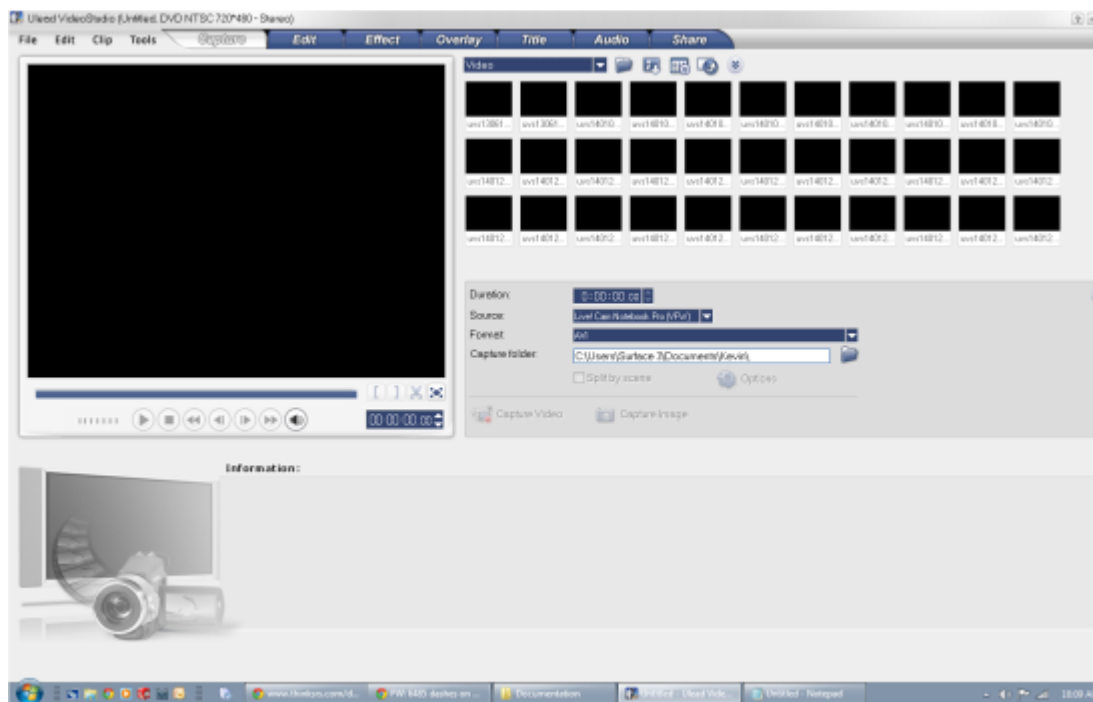
FIG. 3.19. Program used to run the CCD video camera.

For each type of test, the prerun preparation was the same. If the electron beam has been off, before any tests can be done, it must be allowed time to properly warm up and stabilize. Procedures for warm up are found in the electron gun instruction manuals (Kimball; STAIB Instruments). While warming up the gun, alignment of all optical instruments is confirmed. To do so for the Xybion CCD video camera, the image of the sample is monitored with enough light in chamber to see the sample, but not so much that the image of the camera is saturated. This is monitored by watching the computer screen on which the collection program was running.   The camera alignment is adjusted to center the sample in the field of view and set the focus for the sharpest image. The SLR CCD camera is aligned and focused by physically looking through the view finder on the camera. Care is required, however, not to bump and move the camera stand on which both the still and video camera are mounted. A sample picture is taken and examined on the SLR collection computer to be sure the focus is the highest quality possible. To align the collection optics used for the spectrometer, an Ocean Optics LS-1 lamp is attached to the collection fiber optic. This shines light back down the optics and onto the sample. The position of the collection optics is

FIG. 3.20. Spectrometer from StellarNet used for the UV/Vis spectra.

adjusted so the light from the LS-1 lamp is centered on the sample using the Xybion video camera to see where the light is projected. Once the beam is warmed and stabilized, the cooling begins.

Next, the naming and saving of the files for the SLR and electrometer are set up. On each computer, a folder is created that contains the runs that are to make up the measurements set. This folder is selected as the folder in which to save files. The file is named according to material name, sample temperature, beam energy and beam current density; for example a proper file name is fusedsilica_52K_5keV_1nAcm2_electrometer.

In the electrometer program, the available boxes for the beam alignment, deflection, etc. are completed. These appear in the header of the electrometer file.

For the SLR camera EOS Utility program, the F stop is set at F5.6 with a shutter speed of 30 seconds, 30". However, some of the images become saturated so it is suggested, depending on the sample and the intensity of its luminescence, the shutter speed be reduced by approximately half so as not to saturate the image. The test file name (same as that of the electrometer with _SLR rather than _electrometer) is set as the File Prefix in the Sample Shooting menu and the start number is set to 1. Pressing OK initiates image collecting.

Prior to turning on the electron beam, a light image of the sample is taken with both the SLR and video cameras. This is done so the sample can be easily located during analysis, if the luminescence is not bright enough to locate the sample. Once these are completed, a dark spectrum is recorded and zeroed out

from the spectrometer. This is done by first waiting for the spectrometer to update so the dark spectrum does not contain any of the light from the light images, and then clicking on the save dark spectrum icon located in the tool bar at the top of the screen. Subtracting the dark spectrum in this manner allows one to see if the spectrometer is, in fact, able to collect a spectrum once the luminescence has begun. A dark SLR image is also taken during this time. The ULEAD program for video collection is opened and the Video Editor option selected. From there, the Capture tab is selected followed by the Capture Video. Still, before the electron beam is turned on, the electrometer offset is reset and recording is begun. The video camera is started, as well. After at least 30 s of recording with the beam blanked, the beam is then unblanked. Still camera images are taken and, after allowing for the spectrometer to update, spectra are collected. The spectra files are named using the convention for the electrometer files. The beam is then blanked again. Recording continues with the video camera and the electrometer for 30 s. These beam off times before and after the beam on times are used for the dark subtraction during analysis. This completes a set of data or a run. Once the video recording is stopped, the file is named using the same convention as described above.

Cooling runs consist of decreasing the temperature of the sample continuously at a rate of ~1 K/min when using the cryostat. The electrometer program, in this case, is started at the beginning of a cooling run (room temperature) and runs continuously through the entire cooling process (~4 hr). Other than that, the data collection cycle is as described above. Starting at room temperature, as the temperature drops, data is collected in 15 K intervals, each 15 K interval being one run. This continues until the final, lowest temperature (~55 K) is reached.

Cryogenic tests occur at ~55 K. For each run, data collection is done as described above. Instead of allowing time to pass for the temperature to change following each set of data collection, however, beam settings are adjusted to the new parameters (either changing energy or flux) for the next data set, the beam is given time to stabilize, then data collection begins again. The spectrometer is not used for these measurements due to the low light intensity emitted from the sample at reasonable current densities. The beam currents used in these tests are not large enough to produce light intense enough for the spectrometer to detect. If flux is sufficiently large for spectrometer detection at higher energies, arcing will occur. This tendency to arc grows as beam energy increases.

3.5. Analysis of Optical Data

Data processing and analysis is an extremely involved process with multiple steps, which eventually lead to the desired final plots. As can be seen from the flowcharts of FIG. 3.21 and FIG. 3.22, the files from both cameras must be converted to JPEG images. These are then run through a pixel counter, which outputs a single text file with the proper pixel data. These text files, along with the electrometer text file, are all loaded into the IGOR^{TM} macro, which applies the proper calibrations to the data and produces plots of the spectral radiance against the run time. From this point, by gathering spectral radiance data for different runs, spectral radiance can be plotted as a function of incident beam current density, incident beam energy and sample temperature, three of the parameters in the model (Eqs. 2.1 and 2.2).

The spectra files from the spectrometer can be loaded directly into IGOR^{TM} as a General Text file (there is no macro for spectra analysis; simply open IGOR^{TM} and load the file). The raw spectra can be viewed by plotting wave 1 against wave 0. To fit the raw spectra, the Mulitpeak Fitting package is used. In this package, peaks are identified and the sum of the peaks provides a total fit to the raw spectrum, which provides peak location, intensity and width information.

The analysis process for each instrument's data is provided in Appendix A.
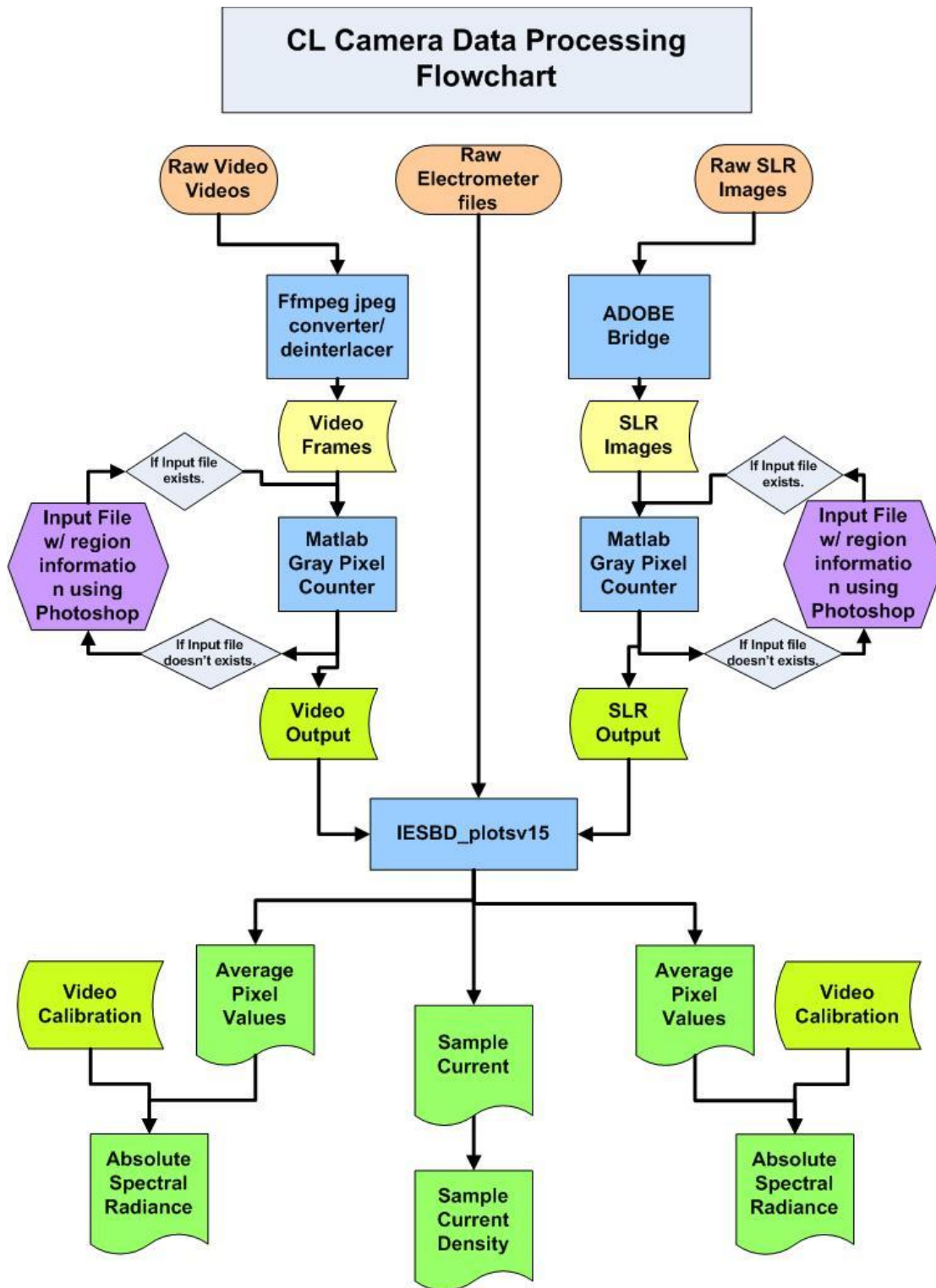
FIG. 3.21. Flowchart for processing the camera CL data.

CL Spectrum Processing Flowchart

Raw Spectrum File

IGOR Pro

Raw Spectrum Plot

If peak fit is good

Do Fit

"Multipeak Fitting" Package

Auto-find or manually locate peaks

Complete Spectrum Fit Output
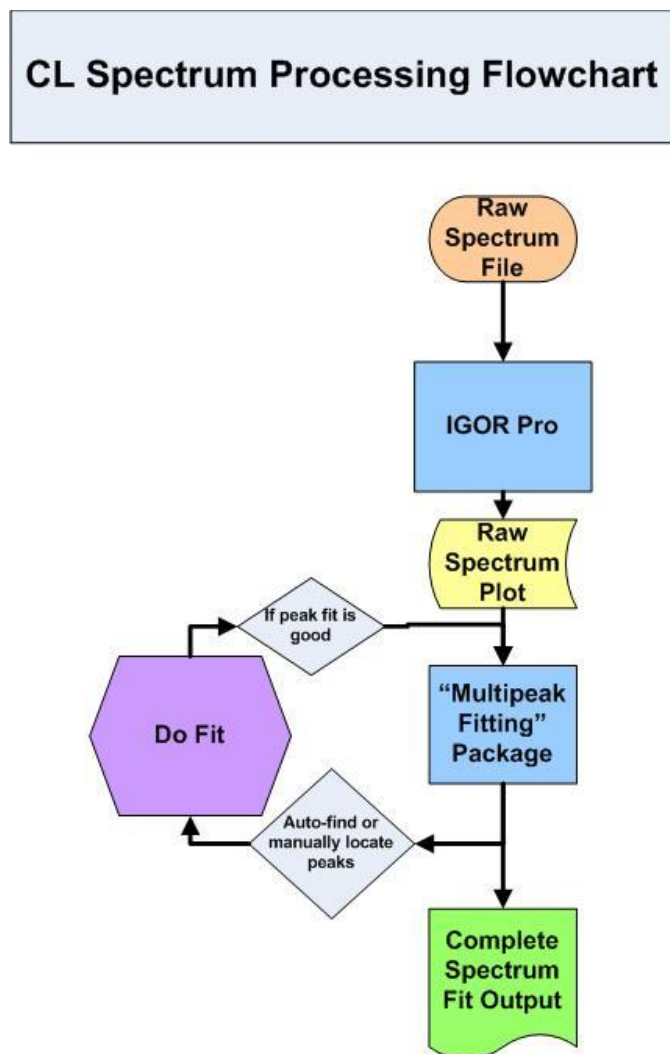
FIG. 3.22. Flowchart for processing the spectrometer CL data.

CHAPTER 4

RESULTS

In this chapter, the results of the experiments are presented. First are the results that fit within the proposed model. These are divided into four parts, showing the overall CL intensity dependence on incident beam current density, incident beam energy, material temperature, and finally how the spectra fit the four-band model. In each section, results from literature are also presented and compared with the results from these experiments. The last part shows the results that do not fit into the model presented, but are significant and interesting behaviors and deserving of mention here.

4.1. Results Within the Model

This section presents the results of the model, including fitting the results into Eqs. 2.1 and 2.2, as well as into the four DT band model.

4.1.1. Incident Beam Current Density

As stated previously, SiO_2 has a band gap ≈ 8.9 eV and therefore, excitation from the VB to CB is not thermal, but rather occurs through collisions with the incident high-energy electrons. Thus, at low currents, I_γ is proportional to the incident current density, J_b, through the dose rate (Eqs 2.1 and 2.2). At very-high-current density, saturation can occur when trap states fill, limiting the number of states electrons can decay into, leading to I_γ approaching a constant value. This saturation effect was discussed extensively in Section 2.3.1.

Current dependent saturation is shown in FIG. 4.1, where the spectral radiance as a function of beam current density for various incident beam energies is fit using Eqs. (2.1) and (2.2). The saturation effect is seen as the departures from the initial linear dependence on current density. Note there is a single $\dot{D}_{sat}$ value for each sample, and as the dose rate changes from thickness-dependent (thick sample) to range-dependent (thin sample) behavior, $\dot{D}_{sat}$ increases dramatically.

The saturation effect is most pronounced in FIG. 4.1(a) for the thin, ~60 nm thick sample in Experiment A with a $\dot{D}_{sat}$ value of $4 \cdot 10^3 \pm 44\%$ Gy/s. This then gives saturation current densities of ~100, ~190, and ~260 nA/cm^2 for incident beam energies of 5, 15, and 25 keV, respectively, using Eq. 2.2. The

48
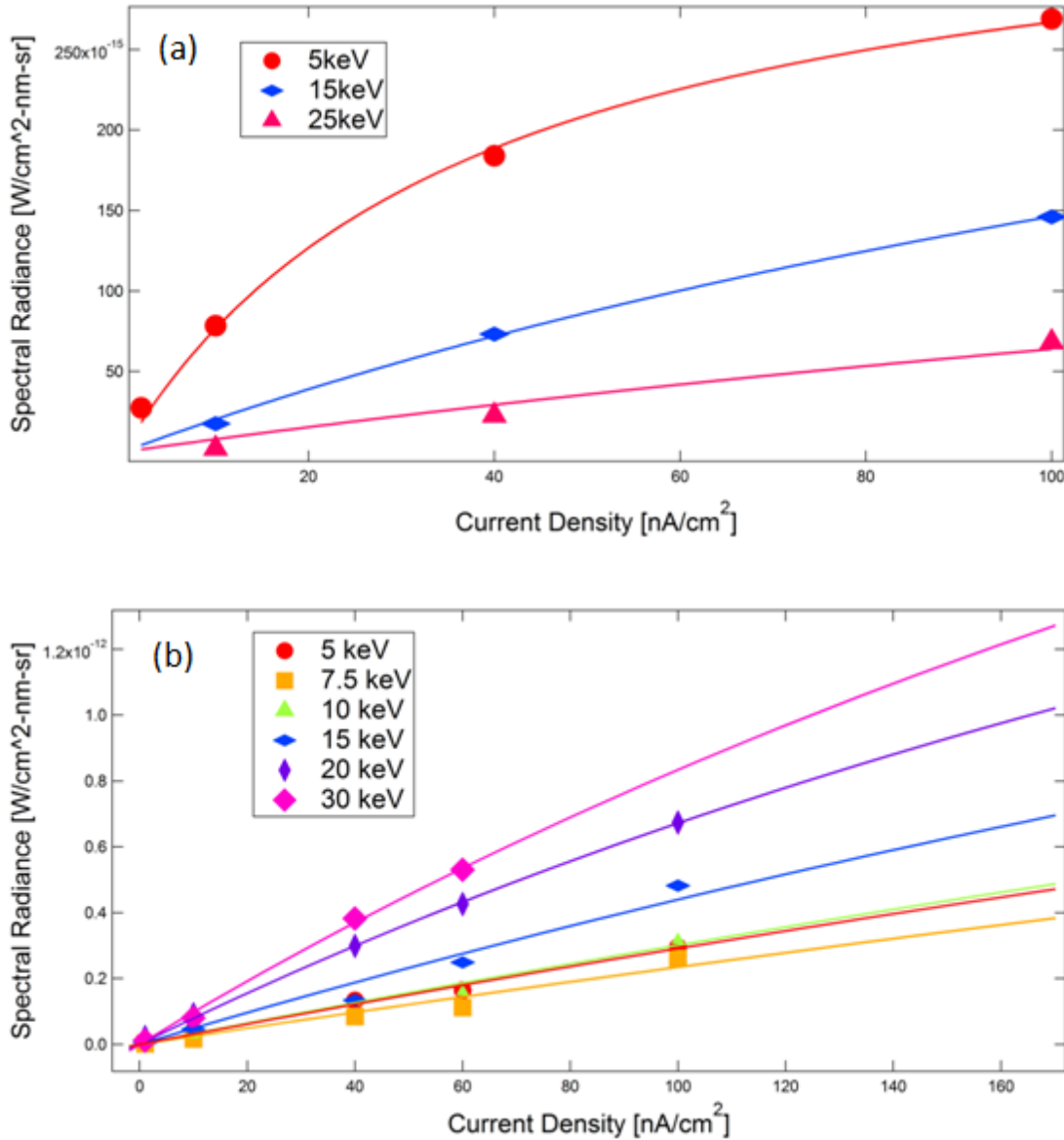
FIG. 4.1. Spectral radiance as a function of beam current density for various incident electron energies. (a) For the ~60 nm thick sample of SiO$_2$, penetration occurs at ~1.3 keV beam energy. The fits yield a value for $\dot{D}_{sat}$ of $4 \cdot 10^3 \pm 44\%$ Gy/s. (b) For the ~80 μm thick sample of SiO$_2$, penetration occurs at ~118 keV beam energy. The fits yield a value for $\dot{D}_{sat}$ of $580 \pm 25\%$ Gy/s.

reason the saturation current density increases as energy increases in this scenario is because the beam is penetrating. Once the beam is above penetrating energies, an increasing amount of current density is needed to reach the saturation point.

Saturation effects are present, though much reduced, for the thick, ~80 μm thick sample of Experiment C, where $\dot{D}_{sat}$ is $580 \pm 25\%$ Gy/s [FIG. 4.1(b)]. In this case, saturation current densities are

~2000, ~650, and ~400 nA/cm^2 for incident beam energies of 5, 15, and 25 keV, respectively, using Eq. 2.2. Here, the trend in the required current density to reach saturation is opposite that of Sample A. Because the beam is nonpenetrating, all the beam power is deposited in the sample so higher energy results in lower saturation current densities. These saturation behaviors exhibit the idea that the power density, with an energy-dependent correction for penetrating or nonpenetrating behavior (the $\frac{1}{R(E_b)}$ and $\frac{1}{L}$ terms, respectively, in Eq. 2.2), is a key factor in CL intensity.

The smaller saturation dose rate for sample C may also be a result of the preparation method for the samples; the vapor-deposited thin sample would be expected to have substantially more defects than the thick sample (Section 3.1.1). When more defects are available for relaxation of excited electrons, a higher dose rate is required to produce saturation in the CL intensity.

In the McKnight studies (McKnight and Palik, 1980), intensity saturation was also observed as a function of beam current. Their samples, 50-1000 Å thick, were exposed to an electron beam with energy of 2000 and 800 eV and beam current from 1 to 60 µA, and exhibited CL. There is not any information about the current density of the beam, however. The observed intensity saturation is presented for the separate peaks in the spectra as opposed to the total luminescence, as was done in the tests presented in this text. The band McKnight and Palik observed at 450 nm (B) saturated as the current increased. However, the 290 nm (UV) band continued to increase linearly with increasing current, showing no indication of saturation (FIG. 4.2). To fit their data, McKnight used

$$\text{In} = \text{In}(\infty)(1 - e^{-aI_b}) \, ,$$

where In(∞) was determined from the experimental data and a is a constant. Fitting (Fitting *et al.*, 2000) also observed individual band saturation behavior with dose rate.

4.1.2.   Incident Beam Energy

Below saturation current densities, I_γ is linearly proportional to $\dot{D}$. For nonpenetrating radiation, the unsaturated intensity, I_γ, and $\dot{D}$ are linearly proportional to the incident power density, $(J_{inc}E_b/q_e)$, and to E_b. This behavior is depicted by the green curves in FIG. 4.3. For penetrating radiation, the unsaturated intensity I_γ scales as $[E_b/R(E_b)]$, as shown by the blue curves in FIG. 4.3. The intersection of these two
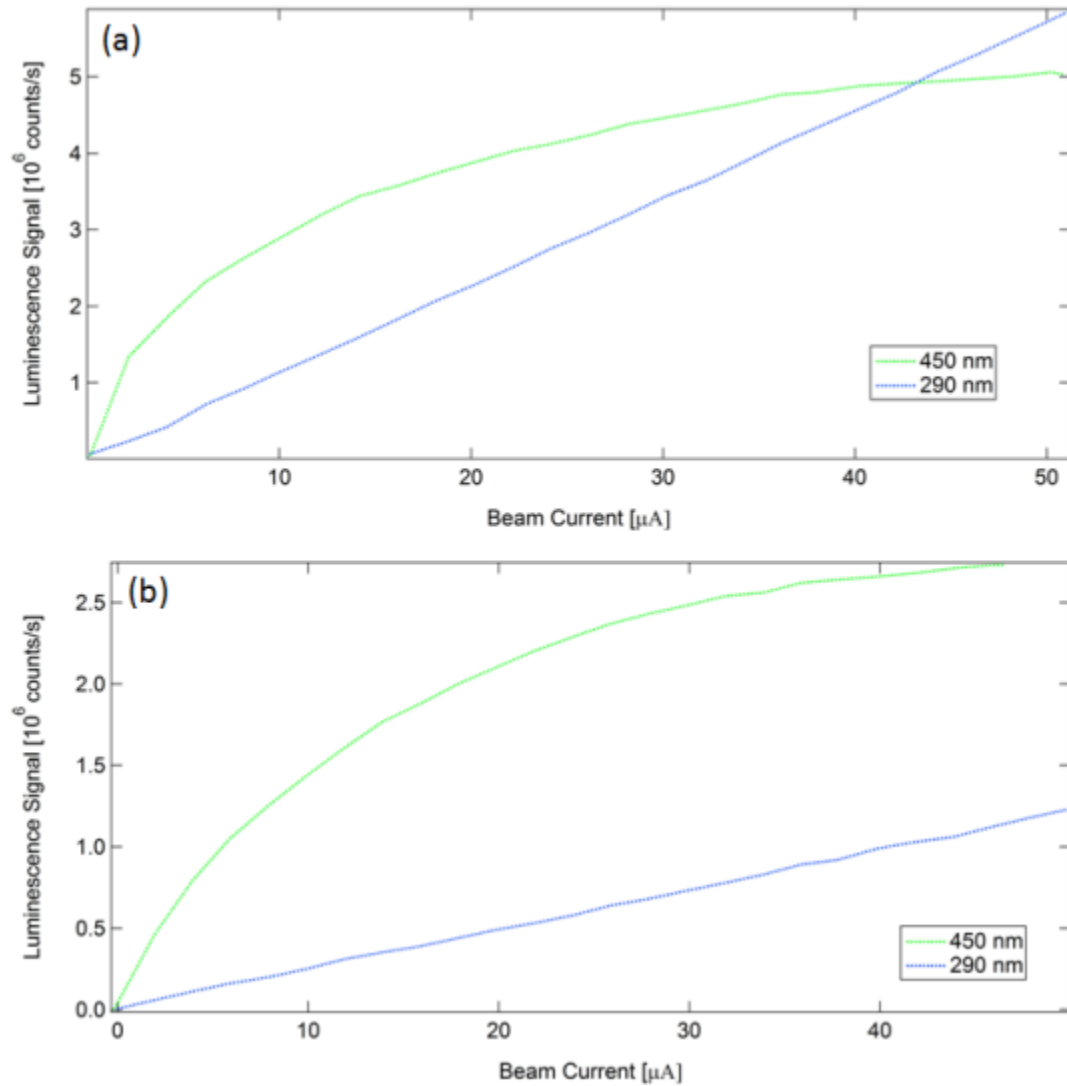
FIG. 4.2. Results from McKnight. (a) Beam voltage of 2000 V and (b) beam voltage of 800 V. The individual band CL intensity of the 450 nm and 290 nm bands as a function of beam current. After McKnight and Palik (1980).

curves occurs at the penetration beam energy at which the range, $R(E_b)$, equals the thickness of the sample,

L. Thus, the expected luminescent behavior follows the solid portions of each curve and the dashed curves

predict the penetrating and nonpenetrating behavior outside their energy ranges of applicability.

The penetration energy, based on the range curve in FIG. 2.6, is denoted by the vertical purple line

(~1.3 keV for Sample A and ~118 keV for Sample C). The behavior of Sample A (~60 nm thick) is shown

in FIG. 4.3(a). The minimum incident beam energy for the study of Sample A was 5 keV, thus, the beam was penetrating at all beam energies incident on this sample. For the Sample C (~80 μm) study, shown in FIG. 4.3(b), the maximum beam energy used in the experiments was 30 keV; thus the experiments were all nonpenetrating. Measured data (purple circles) at a constant 10 nA/cm^2 shown in FIG. 4.3 follow the nonpenetrating portion of the predicted curve for the thick sample and the penetrating portion for the thin sample. The fits in FIG. 4.3 were obtained using the $\dot{D}_{sat}$ value calculated from the previous section related to incident beam current density. For more energy-dependent results, see Appendix B.

The order of the amplitudes of the curves in FIG. 4.1 in Section 4.1, decreasing amplitudes with increasing energy for the penetrating curves in FIG. 4.1(a) and increasing amplitudes with increasing energy for the nonpenetrating behavior in FIG. 4.1(b), also reflect the energy-dependent behavior described above.

Mitchell (Mitchell and Denure, 1973) used the energy dependence of CL intensity to determine the location of the luminescence centers by studying the thickness dependence of luminescence via the range. By changing the beam energy, it penetrates to different depths within the material and therefore, if there are different defects at different depths, the peaks in the CL will change in intensity as beam energy changes. The 450 nm center was located within 250 Å of the Si/SiO$_2$ interface. The 290 nm center was distributed evenly throughout the material.

In the studies done by Goldberg (Goldberg *et al.*, 1997), spatial depth analysis was done by changing the incident beam energy of the electron gun using the constant power method, thus, as they describe, changing the excitation range of CL. The constant power method is just as it sounds, the power, $\frac{E_b J_b}{q_e}$, is kept constant. They explain by using this method, the CL intensity will remain constant as E_b changes if one assumes a homogeneous depth distribution of the centers of luminescence. If, however, it does not remain constant, Goldberg says, the behavior "should be interpreted in terms of CL center depth profiles." The plot from Goldberg shown in FIG. 4.4 is the CL intensity of the blue peak as a function of incident electron energy. The sample is a 250 nm thick SiO$_2$ sample on a Si substrate. According to Goldberg, 4 keV is the energy at which the maximum intensity occurs. From Wilson and Dennison (2012), this maximum should occur at 3.3 keV and which, from the plot, is reasonable. As is explained
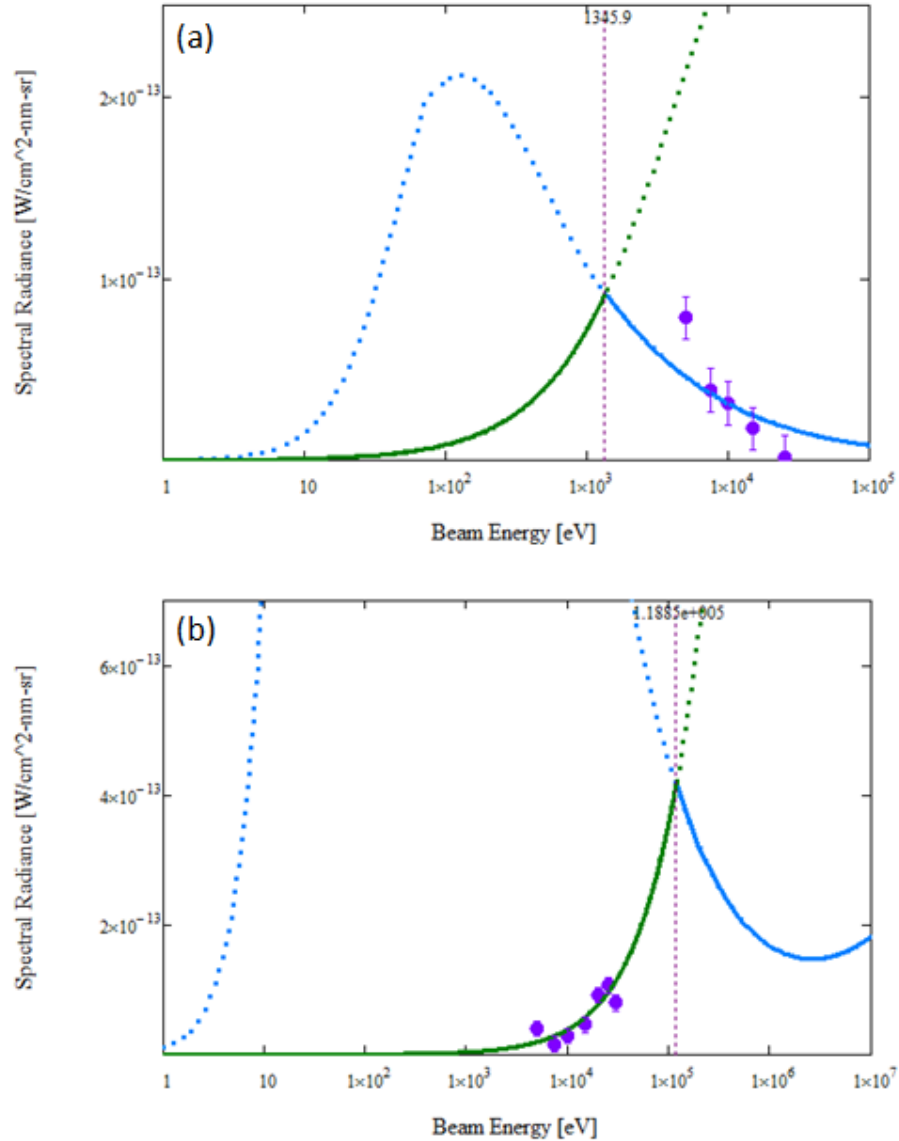
FIG. 4.3. Spectral radiance relationship with beam energy at 10 nA/cm^2. The green curve is the behavior of the spectral radiance when the energy-dependent range is less than the material thickness; all power is deposited into the sample. The blue curve is the behavior of the spectral radiance when the energy-dependent range is greater than the material thickness. The vertical purple dotted line is the energy at which the range is equal to the thickness of the sample, the penetration energy. These curves were created using the range function (FIG. 2.6) and Eqns 2.1 and 2.2. The luminescent behavior follows the solid portions of the curves, not the dotted portions. (a) For Sample A, the penetration energy is ~1.3 keV and the range is greater than the sample thickness, thus, the overall CL intensity decreases with increasing energy. (b) For Sample C, the penetration energy is ~118 keV and the range was less than the sample thickness, thus, the overall CL intensity increases with energy.
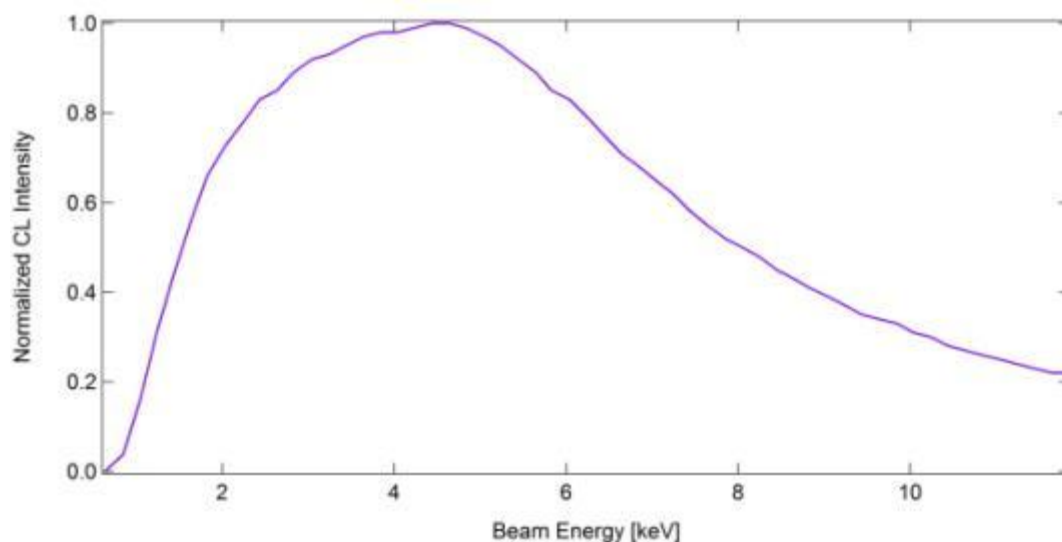
FIG. 4.4. Goldberg's energy-dependent plot. Goldberg identifies 4 keV as the energy at which the maximum intensity occurs, above which the beam is penetrating. The fall off below 4 keV is attributed to a dead layer. After Goldberg *et al.* (1997).

above, Goldberg attributes the falling off in CL intensity at energies above 4 keV to the range of the beam exceeding the thickness of the sample and therefore, some of the power is deposited into the Si substrate. Below 4 keV, the decrease towards zero CL intensity is attributed to what Goldberg terms a dead layer, which is located beneath the surface. By dead layer, he meant a layer of reduced center concentration. Since the blue band is attributed to the ODC in the fused silica structure, the dead layer of this band (and probably the UV band) most likely occurs because there is an excess of oxygen near the surface, which prevents the formation of the ODC CL centers.

4.1.3.   Material Temperature

We begin by looking at the still images from the SLR CCD camera of one of the temperature-dependent runs (FIG. 4.5). By simply looking at these images, it is obvious as the temperature of the sample decreases from 275 K to 55 K, there is a dramatic increase in the CL intensity. A more quantitative study is shown in FIG. 4.6 a plot of the temperature dependence of the SiO_2 spectral radiance for the two samples measured at 5 keV and >200 nA-cm^{-2}, fit with Eq. (2.1). These data come from the processed CCD video camera data. As predicted, the spectral radiance of disordered SiO_2 increases exponentially as the temperature decreases until it reaches a maximum intensity value and horizontal asymptote. The

exponential increase in intensity with decreasing temperature is due to more electrons being retained in the ST states (hence, being available to transition to DT and emit photons) as the thermal energy necessary for ST electrons to be reexcited to the CB is reduced at lower temperature. For Sample B [FIG. 4.6(a)], the value of $\varepsilon_{ST} = 21\pm0.5$ meV. The data for Sample C in FIG. 4.6(b) produce the value of $\varepsilon_{ST} = 5\pm0.5$ meV.

These results are consistent with the following interpretation of the ST DOS, the defect density, and the ε_F^{eff} association with the ST band. Assume the shape of the ST DOS is similar for both samples, as characterized by the distribution width of an exponential monotonically decreasing DOS (Gillespie, 2013). This is reasonable, assuming the ST states result from the same type of defects in both samples. Further,
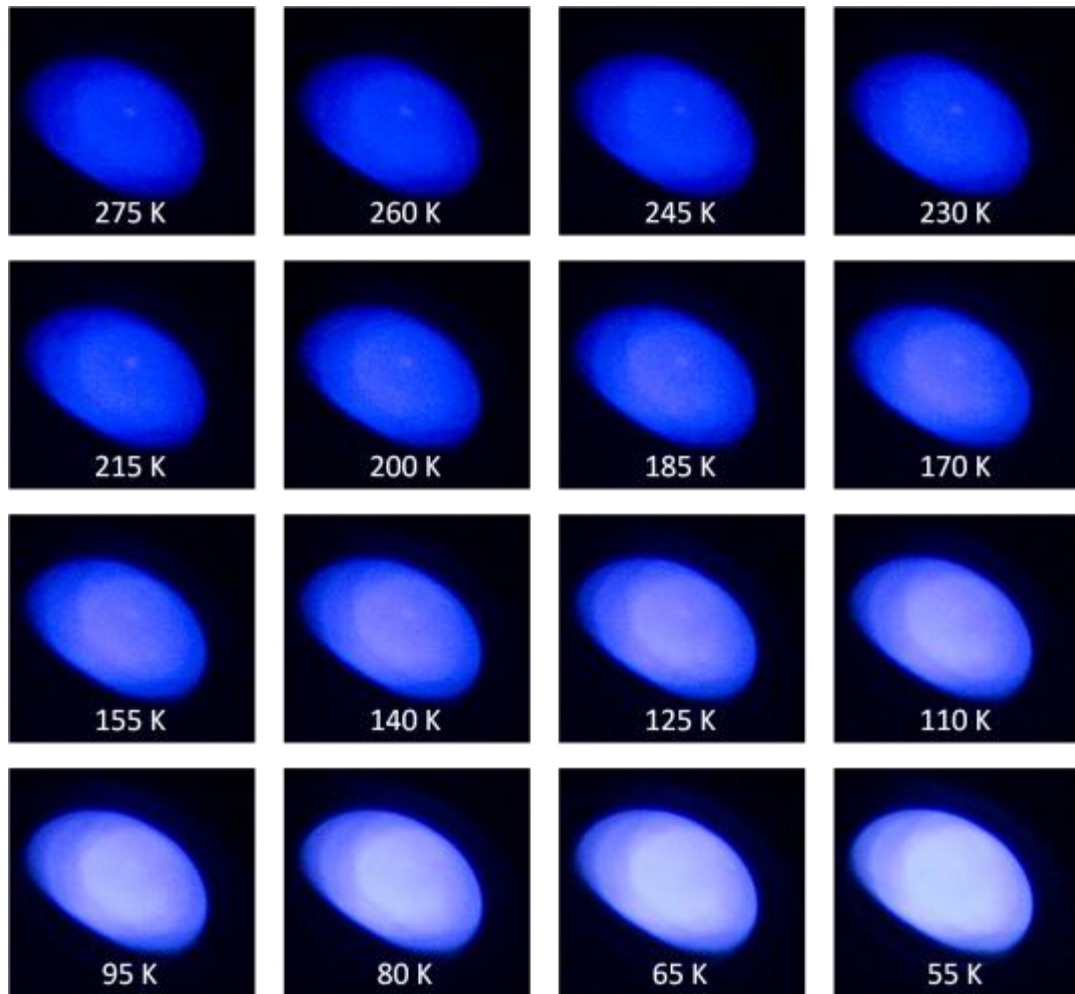
FIG. 4.5. Temperature-dependent SLR images of cathodoluminescence. As the sample temperature decreases from 275 K to 55 K, the overall CL intensity increases dramatically.
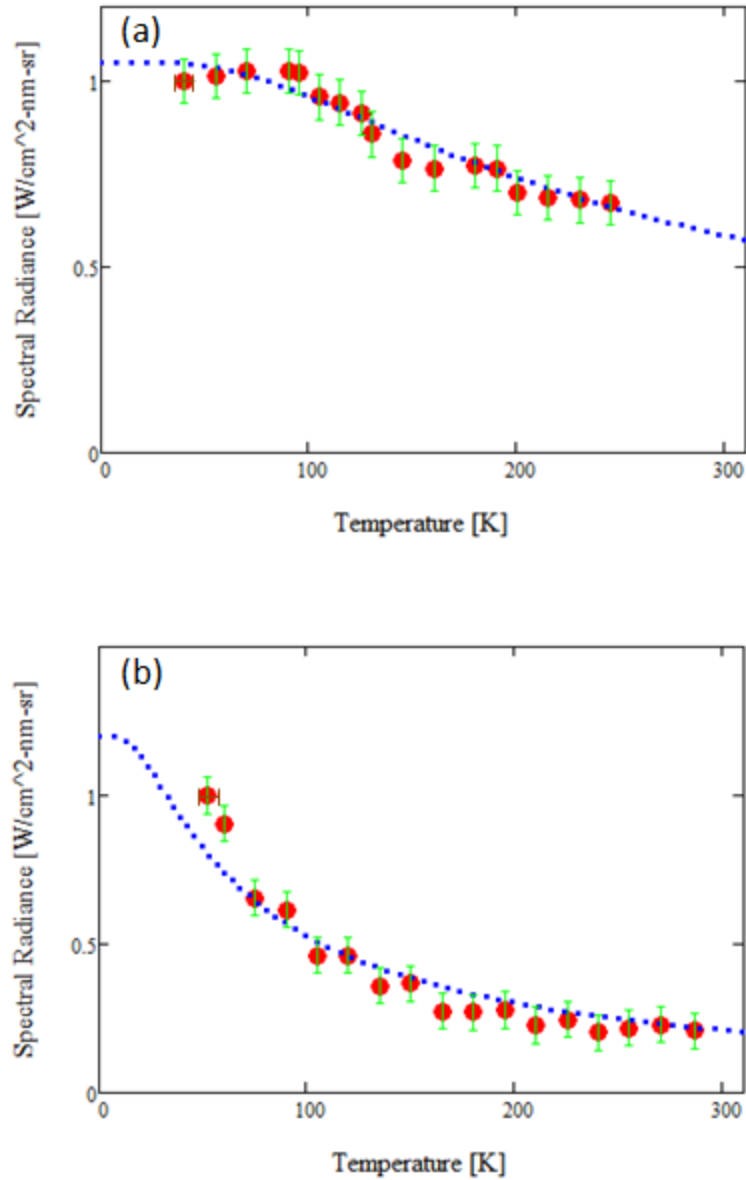
FIG. 4.6. Spectral radiance versus sample temperature. The spectral radiance of SiO_2 as a function of sample temperature, measured at 5 keV and >200 nA-cm^{-2}. Curves are fit with Eq.(2.1). (a) 60 nm sample, fit with a $\varepsilon_{ST} = 21 \pm 0.5$ meV. (b) 80 μm sample, fit with $\varepsilon_{ST} = 5 \pm 0.5$ meV.

assume the ST defect density for Sample C is significantly smaller than for Sample B. This is consistent with the supposition the sputter deposition process used to produce Sample B will create more defects than the hydrolysis process used to produce Sample C. For similar incident dose rates, we would expect the equilibrium number of electrons in the ST states of the two samples to be roughly equal. Hence, the lower

defect DOS for Sample C would be filled to a higher ε_F^{eff} than Sample B. Hence, Sample C would have a smaller ST excitation energy; $\varepsilon_{ST}^C < \varepsilon_{ST}^B$ as observed.

4.1.4.   Four-Band Model

Temperature-dependent emission spectra in the visible range were also collected for thin (Sample B) and thick (Sample C) samples. Note, the spectra are not on an absolute scale, but are only used for relative intensity comparisons. A few representative spectra are shown at selected temperatures for these samples in FIG. 4.7. These plots show the fits to the spectra based on a composite fit with four Gaussian peaks, as described in Appendix A. The set of acquired spectra and their analysis are shown in Appendix C. These two different materials produced spectra, which were similar in the peaks observed, but not entirely the same in terms of relative peak intensity; thus, we can conclude the defect density of states varies from one fused silica sample type to the next. Also, while data were acquired for Sample C from 280 K to 50 K, Sample B had a temperature range of 280 K to 160 K, so the behavior of the two samples cannot be compared below 160 K.

The raw spectral data were fit with composite curves with four Gaussian functions to obtain the spectra shown in FIG. 4.7. The spectra for Sample B [FIG. 4.7(a)] and Sample C [FIG. 4.7(b)] both had two dominant bands centered at approximately 500 nm and 645 nm; an additional shoulder was observed at ~455 nm at low temperature. A fourth peak in the UV range at ~275 nm was observed for the thin samples (Jensen *et al.*, 2014); the UV range below ~350 nm was cut off during experimentation (due to the transmission range of the port window) of Sample C and therefore, was not measured. This is indicated by the dashed line in FIG. 4.7(b). The four peaks in the disordered SiO_2 luminescence spectra are attributed to bands of localized defect or DT states, at ~1.93, ~2.48, ~2.76, and ~4.97 eV below the CB edge (Jensen *et al.*, 2014). As discussed in Section 2.3.3, the positions of these observed peaks are consistent with the results of Salh (Salh *et al.*, 2006) and Trukhin (Trukhin *et al.*, 1998) for similar disordered SiO_2 samples at room temperature. Salh identified the peak at 645 nm as a nonbridging oxygen hole center in the structure. The peak at 500 nm and the 275 nm peak are a result of an oxygen deficient center, as identified by Trukhin. As noted in Section 4.1.2, Mitchell and Goldberg attributed the ~455 nm peak to surface defects.
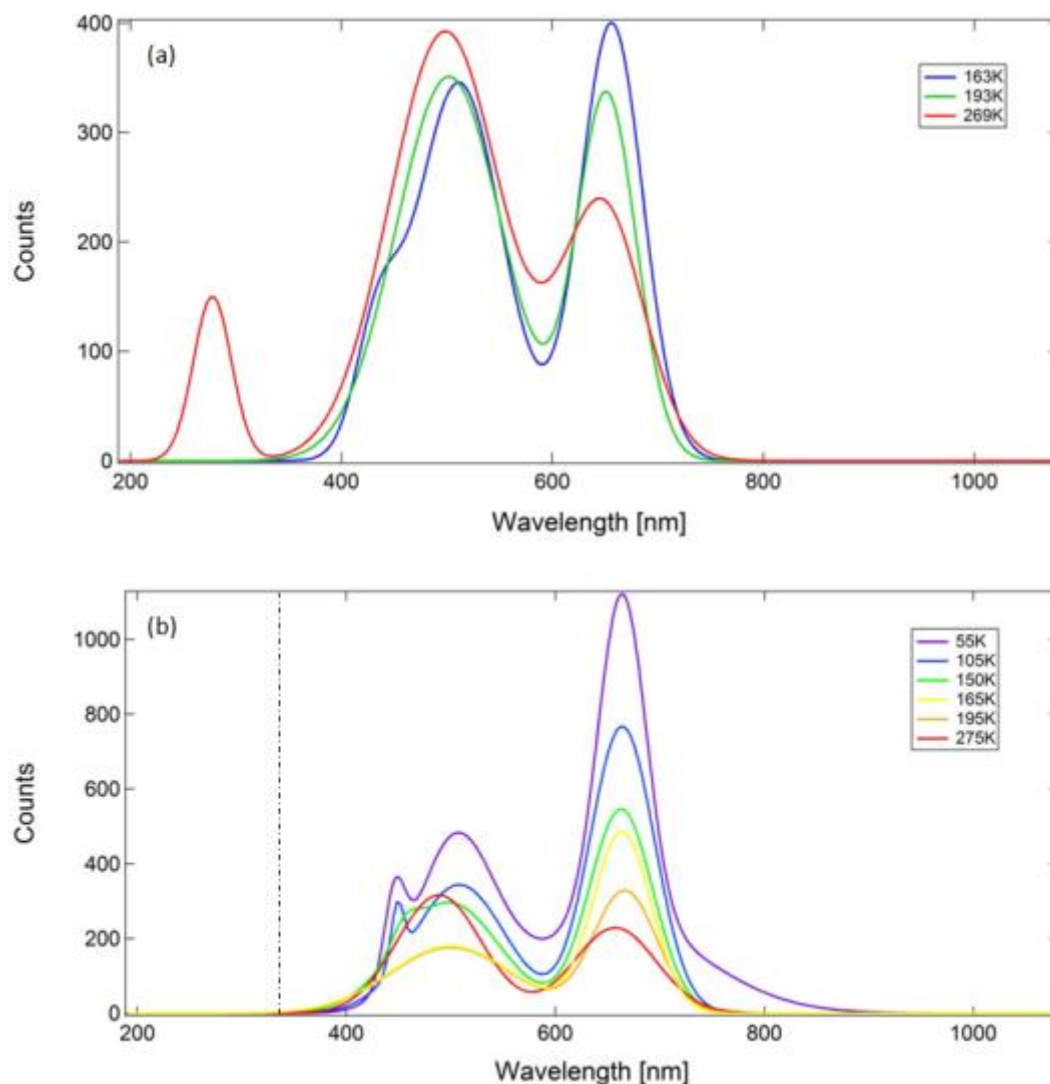
FIG. 4.7. Fits to measured emission spectra obtained at various sample temperatures. The spectra have two peaks centered at ~500 nm and ~645 nm; an additional shoulder is observed at ~455 nm. (a) Spectra are from the Sample B, cooled to ~160 K. (b) Spectra from the Sample C, cooled to ~55 K.

Mitchell attributed the ~275 nm (and by association, the 500 nm) peak to bulk oxygen deficiency sites. The origin of an additional shoulder at ~455 nm has not yet been identified.

As temperature changes, the peak positions remain relatively constant, except where the 455 nm and 500 nm peaks become indistinguishable. This change in position occurs because two peaks coalesce and the combined peak position is located between the individual peak positions. In the R peak, the peak position was consistently located at 663±3 nm. The B peak position was centered at 450±5 nm while the G

peak was centered at 506±7 nm. After the temperature increased beyond 165 K, the combined peak position of the B and G peaks shifted to 495±6 nm.

The peak widths remain relatively constant with changing temperature, but vary from one peak to another. FIG. 4.8 shows a plot of the peak widths for the B, G, and R peaks. Each peak width remains constant within error bars, starting at 55 K down to 165 K, where the blue and green peaks coalesce. Then the B band is no longer distinguishable from the G band and the width of the combined peaks, shown in the plot as a continuation of the G peak width, becomes broader at first and then more narrow. The broadening seems to be an obvious effect of the combination of the two peaks. The narrowing at room temperature, however, does not seem to follow this behavior.

FIG. 4.9 displays the normalized peak intensities for the 500 nm (green) and 645 nm (red) peaks as a function of temperature, for both thin and thick samples. For each sample, the behavior of the red band is very comparable, possibly suggesting the defect density of states for those defects contributing to red photons is similar from one sample to the other. Because the intensity of the red peak continually increases for both samples as the temperature decreases, we can infer the ε_F^{eff} of the material lies below the energy
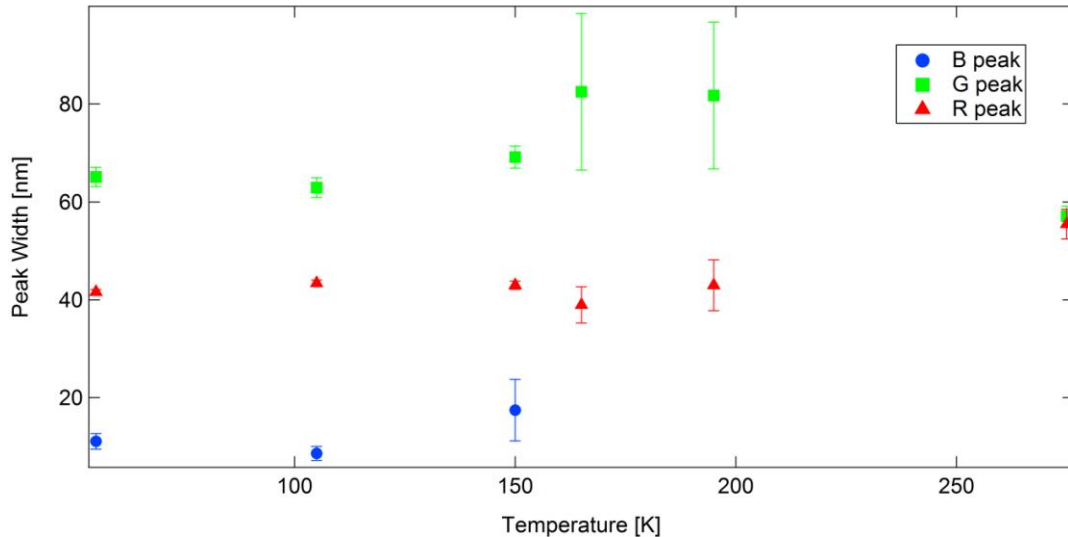

FIG. 4.8. Peak widths for the blue, green, and red spectral peaks. Each remains constant within error bars down to 165 K where the blue and green peaks coalesce. Then the blue band is no longer distinguishable and the width of the peak close to the green peak becomes broader at first and then more narrow.
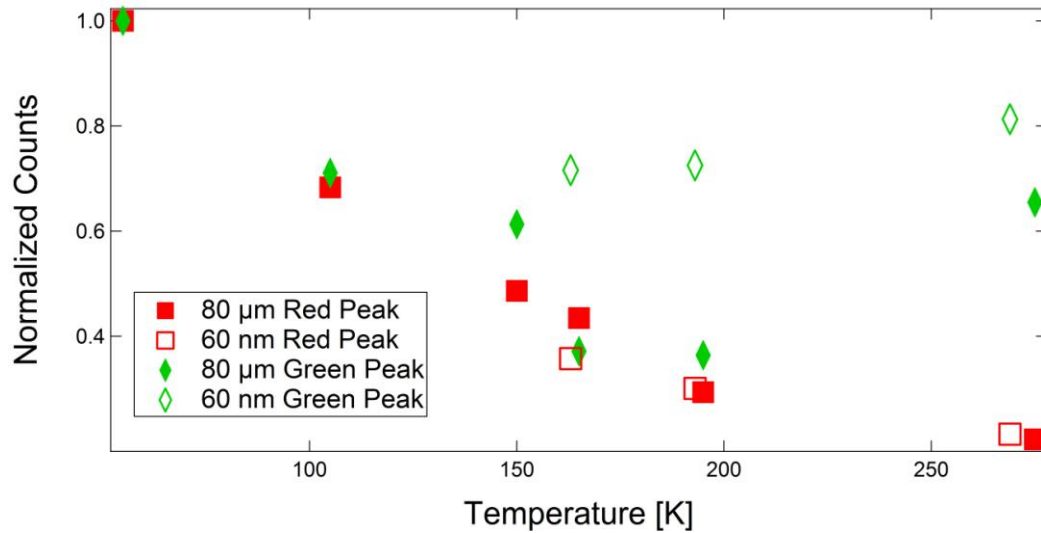
FIG. 4.9. Temperature dependent behavior of the red and green spectral peaks, normalized to the most intense peak value. The red 650 nm peak continually decrease with increasing temperature. The green 500 nm peak also begins decreasing with increasing temperature but starts to increase as temperature approaches 165 K. Separate data are shown for the thin (open symbols) and thick (solid symbols) data.

level of the red peak. This is the same assumption as was made in the two-band model described in Section 2.3.2 and the four-band model of Section 2.3.3.

The UV peak disappears as the sample temperature decreases. This behavior leads to the inference that the energy band is below the ε_F^{eff}. Thus, at absolute zero, the band will be entirely filled and even as the temperature increased, it will have to be well above absolute zero to begin thermally exciting electrons from this band into the higher bands. This is, again, consistent with the same argument as was made in the models of Section 2.3.2 and 2.3.3.

As we consider the green and blue bands, the behavior becomes much more complicated and more difficult to explain. The first difficulty arises in being unable to distinguish the two bands from each other. In some of the spectra, there are two distinct bands, one in the blue (~455 nm) regime and the other in the green (~500 nm). However, in other spectra, distinguishing between the two bands is not possible and it could be assumed the two coalesce. This occurs because the energy level of the two bands, 2.7 eV (B) and 2.48 eV (G), are so close together and the bands, more than likely judging by the width of the combined band, overlap. Due to the work of others (Salh *et al.*, 2006), however, we know there is both a green and a

blue energy level. Others (McKnight and Palik, 1980; Fitting *et al.*, 2000, 2001), however, do not see the appearance of the 2.48 eV band, but see a 2.2 eV band and identify it as green, whereas Salh identifies this as a yellow band. We do not identify a 2.2 eV band in our tests. In the spectra, the intensity of the green or combined peaks decrease with increasing temperature as the temperature approaches 160 K. Above 160 K, however, the behavior of this band becomes scattered. A couple of sets of experiments show a change in band behavior and the intensity begins to increase as the temperature increases. In other sets, as the temperature continues to increase, the intensity will increase in one temperature interval and then decrease in the next interval. This complicated behavior suggests the ε_F^{eff} is located somewhere within both of these bands. This is consistent with the limits placed on the position of the ε_F^{eff} above (that it be between the R and UV bands) and constrains it even more to be located somewhere between 2.48 and 2.7 eV within the band gap.

Similar peak behavior was seen in the still camera images of Sample B, where the red, green and blue components of the color images followed the same temperature-dependent trends as the corresponding peaks in the spectra (Jensen *et al.*, 2014). This was not as clear, however, for the images of Sample C.

These temperature-dependent intensity behaviors are attributed to the thermal filling of the deep traps (Dennison *et al.*, 2012). Recall the CL intensity is proportional to the number of unoccupied DT states into which the ST electrons can decay. (For disordered materials, the peak amplitudes are roughly proportional to the density of states for the associated defect, since there are no symmetry selection rules for disordered states. Further, the spectrometer response function is relatively flat over the spectral range.) The temperature dependence for a given distribution may depend on the position of the ε_F^{eff}, which increases at higher temperatures, as described in (Dennison *et al.*, 2014a). At low temperature the higher-energy defect bands will be largely unoccupied, while those bands below the ε_F^{eff} will be mostly filled. As temperature increases, thermal energy excites electrons in lower bands into higher states, thus enhancing the probability for relaxation of CB and ST electrons into the lower bands and the emission of higher energy photons. This can explain the decrease in the red peak intensity at higher temperatures. The more complicated behavior of the green and blue (which shows up as a small shoulder off the green peak at low

temperatures) peak may result from the ε_F^{eff} moving through the bands associated with these peaks; it may also be complicated due to the close vicinity of the two peaks.

The energy bands have been determined to be approximately Gaussian in shape as a result of the spectral band shapes. Gaussian instrumentation broadening is negligible since the resolution of the spectrometer, 0.5 nm, is much less than the range of width of the bands, ~20-50 nm. The dominance of the Gaussian component of attempted fits with a composite Gaussian, Lorentzian, and Voight distribution indicates minimal lifetime broadening of the DOS signature, as would be expected for the relatively long lifetimes of the DT defect states.

There have been many investigators who have studied the spectra of SiO_2 and have shown the behavior of the spectra depends on the specific type of SiO_2 under radiation.

Fitting (Fitting *et al.*, 2001) compared the spectra of SiO_2 quartz, stishovite, silica glass, and a film layer (500 nm). In these results, the crystalline quartz and stishovite structures exhibit distinct differences in the spectra produced compared to the amorphous structures of silica glass and the film layer. The latter two are similar to the samples used in the experiments presented in this text. The spectra from Fitting show peaks at 650 nm (R), 560 nm (G), 460 nm (B), and 290 nm (UV). The G self-trapped exciton appeared at low temperature in Fitting's work. Here, the R band is attributed to the nonbonding oxygen hole center (Fitting *et al.*, 2001). While the peak, which Fitting identifies as green at 560 nm does not appear in the spectra from the experiments done in this work, it appears in Salh's work, who identifies it as yellow (Salh *et al.*, 2006). Salh was, therefore, able to identify five spectral peaks from the CL.

McKnight performed similar tests on wet and dry oxides of SiO_2 thin films. These were done at 300 K and were obtained after the beam had been on the sample for a few minutes and saturation was reached. Here, they observed peaks at 650 nm (R), 460 nm (B), and 290 nm (UV). The UV peak is attributed to oxygen vacancies, thus explaining the low UV intensity they observed in the wet oxide where there is excess hydrogen present (McKnight and Palik, 1980).

For a summary of the peaks identified by the different investigators, refer to Table 4.1.

Table 4.1. Table of collected data. The spectral peaks are identified by wavelength and color. The peaks seen by different investigators are identified by either an x, which simply means it was observed, or by indicating what defect the investigator attributed to the peak.

Spectral Peaks		Data Source						
λ (nm)	Color	Jensen	Salh	Trukhin	Mitchell	McKnight	Fitting	Goldberg
645	Red	x	NBOHC				x	NBOHC	x
560	Yellow		x					x	
500	Green	x		ODC			self trapped exciton	
455	Blue	x			x	x	x	x
275	UV	x		ODC	x	x	x	x

4.2. Additional Results for Further Consideration

Two additional topics that have been explored in this thesis work are briefly outlined here. Full investigation is left for future studies.

4.2.1.   Time Dependence

Irradiation time can also have an effect on the CL intensity. The time dependence could be a result of saturation; that is, the filling of traps as it comes to equilibrium. It could also be a result of a surface potential modifying the landing energy of the electrons, thus affecting the CL intensity. This dependence is seen in some of the results seen in these experiments (FIG. 4.10). CCD video camera absolute spectral radiance data indicates a time-dependent behavior in the CL intensity. When the beam turns on at ~30 s, the intensity very rapidly goes to a maximum value. It subsequently decays to an equilibrium value after ~25 seconds. The decay is roughly exponential with a decay time constant of ~12±2 s.

McKnight addresses the time dependence of the CL signal at both room and liquid nitrogen temperatures (McKnight and Palik, 1980). Again, they looked at the behaviors of the individual peaks observed. They compare the behaviors of the blue and UV time-dependent CL behavior and show one example of the red-band behavior (FIG. 4.11). The time dependence is most likely a result of the surface potential, which the sample builds up as it undergoes irradiation.

4.2.2.   Edge Effect

Part way through one set of tests on Sample C, the sample was found to be cracked. The cause of this crack is unknown, but it did not present a problem for a majority of the tests. Then, after doing tests at an energy of 30 keV, the beam energy was dropped down to 5 keV and, after stabilization, tests were continued. It was here that an odd behavior was observed. The CL glow was not coming from the entire area of the sample exposed to the beam (though the beam did fill the entire area), but instead came only from the regions around the crack and along the edge of the exposed sample (FIG. 4.12). This was first presumed to be a result of a surface voltage built up from the higher-energy tests done previously, which could dissipate only around the crack and the edges. This led to impromptu tests. The energy was gradually increased and, as this was done, the CL glow began to fill in the gaps on the surface of the sample. The energy was increased to 7 keV and then brought back down to 5 keV and the entire surface area of the sample filled with the glow. Because the effect went away, it is unknown whether it really was an effect of a surface potential. Perhaps a sufficient amount of time was allowed to pass during these tests for the higher surface potential to dissipate and allow the entire surface area to glow again. Simultaneous surface voltage and CL measurements could provide some insight into this strange phenomenon.
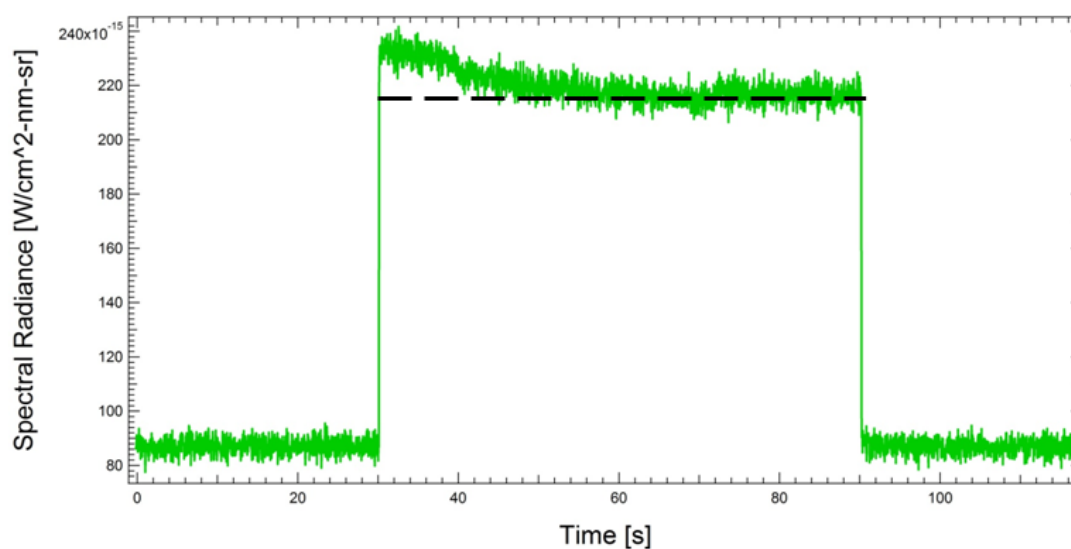

FIG. 4.10. Time dependence of CL intensity. The beam turns on at ~30 s and the intensity goes to a maximum value, then decays to an equilibrium value, represented by the dashed line, after ~25 seconds. This results in a decay time constant of ~12 ± 2 s.

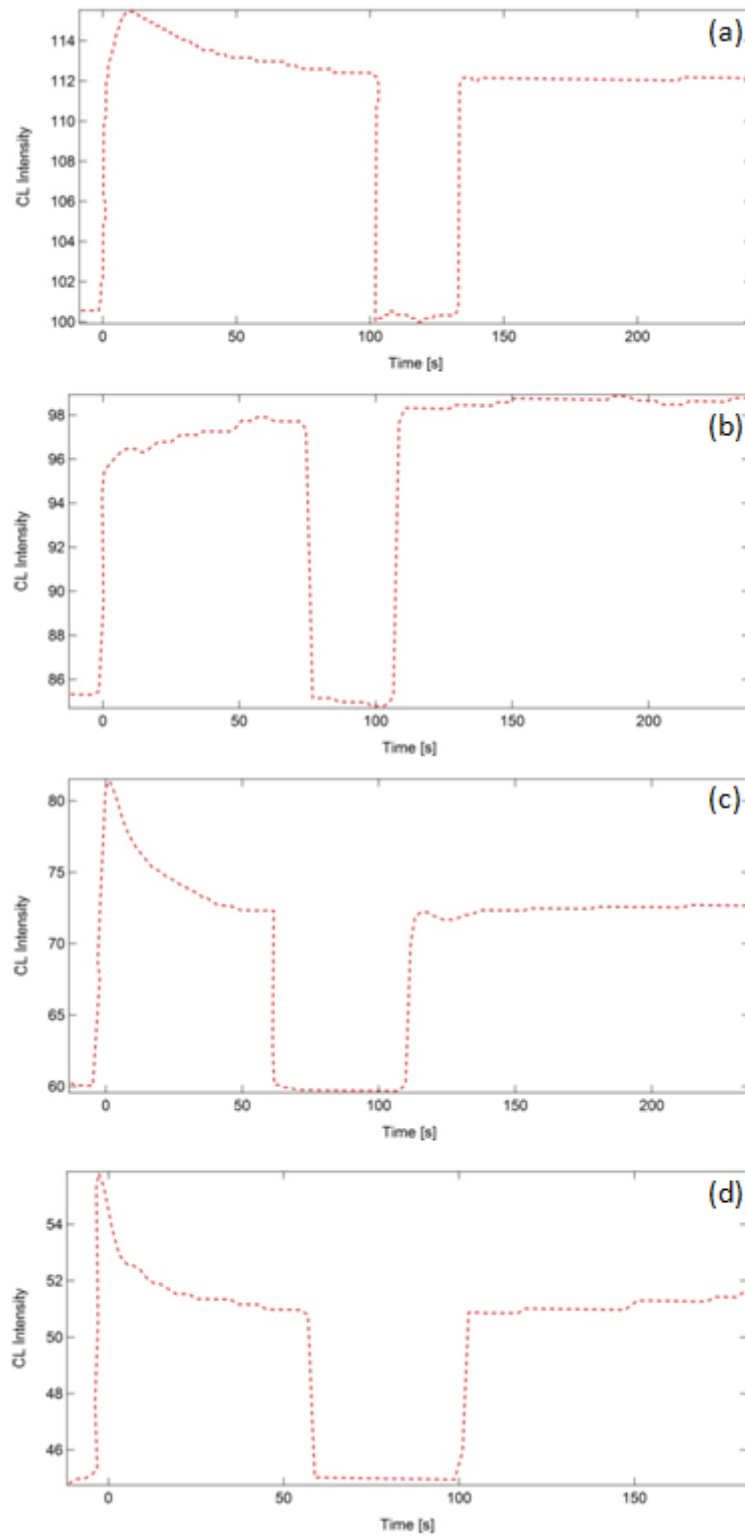FIG. 4.11. Time-dependent results from McKnight. (a) 290 nm peak at 300 K. (b) 450 nm peak at 300 K. (c) 290 nm peak at 95 K. (d) 450 nm peak at 95 K. After McKnight and Palik (1980).
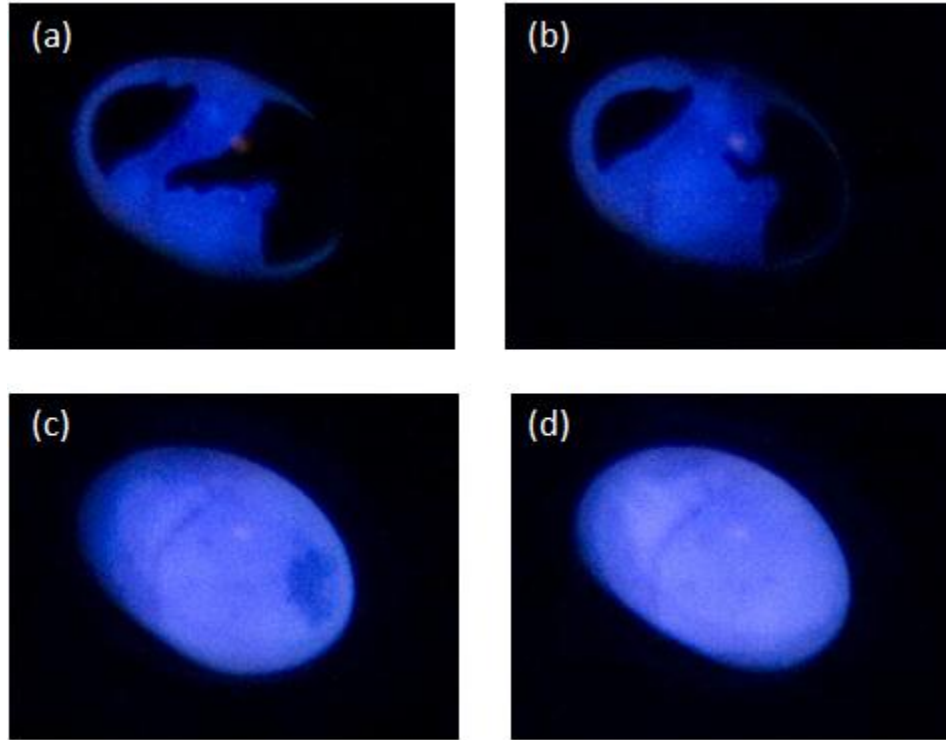
FIG. 4.12. Images of the edge glow effect. The glow appeared around the cracks and the edge of the surface area exposed to the beam in the time sequential frames shown: (a) 5 keV. (b) 5.5 keV. (c) 6 keV. (d) 6.5 keV.

CHAPTER 5

CONCLUSIONS

The conclusion of this work provides a summary of the results, applications, and proposed future work. In the summary is a description of what this work has added to the existing studies. It also recaps the results of these studies and how they fit into the proposed model developed here. The applications section outlines three areas of study for which CL or related behaviors are relevant. Finally, in the future work section are ways in which to improve and extend the work that is presented here.

5.1. Summary of Results

There are many investigators who have studied the presence and behaviors of the spectral bands of fused silica CL. In their studies, the defects associated with the bands have been identified. The temperature-dependent behavior of the individual bands is also studied to some extent. There is little information about the effect of the incident current density and energy on the CL intensity, and the available information is related to individual peaks.

The work presented here also considers the individual spectral bands present in the spectra produced by CL. It looks at the temperature-dependent behavior of these bands from 280 K to 50 K, well below the temperature threshold of previous studies. In the work found in the literature, measurements were made at only two temperatures, room temperature and near liquid nitrogen temperatures; whereas in this work, measurements were taken at equal intervals of temperature as the temperature went from one extreme to the other. Unlike any other work, the dependence of the overall CL intensity on material temperature was also studied.

Furthermore, the effect of incident beam current density and energy on the overall CL intensity was studied extensively. A better understanding of the saturation effect of CL was gained. The dependence of CL intensity on the range of a material has been studied and described extensively. This has not been done prior to this work.

Not only were each of these components measured and studied, but a model was proposed. Equations (2.1) and (2.2) describe the explicit dependence of the CL intensity on incident flux and energy, temperature, and emitted photon wavelength:

$$I_\gamma(J_b, E_b, T, \lambda) \propto \frac{\dot{D}(J_b, E_b)}{\dot{D}(J_b, E_b) + \dot{D}_{sat}} \{[1 - e^{-(\varepsilon_{ST}/k_B T)}]\}\{[1 - \mathbb{A}_f(\lambda)][1 + \mathbb{R}_m(\lambda)]\} \, , \tag{2.1}$$

$$\dot{D}(J_b, E_b) = \frac{E_b \, J_b [1 - \eta(E_b)]}{q_e \rho_m} \times \begin{cases} [1/L] & ; \ R(E_b) < L \\ [1/R(E_b)] & ; \ R(E_b) > L \end{cases} . \tag{2.2}$$

The CL intensity is dependent on the incident beam current density through the dose rate. Through this dependence, fits of data allow determination of the saturation dose rate. The saturation effect was observed as the current density increased at a constant beam energy. At low current density, intensity increased linear as current density increased. Bends observed in the intensity at higher currents suggest the beginning stages of saturation are occurring. Eventually, complete saturation takes place, seen as the intensity data approaches a horizontal asymptote. For a given sample, the saturation current density will vary as the energy is varied. However, for that same given sample, the saturation dose rate will remain constant. From one sample to another, even though it was the same material, the saturation dose rate changed. This can be due, in part, to the method of preparation of the samples, which determines the density of defects within the sample. It can also be due to the thickness of the sample and whether or not the incident beam is penetrating. When the dose rate changes from thickness-dependent to range-dependent behavior, $\dot{D}_{sat}$ increases drastically. This effect is a result of the beam not depositing all of its power into the sample. Thus, at a penetrating energy, a higher current density is needed to reach the saturation point.

As was touched on above, there is an energy at which the beam will penetrate the entire thickness of the sample and only a portion of the beam power is deposited into it. The depth to which this power is deposited is termed the range and it is a material- and energy-dependent property. When the range is less than the sample thickness, the radiation is nonpenetrating; all power is deposited into the material and the

CL intensity increases linearly with increasing energy. Once the penetration energy is reached, a fraction of the power is deposited in the sample and intensity begins to fall off with increasing energy. In the nonpenetrating region of the energy spectrum, the intensity increases with energy because the more energetic beam can excite more VB electrons into the CB. As long as the dose rate is below $\dot{D}_{sat}$, these excited electrons are allowed to relax into ST states and then into DT states and emit photons as they do so.

The temperature of the sample also affected the intensity of disordered SiO_2 CL. As sample temperature decreased from room temperature, the overall CL intensity increased exponentially. This continued until a critical temperature and horizontal asymptote was reached below. The increase in intensity with decreasing temperature suggests as temperature decreases, fewer electrons thermalize from the ST states back into the CB, but rather fall from the ST states into the DT states, emitting photons. This behavior leads to the calculation of ε_{ST}, the mean energy depth of the ST states below the CB; that is, the ε_F^{eff} of the ST DOS. Though this parameter is different for each sample, as is expected because of the difference in defect states for disordered fused silica, ε_{ST} is on the order of 1 to 10 meV for each sample.

Finally, the spectra of disordered SiO_2 were used to determine the energy depth at which localized defect sites are located within the band gap. The wavelengths (and therefore energies) of the spectral bands correspond to the energy difference the electrons fall through from one state to another; that is, from the ST states to a given DT state. The intensities, positions and widths of the four primary peaks observed in the UV/VIS region were measured as a function of temperature from ~50 K to ~280 K.

The bands occurring in the UV and red regions of the electromagnetic spectrum were distinct and had obvious behaviors. Those in the blue and green regions, however, were often indistinct and their behaviors were sometimes inconsistent from one experiment to the next. The bands were determined to be Gaussian in shape, indicating the long lifetimes of the DT defect states. As temperature decreased, the intensity of the red band clearly decreased. This indicates this band is well above the ε_F^{eff} of the material. The UV band is only observed, however, at higher temperatures, indicating it is located below the ε_F^{eff}. It only becomes available for relaxation of excited ST electrons once there is enough thermal energy in the material for UV band electrons to be thermally excited into higher defect trap bands.

In many of the spectra, it becomes very difficult to distinguish between the green and blue CL bands. The location of the green and blue bands corresponds with the work of Salh and Trukhin. However, in the work of McKnight and Fitting, they do not have a corresponding green band, but identify a green band in the location of Trukhin's yellow band. Starting at low temperature, these two bands decrease in intensity as temperature increases, similar to the red band, but around 160 K, this behavior stops and the exact behavior is untraceable. The intensity appears to increase or decrease at random upon changing temperature. This behavior suggests the ε_F^{eff} is located within the two bands, causing the thermal filling and emptying of these bands to be more complicated at higher temperatures where there is a lot of thermal activity.

5.2. Applications

5.2.1. Space

Because spacecraft reside in a harsh space plasma environment, there is a need for studies on and understanding of material charging. Spacecraft charging is the accumulation of an electrical charge on orbiting spacecraft induced by the space plasma environment and has harmful effects on the electrical functionality of spacecraft. It is one of the most destructive occurrences on spacecraft, causing more than half of all spacecraft problems due to the environment (Leach and Alexander, 1995). The space environment includes a dynamic mix of particle species, charged and neutral plasmas, electric and magnetic fields, radiation, and physical debris (Hastings and Garrett, 1996). The effects of spacecraft interaction with this environment can include a range of problems from damage to the craft's structure, degradation of the electronic components, unwanted electrical behavior and, in extreme cases, loss of spacecraft (Leach and Alexander, 1995).

On top of all this, it can also produce unwanted luminescence. Such luminescence can potentially produce a stray light background in space-based astronomical observatories, which are exposed to high-energy electron fluxes from space plasmas. However, the magnitude of CL will also be significantly affected by the environmental conditions, in particular the energy spectrum of impacting electrons. Energy spectra typical of four common space plasma environments (GEO, auroral, plasma sheet, and solar wind), dominated by fluxes (~0.01 pA/cm^2 to ~ 10 nA/cm^2) for electron energies of up to ~100 keV (Hastings and

Garrett, 1996), are shown in FIG. 5.1. Environmental electron fluxes often show a wide variance due to storm conditions, stochastic variability and changes due to the different environments that may be encountered during a particular mission; the curves in FIG. 5.1 are intended to illustrate the range of some of these different environments (Hastings and Garrett, 1996; Minow *et al.*, 2004, 2005). Severe space weather conditions for environments such as those illustrated in FIG. 5.1 have on the order of 10 µW-cm^{-2} incident electron power (*i.e.*, 10 nA-cm^{-2} and 1 keV or 1 nA-cm^{-2} and 10 keV); this provides a scaling factor for comparison of luminescent intensities observed in the experiments described in these studies (Jensen and Dennison, 2013). In the case of IR observatories or sensors, the applications often require low temperatures down to 10's of Kelvin.

The results of these experiments suggest materials used in structural components, optical elements, and thermal control surfaces of spacecraft and space-based observatories could, when exposed to sufficiently energetic, charged particles from the space plasma environment, luminesce (Fitting *et al.*, 2001;
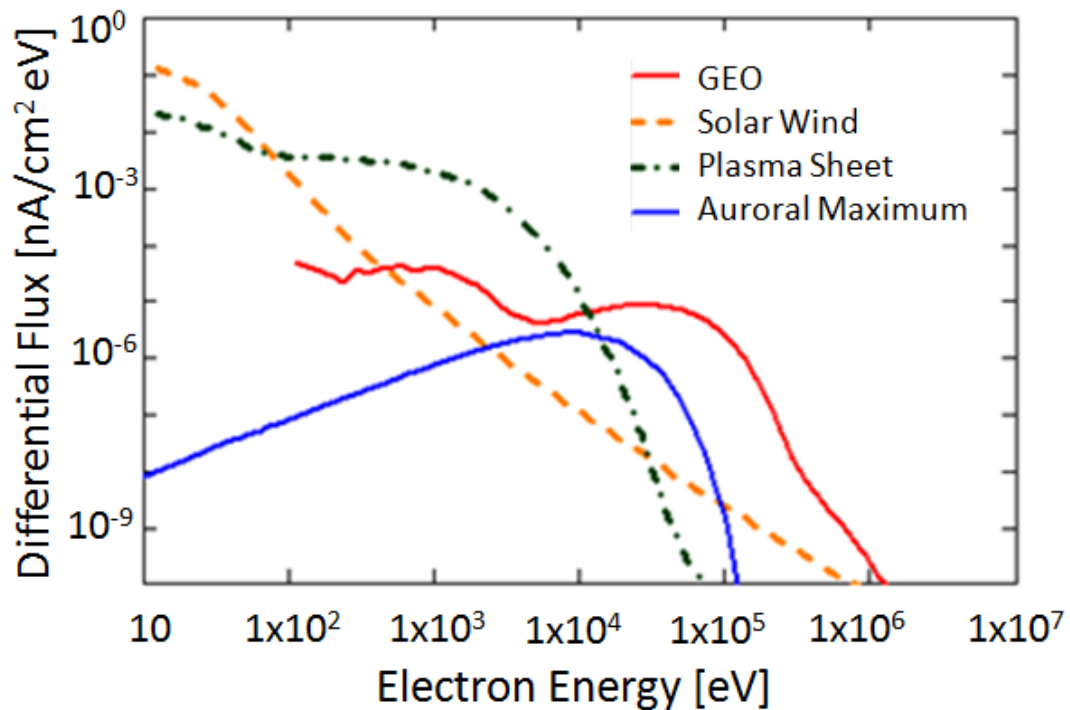

FIG. 5.1. Typical space differential electron flux spectra. Spectra shown for geostationary Earth orbit (Hastings and Garrett, 1996), solar wind at the mean Earth orbital distance (Minow *et al.*, 2005), Earth plasma sheet (Minow *et al.*, 2004) and a peak auroral storm (Hastings and Garrett, 1996).

Griseri *et al.*, 2001; Evans *et al.*, 2011; Dennison *et al.*, 2013; Jensen and Dennison, 2013, 2014; Dekany *et al.*, 2014a). If these visible, infrared and ultraviolet emissions are intense enough, they could potentially produce optical contamination detrimental to the performance of the observatory optical elements and sensors, and act to limit their sensitivity and performance windows (Jensen and Dennison, 2013).

In efforts to explore further into the farthest reaches of our universe, astronomy observation platforms continue to expand in size and complexity and to be located in more exotic and demanding environments. This work will extend the basic research and theoretical aspects of our understanding to allow for a broader application of the concepts to additional mission critical issues. As future observatory missions push the envelope into more extreme environments and more complex and sensitive detection, the fundamental understanding of luminescent dependences on time, temperature, flux, energy, and material structure provided by this work will be useful in building long-lasting spacecraft with high-sensitivity scientific instruments.

There is, however, a potentially useful side of CL on spacecraft. One such useful possibility is to provide the capability for remote monitoring of the evolution of satellite surfaces, using natural space plasma as an excitation source. Materials that have particularly high intensity could be mounted on spacecraft to provide remote monitoring of such things as contamination and spacecraft potential. Ferguson (Ferguson *et al.*, 2013) reviewed these possibilities. They concluded it was unlikely that direct observations of such luminescence from natural space plasma fluxes could be made from Earth-based telescopes or even of GEO satellites from LEO observatories; however, the possibility of observations of these phenomena from co-orbiting LEO or GEO satellites seemed feasible.

5.2.2. Microelectronics

Silicon dioxide has played a large role in the development and evolution of microelectronics. Its high resistivity, dielectric strength, large band gap, and high melting point make SiO_2 an excellent material for use as an interface in microelectronics. It is important to characterize, physically, the films of SiO_2 used in microelectronics. This can be done using multiple methods. These include optical methods, X-ray based methods, ion beam analysis, electron microscopy, and scanning probe microscopy (Green *et al.*, 2001). Along with these techniques, CL has been used to study both optical information, as well as the electronic

structure of the SiO$_2$/Si/metal interfaces found in microelectronics. One useful aspect uses the range of the material and variations of electron beam energy to determine the interface depth in the sample (Brillson, 2012).

5.2.3.   Optically Stimulated Luminescence Dating

In the world of geology, fluvial deposits, the deposits created by rivers and streams, are an important field of research. These deposits archive a water system's response to changes in tectonics, climate, and base level, and are oftentimes associated with archaeological sites. Geologists use these deposits to determine how long ago certain events occurred. However, the usual method of carbon dating can prove difficult due to a lack of organic material in the deposits. Optically stimulated luminescence (OSL) dating uses the luminescent properties of quartz, among a few other materials, to date the sample. The presence of naturally occurring radioactive isotopes in all sediments allows for this technique to be possible. When quartz is exposed to the radiation, quartz electrons can be excited into the trapped states that are located between the conduction and valence bands, just as the electron beam does in the experiments discussed in this paper. When exposed to sunlight, light-stimulated relaxation occurs, which will reset the luminescence signal. Thus, the longer a sample is buried, the longer the radiation exposure time, resulting in a higher luminescence signal when it undergoes OSL dating. The luminescence intensity provides a measurement of the population of the trapped states, the radiation dose, and therefore, the elapsed time since the original sunlight exposure, prior to deposition into the fluvial deposit (Godfrey-Smith *et al.*, 1988; Huntley *et al.*, 1993; Rittenour, 2008).

5.3. Future Work

To continue this work, high-temperature data can be collected. This would verify the model proposed in this work in the high-temperature regime. Here, we would expect the overall CL intensity decline to continue following the trend of the fit shown in the results of Chapter 4; that is, it will approach a constant minimum value of CL intensity. This is due to the thermal excitation of the ST electrons into the CB. The thermal behavior of the individual bands would be interesting to study. There would be even

more thermal excitation from one DT state to another at higher temperatures, which would potentially complicate the band behavior even more.

Also, in future tests, it would be useful to improve and add to the optical data collection instrumentation. One way to do this is to study optical lenses and create a setup of spectrometer collection optics, which is vacuum compatible, thereby, theoretically, enabling the collection of more intense spectra. This would improve the signal-to-noise ratio and could potentially make it possible to get current density-dependent spectra. This could allow the study of the effect of an increasing ε_F^{eff} with increasing incident current density on the overall CL intensity and that of individual bands. Improving the spectra could also help separate the bands that overlap, making them distinguishable from one another. Adding cameras and a second spectrometer that operate in the IR range would indicate whether there is IR CL activity and if so, where the bands are located that contribute to CL.

Other tests that would be useful are nonmonoenergetic beam tests. Here, a low- and high-energy beam would be simultaneously incident on the sample. To accomplish such tests in the facilities currently available, the sample would have to be positioned in such a way the two electron sources discussed in Section 3.3.5 are able to produce beams that will impinge on the sample simultaneously. These tests would be useful in space applications, where there are many charged particles, each with different energies, incident upon the spacecraft. CL from a broadband high-energy radiation source, such as Sr^{90}, which mimics the 250 keV to 2.5 MeV GEO flux spectrum, would also be of interest (Dennison *et al.*, 2014c).

To better understand the CL behavior and the model presented here, tests could be done in such a way as to take surface voltage measurements while also doing CL tests. The effect a surface potential can have on the CL intensity was discussed in Section 2.3.1. Surface voltage measurement capabilities are available at the USU MPG facilities (Hodges *et al.*, 2014) and are discussed in detail in (Wilson *et al.*, 2013).

Finally, the test methods can be extended to other materials where a knowledge of the temperature-dependent behavior of CL will be useful. Such materials include those used in spacecraft construction, for instance Al_2O_3, epoxy resins, carbon composites, and plastic materials (Dekany *et al.*, 2014a).

REFERENCES

Brillson, L. J., 2012, "Applications of Depth-Resolved Cathodoluminescence Spectroscopy," J. Phys. D: Appl. Phys. **45,**1.

Chang, W. Y., J. Dennison, N. Nickles, and R. E. Davies, 2000, "Utah State University Ground-Based Test Facility for Study of Electronic Properties of Spacecraft Materials," in *6th Spacecraft Charging and Technology Conference,* Air Force Research Laboratory Science Center, Hanscom Air Force Base, MA.

Dekany, J., J. Christensen, J. R. Dennison, A. E. Jensen, G. Wilson, T. Schneider, C. W. Bowers, and R. H. Meloy, 2014a, "Variations in Cathodoluminescent Intensity of Spacecraft Materials Exposed to Energetic Electron Bombardment," in *13th Spacecraft Charging Technology Conference,* Pasadena, CA.

Dekany, J., R. H. Johnson, G. Wilson, A. Evans, and J. R. Dennison, 2014b, "Ultrahigh Vacuum Cryosat System for Extended Low Temperature Space Environment Testing," IEEE Trans. on Plasma Sci **42**, 266.

Dennison, J. R., J. Dekany, J. C. Gillespie, P. Lundgreen, A. Anderson, A. E. Jensen, G. Wilson, A. Sim, and R. Hoffman, 2014a, "Synergistic Models of Electron Emission and Transport Measurements of Disordered SiO_2," in *13th Spacecraft Charging Technology Conference,* Pasadena, CA.

Dennison, J. R., J. Dekany, K. Hartley, J. S. Dyer, and R. H. Johnson, 2014b, "Small Satellite Space Environments Effects Test Facility," in *28th Annual AIAA/USU Conference on Small Satellites,* Logan, UT.

Dennison, J. R., A. Evans, G. Wilson, C. W. Bowers, and R. Meloy, 2012, "Electron Beam Induced Luminescence of SiO_2 Optical Coatings," in *Conference on Electrical Insulation and Dielectric Phenomena,* Montreal, Canada.

Dennison, J. R., K. Hartley, L. Phillipps, J. Dekany, R. H. Johnson, and J. S. Dyer, 2014c, "Small Satellite Space Environments Effects Test Facility," in *AIAA/USU Conference on Small Satellites,* Logan, UT.

Dennison, J. R., A. E. Jensen, J. Dekany, G. Wilson, C. W. Bowers, and R. Meloy, 2013, "Diverse Electron-Induced Optical Emissions Form Space Observatory Materials at Low Temperatures," in *Society of Photo-Optical Instrumentation Engineers Cyogenic Optical Systems and Instruments Conference,* San Diego, CA.

Donegan, M., J. Sample, J. R. Dennison, and R. Hoffmann, 2010, "Spacecraft Coating-Induced Charging: A Materials and Modeling Study of Environmental Extremes," J. Spacecraft Rockets **47**, 134.

Evans, A., G. Wilson, J. Dekany, A. Sim, and J. R. Dennison, 2012, "Low Temperature Cathodoluminescence of Space Observatory Materials," in *12th International Spacecraft Charging Technology Conference,* Kitakyushu, Japan.

Evans, A., G. Wilson, and J. Dennison, 2011, "Temperature Dependence of SiO_2 Electron-Induced Luminescence," in *American Physical Society Four Corners Section Meeeting,* University of Arizona, Tucson, AZ.

Ferguson, D. C., J.-M. Drezan, D. A. Barton, J. R. Dennison, and S. Gregory, 2013, "On the Feasibility of Detecting Spacecraft Charging and Arcing by Remote Sensing," in *5th AIAA Atmospheric and Space Environments Conference,* San Diego, CA.

Fitting, H. J., 2009, "How to Make Silica Luminescent?," J. Lumines. **129**, 1488.

Fitting, H. J., T. Barfels, A. N. Trukhin, and B. Schmidt, 2001, "Cathodoluminescence of Crystalline and Amorphous SiO_2 and GeO_2," J. Non-Cryst. Sol. **279**, 51.

Fitting, H. J., T. Barfels, A. Von Czarnowski, and A. N. Trukhin, 2000, "Electron Beam Induced Optical and Electronical Properties of SiO_2," Mat. Sci. Engin.: B **71**, 109.

Gillespie, J. C., 2013, "Measurements of the Temperature Dependence of Radiation Induced Conductivity in Polymeric Dielectrics," Master's thesis (Utah State University).

Gillespie, J. C., J. R. Dennison, and A. Sim, 2014, "Density of State Models and Temperature Dependence of Radiation Induced Conductivity," in *13th Spacecraft Charging Technology Conference,* Pasadena, CA.

Godfrey-Smith, D. I., D. J. Huntley, and W.-H. Chen, 1988, "Optical Dating Studies of Quartz and Feldspar Sediment Extracts," Quaternary Sci. Reviews **7**, 373.

Goldberg, M., H. J. Fitting, and A. N. Trukhin, 1997, "Cathodoluminescence and Cathodoelectroluminescence of Amorphous SiO_2 Films," J. Non-Cryst. Sol. **220**, 69.

Green, M. L., E. P. Gusev, R. Degraeve, and E. L. Garfunkel, 2001, "Ultrathin (<4 Nm) SiO_2 and Si-O-N Gate Dielectric Layers for Silicon Microelectronics: Understanding Theprocessing, Structure, and Physical and Electrical Limits," J. App. Phys. **90**, 2057.

Griseri, V., L. A. Dissado, J. C. Fothergill, C. Laurent, and G. Teyssedre, 2001, "Photoluminescence, Recombination Induced Luminescence and Electroluminescence in Epoxy Resin," J. Phys. D: Appl. Phys. **34,** 2534.

Hastings, D., and H. Garrett, 1996, *Spacecraft-Envrionment Interactions* (Cambridge Press, New York).

Hodges, J., 2012, "*In Situ* Measurements of Electron-Beam-Induced Surface Voltage of Highly Resistive Materials," Master's thesis (Utah State University).

Hodges, J., A. Sim, J. Dekany, G. Wilson, A. Evans, and J. R. Dennison, 2014, "*In Situ* Surface Voltage Measurements of Dielectrics under Electron Beam Irradiation," IEEE Trans. Plasma Sci. **42**, 255.

Hoffmann, R., 2010, "Electron-Induced Electron Yields of Uncharged Insulating Materials," Master's thesis (Utah State University).

Huntley, D. J., J. T. Hutton, and J. R. Prescott, 1993, "Optical Dating Using Inclusions within Quartz Grains," Geology **21**, 1087.

Instruction Manual Electron Gun Model Ek-5-S, 2002, (STAIB Instruments, Munich).

Jensen, A. E., and J. R. Dennison, 2013, "Properties of Cathodoluminescence for Cryogenic Applications of SiO$_2$-Based Space Observatory Optics and Coatings," in *Society of Photo-Optical Instrumentation Engineers Cyogenic Optical Systems and Instruments Conference,* San Diego, CA.

Jensen, A. E., and J. R. Dennison, 2014, "Defects Density of States Model of Cathodoluminescent Intensity and Spectra of Disordered SiO$_2$," in *13th Spacecraft Charging Technology Conference,* Pasadena, CA.

Jensen, A. E., G. Wilson, J. Dekany, A. Sim, and J. R. Dennison, 2014, "Low Temperature Cathodoluminescence of Space Observatory Materials," IEEE Trans. Plasma Sci **42**, 305.

Joblonski, A., 1935, "Uber Den Mechanismmus Des Photoluminescence Vofarbsoff-Phosphoren," Z. Phys. **94**, 33.

Kimball Electron Gun Manual, 2004, (Kimball Electronics, Cleveland).

Lakowicz, A., 1983, *Principles of Flourescnece Spectroscopy*, (Plenum Press, New York).

Leach, R., and M. Alexander, 1995, "Failures and Anomalies Attributed to Spacecraft Charging," NASA STI/Recon Technical Report N **96**, 11547.

McKnight, S. W., and E. D. Palik, 1980, "Cathodoluminescence of SiO$_2$ Films," J. Non-Cryst. Sol. **40**, 595.

Minow, J., W. C. Blackwell Jr., and A. Dickmann, 2004, "Plasma Environment and Models for L2," in *AIAA 42nd Aerospace Sciences Meeting and Exhibit,* Reno, NV.

Minow, J., L. N. Parker, R. L. Alstaff, W. C. Blackwell Jr., and A. Dickmann, 2005, "Radiation and Internal Charging Environments for Thin Dielectrics in Interplanetary Space," in *9th Spacecraft Charging Technology Conference,* Epochal Tsukuba, Tsukuba, Japan.

Mitchell, J. P., and D. G. Denure, 1973, "A Study of Sio Layers on Si Using Cathodoluminescence Spectra," Solid-State Electronics **16**, 825.

Nickles, N., 2002, "The Role of Band Gap in the Secondary Electron Emission of Small Band Gap Semiconductors: Studies of Graphitic Carbon," Ph.D. dissertation (Utah State University).

Rittenour, T. M., 2008, "Luminescence Dating of Fluvial Deposits: Applications to Geomorphic, Palaeoseismic and Archaeological Research," Boreas **37**, 613.

Salh, R., A. V. Czarnowski, M. V. Zamoryanskaya, E. V. Kolesnikova, and H. J. Fitting, 2006, "Cathodoluminescence of Sio$_x$ under-Stoichiometric Silica Layers," Physica Status Solidi (a) **203**, 2049.

Sim, A., and J. Dennison, 2010a, "Unified Model of Charge Transport in Insulating Polymeric Materials," in *15th Rocky Mountain NASA Space Grant Consortium NASA Fellowship Symposium,* Logan, UT.

Sim, A., and J. R. Dennison, 2010b, "Parameterization of Temperautre, Electric Field, Dose Rate and Time Dependence of Low Conductivity Spacecraft Materials Using a Unified Electron Transport Model," in *11th Spacecraft Charging Technology Conference,* Albuquerque, NM.

Thomson, C. D., 2001, "Experimental Investigation of Snapover: The Sudden Increase of Plasma Current Drawn to a Positively Biased Conductor When Surrounded by a Dielectric," Ph.D thesis (Utah State University).

Thomson, C. D., V. Zavyalov, and J. R. Dennison, 2003, "Instrumentation for Studies of Electron Emission and Charging from Insulators," in *Proceedings of the 8th Spacecraft Charging Technology Conference,* NASA Marshall Space Flight Center, Huntsville, AL.

Trukhin, A. N., M. Goldberg, J. Jansons, H. J. Fitting, and I. A. Tale, 1998, "Silicon Dioxide Thin Film Luminescence in Comparison with Bulk Silica," J. Non-Cryst. Sol. **223**, 114.

Wilson, G., 2013, "The Internal Charge Evolution of Multilayered Dielectrics Undergoing Mono-Energetic Electron Bombardment," Master's thesis (Utah State University).

Wilson, G., and J. Dennison, 2010, "Approximation of Range in Materials as a Function of Incident Electron Energy," in *11th Spacecraft Charging and Technology Conference,* Albuquerque, NM.

Wilson, G., and J. R. Dennison, 2012, "Approximation of Range in Materials as a Function of Incident Electron Energy," IEEE Trans. Plasma Sci. **40**, 291.

Wilson, G., JR Dennison, A. E. Jensen, and J. Dekany, 2013, "Electron Energy-Dependent Charging Effects of Multilayered Dielectric Materials," IEEE Trans. Plasma Sci. **41**, 12.

APPENDICES

APPENDIX A

OPTICAL DATA ANALYSIS

CCD Video Camera

Each digital video file consists of hundreds to thousands of individual frames, depending on the length of the video. To convert the video to JPEG images of each frame, the useful form for processing and analysis, each video is run through the ffmpeg program. To run this program, open the command window. The easiest way to do this is to go to the Start menu and search cmd. Once this window is open, you will probably have to change the directory to the one containing your files. If working out of drive F, this is done by typing :F and pressing enter. Next, to get to the correct folder within this drive, type cd [filepath] then press enter. Open the text file, ffmpeg - READ ME final, and paste the file name into the designated places. Then copy that entire line into the command prompt window and press enter. The program will then begin to run, and at the end will have output each frame as its own JPEG file. To begin a new run, change the folder by again typing in cd [filepath] and repeating the process.

Next, open the text file called Input_Data, as well as one of the jpeg images in which you can see where the sample was and the LaB_6 spot in Photoshop^{TM}. It may be necessary to overlay the light image on a run image to see the sample. In the text file, the first two columns define the size of the image. These should not need to be changed. The next four columns define a corner of the image where there should not be any light. Make sure this is the case. The next two, x2 and y2, define the center of the sample. Place the cursor at the center of the sample in Photoshop and record the pixel values. The radius of the sample, r2, cannot include any edge glow. Estimate that value. Next, L, defines half the length of a square that encompasses the sample and all edge glow. This will probably be 10 to 20 more than the radius of the sample, depending on the size of the sample. The center of the LaB_6 spot is defined as x3 and y3 with radius, r3. State what frame is used to obtain this information, what frame the images start on, usually 1, and what the number of the last frame is. Finally, Digits was where the number of digits used in each file name is identified (i.e., fusedsilica_52K_5keV_1nAcm2_xybion_00243 has 5 digits).

Open the MatLAB program named Xybion_RGB_Gray_Pixel_Counter_V.8. Double left clicking to open the program opens MatLAB with the program editor, which can be closed. Right clicking on the

program icon and choosing Run will launch the program immediately into its routine. Once opened, on the left side pane is the directory structure of the current working directory. If not, change this by clicking on the top middle button to the right of the drop down box of Current Folder that has … . From there, navigate to the folder that has the Input data, program, and the folders of images that will run through the program. Right click on the program icon in the left pane and choose run file. All of the dialog and inputs will show in the center pane command window. It will first ask which folder name contains the images to process (it was not case sensitive). Typically, larger Xybion videos are ripped into two folders due to file system limits of windows for number of files per folder. So there may be a folder named something like JPEG 1 and the other JPEG 2. Do one folder at a time. Because there are two folders there will also be two input files and in the end there will be two output files.

After entering the folder name and hitting enter, it will then ask for the file name of the images in that folder. This should be the same for each of the images. Enter only the characters (including underscores, etc.) of the file name before the digit sequence of each image. Then hit enter.

Next, enter the part number, which means if there are two folders of jpeg images you will have two parts corresponding to two inputs and will have two outputs. So to start, enter 1 for part 1.

After hitting enter, a sample image will appear showing the regions it will take the pixel counts from. Make sure these regions lines are correct based on parameters set in the input file. In the command prompt, it will ask if this looks good. If not, enter n, if yes, enter y. Entering n will close the running program within MatLAB and allows necessary adjustments to be made in the input file. Once adjustments have been made, restart the process by right clicking again on the program on the left side and choosing run file. If the image is correct, enter y for yes and the program will begin iterations of processing each image. Once it is complete it will have produced a file named Output 1 for part 1. Output 2 for part 2 is created in the same manner.

Because the cooling runs have ~15 different video files, there will be ~15 output files for the entire run. Before this run can be processed further, these files must be pieced together in order of decreasing temperature. This is done by importing the files, one at a time, into Excel. Keep only the header of the very first file. Then save this as text file.

SLR Still Camera

The raw still camera files cannot be used in analysis. In Adobe Bridge, open one run of photos. Select all the pictures (Ctrl A), right click and select Open in Camera Raw. Again, select all the pictures then click on Save Images at the bottom of the screen. A Save Options dialog box will appear. Under Destination, select Save to New Location. Then click Select Folder and save it in the correct folder for the corresponding run. It is convenient later on to have two separate folders, one for the raw images and another for the JPEG images. Name the files the same as was done when taking the images and make sure the box next to it says 4 digit serial number. Begin numbering at 1, set the file extension to jpeg and quality to maximum then press save. This will convert each picture to a JPEG file. In each SLR folder, there should be a text file called Input_Data. Open that file, as well as one of the jpeg images, in which you can see where the sample is and the LaB_6 spot, in Photoshop. It may be necessary to overlay the light image on a run image to see the sample. In the text file, the first two columns define the size of the image. These should not need to be changed at all. The next four columns define a corner of the image where there should not be any light. Make sure this is the case. The next two, x2 and y2, define the center of the sample. Place the cursor at the center of the sample and record the pixel values. The radius of the sample, r2, cannot include any edge glow. Estimate that value. Next, L, defines half the length of a square that encompasses the sample and all edge glow. This will probably be 10 to 20 more than the radius of the sample. The center of the LaB_6 spot is defined as x3 and y3 with radius r3. Finally, state what frame was used to obtain this information, what frame the images start on, usually 1, and what frame is the last in the file.

Next, open the MatLAB program named Xybion_RGB_Gray_Pixel_Counter_V.8. Double left clicking to open the program opens MatLAB with the program editor, which can be closed. Right clicking on the program icon and choosing Run will launch the program immediately into its routine. Once opened, on the left side pane is the directory structure of the current working directory. If not, change this by clicking on the top middle button to the right of the drop down box of Current Folder that has … . From there, navigate to the folder containing the Input data, program, and the folders of images that will run through the program. Right click on the program icon in the left pane and choose run file. All of the dialog

and inputs will show in the center pane command window. It will first ask which folder name contains the images to process (it was not case sensitive).

After entering the folder name and hitting enter, it will then ask for the file name of the images in that folder. This should be the same for each of the images. Enter only the characters (including underscores, etc.) of the file name before the digit sequence of each image. Then hit enter.

Next, enter the part number, which means if there are two folders of jpeg images you will have two parts corresponding to two inputs and will have two outputs. To start, enter 1 for part 1.

After hitting enter, a sample image will appear showing the regions it will take the pixel counts from. Make sure that these regions lines are correct based on parameters set in the input file. In the command prompt, it will ask if this looks good. If it does, enter y; if not, enter n. Entering n will close the running program within MatLAB and allows necessary adjustments to be made in the input file. Once adjustments have been made, restart the process by right clicking again on the program on the left side and choosing run file. If the image is correct, enter y for yes and the program will begin iterations of processing each image. Once it is complete it will have produced a file named Output.

Image Processing and Intensity Plots

A single IGOR Macro is used to plot the video, still camera, and electrometer data. Each of the text files created above are loaded into the IGOR Macro. The IGOR IESBD Plots Macro will open, organize, set the timescale and plot the data from the several detectors. To begin, open the procedures file, IESBD_plotsv[most current version].ipf. Originally, other data collection instruments were used for similar tests and their output files were processed in the IGOR macro. Because I did not use these instruments, I modified the macro to not include them. This made processing easier and more concise.

To run the macro, compile the program by clicking on the command window at the bottom then run the macro from the drop down menu at the top under Macros. Two windows will then appear, a dialog box to open a file, as well as a dialog box with instructions. If there is the corresponding file, open it, check the detected header information to make sure it is correct, click load, and then click continue on the directions window and the macro will continue to the next step. If the file does not exist, click cancel on the file open dialog window and then click No File on the directions box. After the files are loaded, it will ask

you for the number of beam on times and then, using the electrometer plot, ask you to identify them. Place cursor A at the beginning of the first beam on and cursor B at the end, then click continue. In the case of these experiments, there is usually only one beam on time per run. It will then ask for the light off frames of the video and still camera data. Place cursor A at those positions and click continue. This process is not as important in these runs because we are not trying to match arcing and flaring events from one instrument to another, but it is necessary for the program to run.

Once these times are identified, the IGOR^{TM} routine applies offsets and calibration coefficients to the data. When the macro is complete, plots of the data from each instrument vs. time are created (FIG. A.1). The experiment can then be saved.

Using the plots from this IGOR macro, other plots can be created for more in-depth analysis. For instance, each cryogenic run at a different energy is contained in a separate IGOR file. In order to make sense of the energy dependence of the luminescence, the intensity values of either the still or video camera for each energy must be plotted together against energy. This process is done manually. To obtain the intensity values from the camera data, the dark beam off values must be subtracted from the beam on values. FIG. A.2 shows a typical plot of the video camera output by the IGOR macro. By placing one
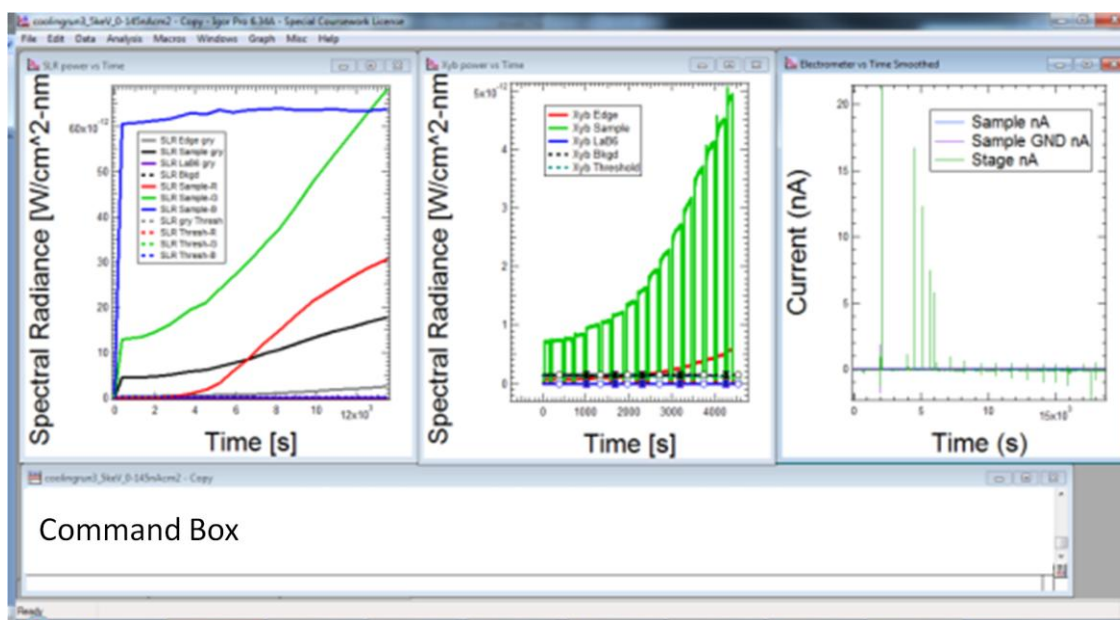
FIG. A.1. Example of the plots that IGOR will produce when the macro has run. The macro procedures will appear in the Command Box.

cursor before the beam on time and one after, two values are obtained, which can be averaged for the dark data. Then the two cursors are placed on the beam on portion of the plot and again, an average is obtained. The dark is then subtracted from the light to give the absolute intensity. When this is completed for each energy, current density and temperature, the proposed model can be applied to the data.

Spectrometer

Read in the .SSM files from the spectrometer into IGOR as General Text files. Once in IGOR, the spectral intensity (defaulted wave 1) is plotted against wavelength (defaulted wave 0). Originally, the spectra were smoothed in order to decrease the noisiness of the spectra. However, upon closer inspection, smoothing caused certain features in the spectra to be either washed out or created. FIG. A.3 shows a raw spectrum overlaid with the same spectrum, but smoothed with different smoothing functions in IGOR, illustrating both the wash out and the creation of features. This is an unwanted side effect of smoothing, and therefore, the spectra were not smoothed for analysis.

Instead, the raw spectra were fitted with Gaussian fits using the Multipeak Fitting package in IGOR Pro version 6 (FIG. A.4). This package has the option to automatically locate peaks, which can be useful, but not always accurate. It can either omit peaks that really are there or find peaks that probably are not truly present. Manually locating peaks is also an available option to add peaks to the fit. With either
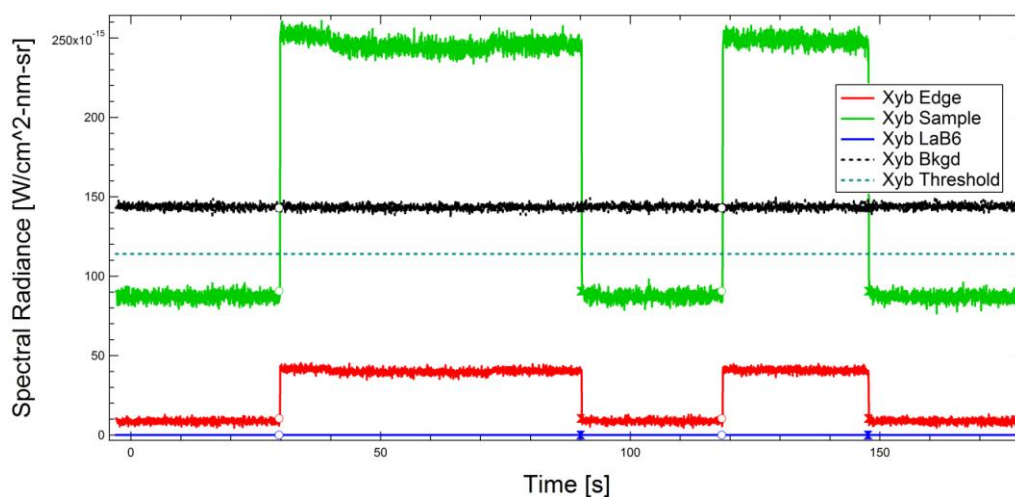
FIG. A.2. Video camera IGOR plot. The green data is used in these tests. The other plots shown are used in other experiments. In this example, the beam off times occur from 0-30 s, 90-120 s, and 145 s-end. Beam on occurs from 30-90 s and 120-145 s.
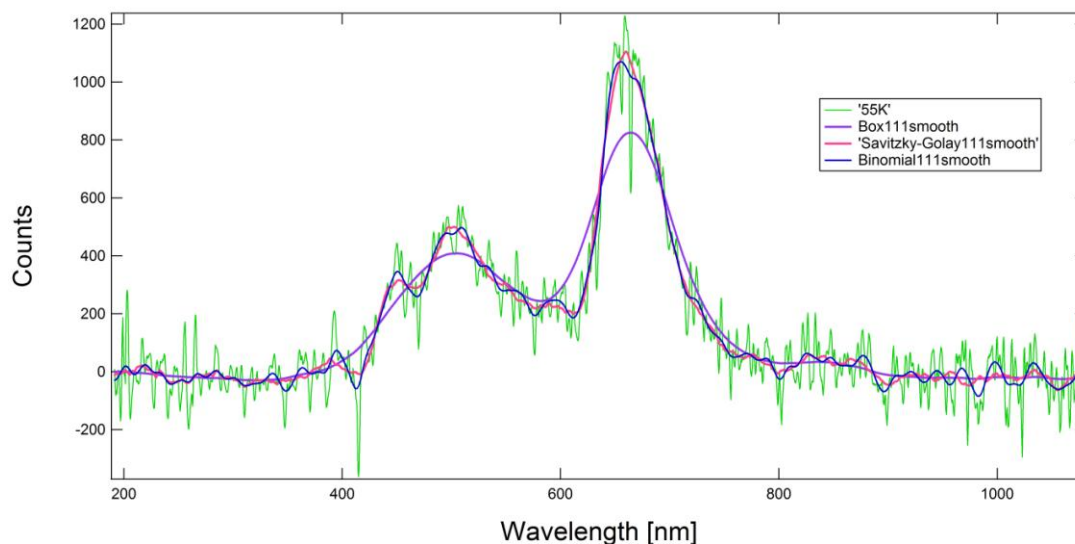
FIG. A.3. Raw versus smoothed spectra. In this figure, we compare the raw data with data smoothed using different functions available in the IGOR program. The Box 111 Smooth function washed out the shoulder at about 460 nm and really dropped the intensity of the 645 nm peak. The Savitzky-Golay and Binomial 111 smooth smoothing functions did pretty good on this spectrum but in others, they washed out features or made them appear.

approach, error can arise. To avoid error, it is imperative to watch for and be aware of trends from spectrum to spectrum. The Gaussian fit is used because it provides the best fit to the spectra. Other fits were attempted, including the Lorentzian and Voigt, but neither of these fit each spectrum as well as the Gaussian, and sometimes would even cause the program to malfunction as it tried to do the fit. Once acceptable fits are complete, the parameters of these fits are used to identify the features of the spectra. These features include the location of a band, its peak amplitude, and the band width. These values are then plotted together for a given band as temperature changes.
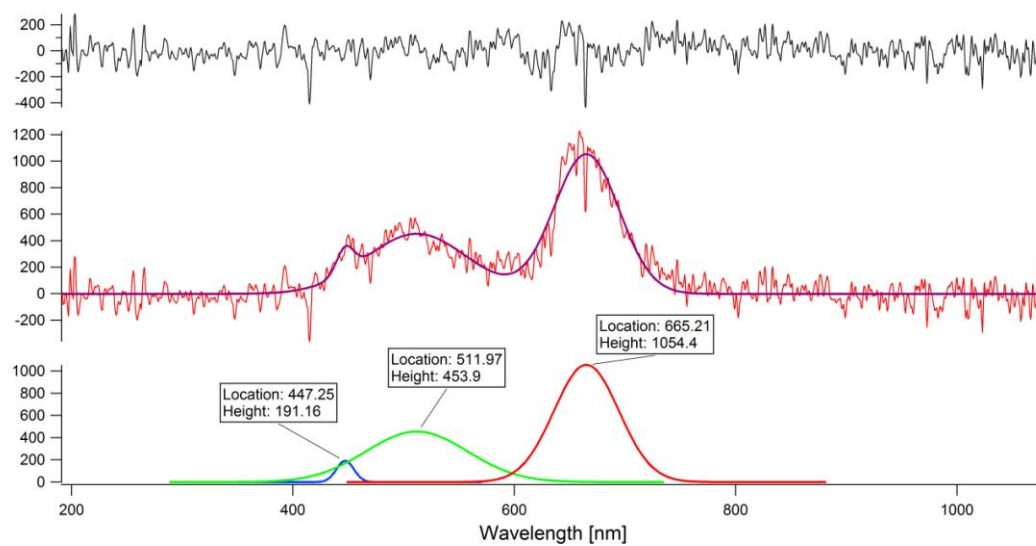
FIG. A.4. Gaussian fits to the spectral peaks. The top black graph is the residual, the middle graph is the sum of the Gaussian's overlaid on the raw spectrum, and the bottom plot shows the individual Gaussian curves.

APPENDIX B

ENERGY RESULTS

This appendix shows energy-dependent data fit with the part of the model that corresponds with its behavior. Figure B.1 is range-dependent data from Sample A. It falls off with increasing energy as described in Eqs. (2.1) and (2.2). The beam is a penetrating beam. Figure B.2 is range-independent data from Sample C and increases with increasing energy as is predicted in Eqs. (2.1) and (2.2). The beam is a nonpenetrating beam.
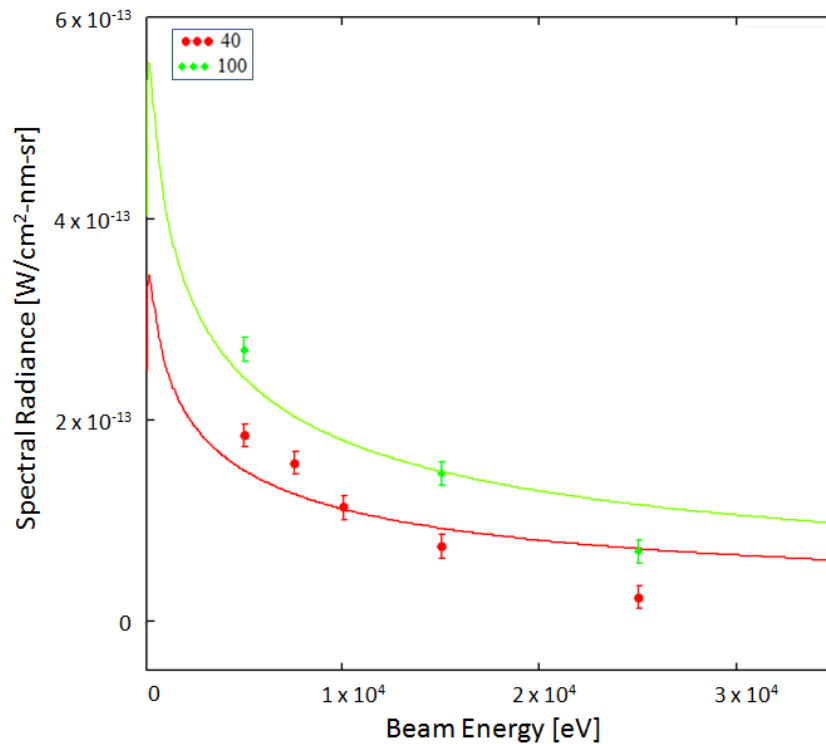
FIG. B.1. Energy dependence of spectral radiance for Sample A. 40 and 100 nA/cm^2 energy-dependent spectral radiance of the 60 nm fused silica sample. It is range dependent and therefore, falls off with increasing energy.
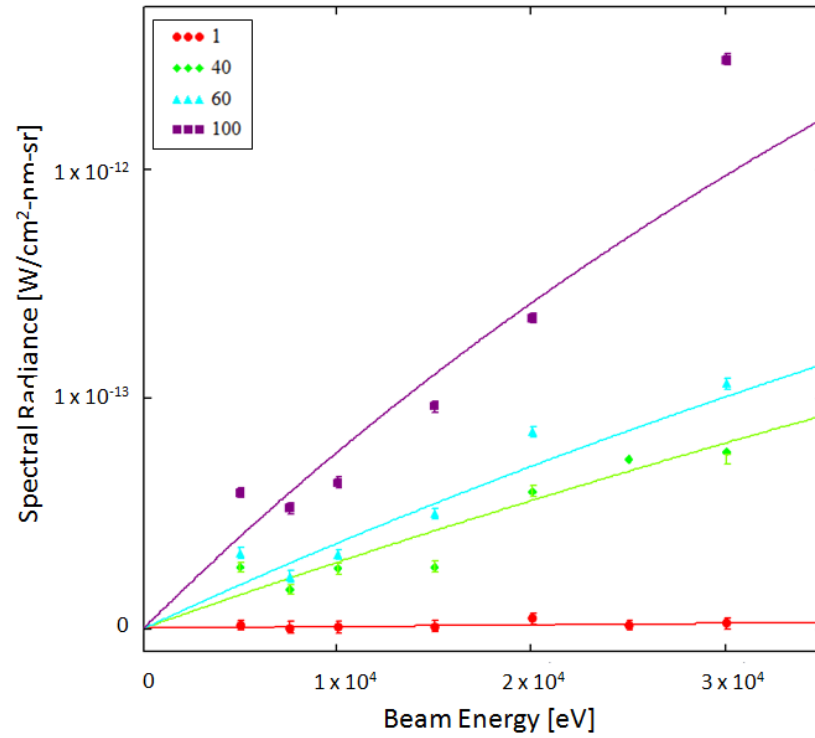
FIG. B.2. Energy dependence of spectral radiance for Sample C. 1, 40, 60, and 100 nA/cm^2 energy-dependent spectral radiance on the 80 μm fused silica sample. It is rang -independent and therefore, increases with increasing energy.

APPENDIX C

SPECTRA ANALYSIS

The figures below show the individual spectrum at a given temperature, the fits for each peak, the residuals, and the total fit. These are the plots used to perform the analysis on the spectral data.
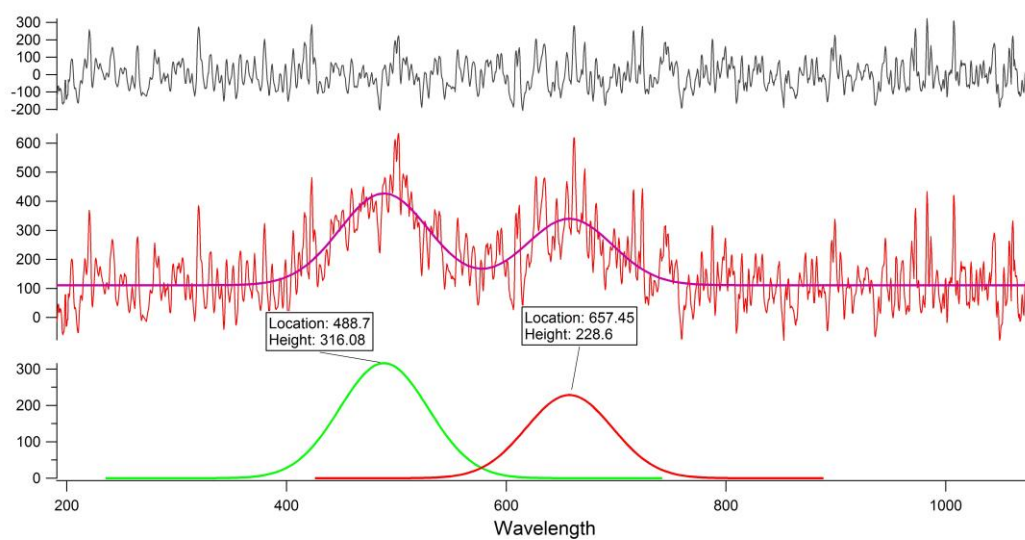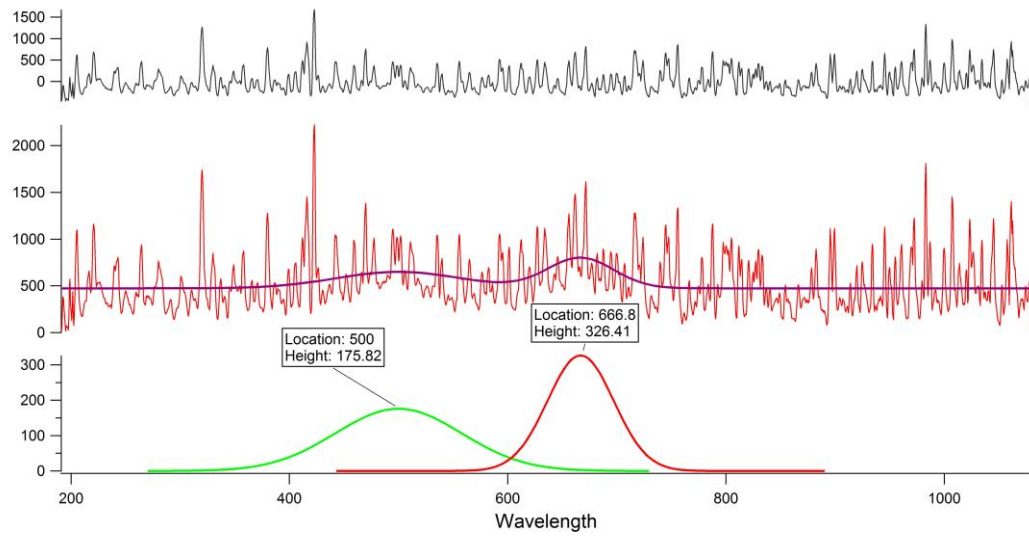

FIG. C.1. 275 K spectrum.

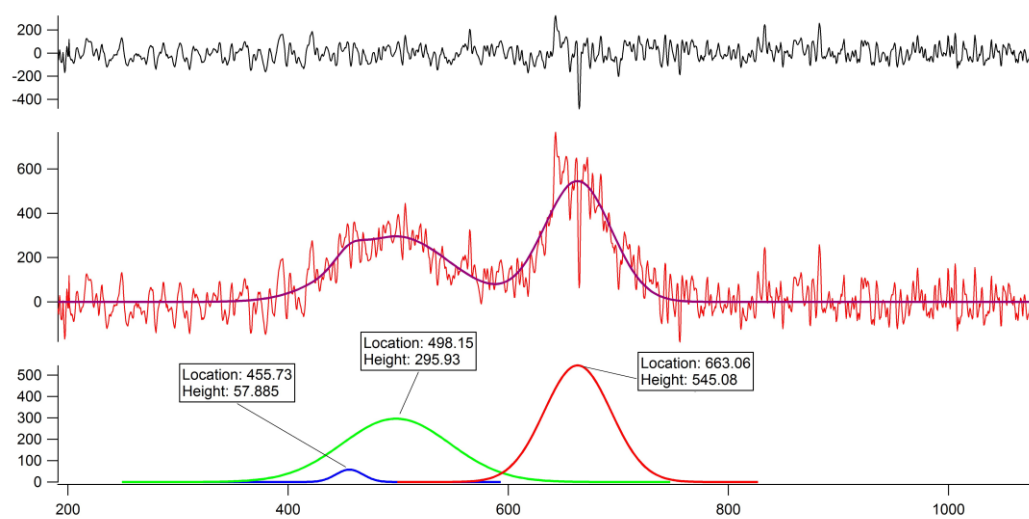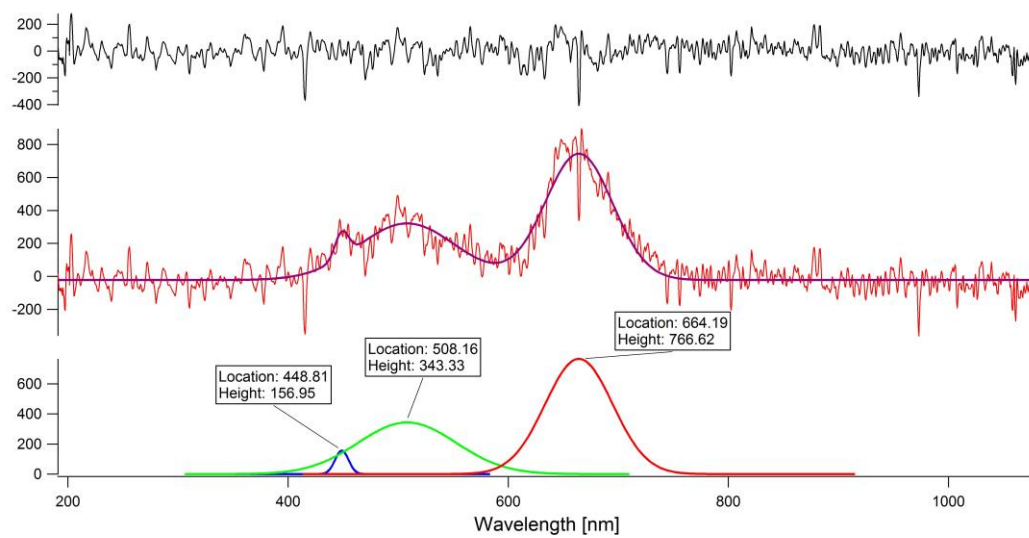FIG. C.2. 195 K spectrum.
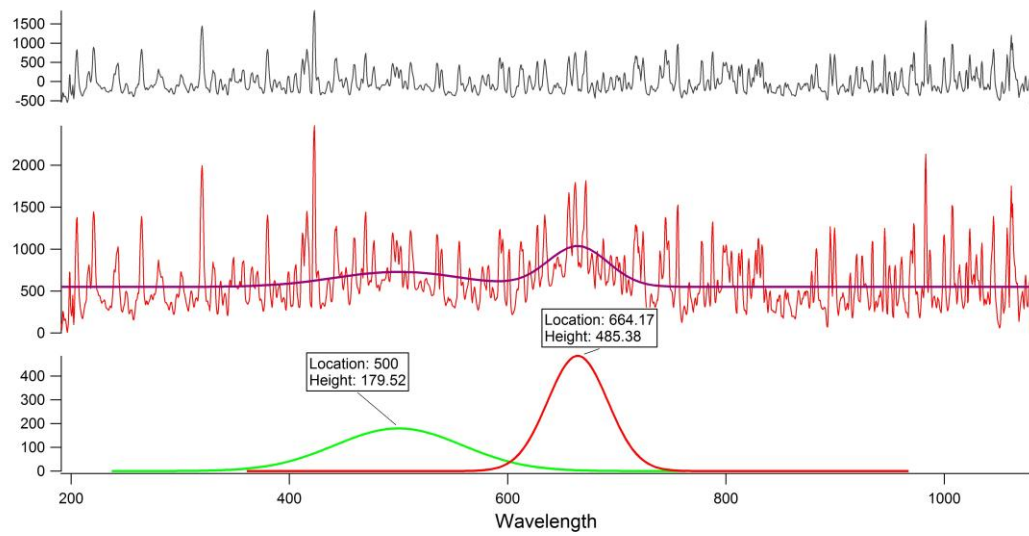
FIG. C.3. 165 K spectrum.

FIG. C.2. 150 K spectrum.

FIG. C.3. 105 K spectrum.

FIG. C.4. 55 K spectrum.